2018

Widefield functional and metabolic imaging from 600 – 1300 nm in the spatial frequency domain

BOSTON UNIVERSITY

COLLEGE OF ENGINEERING

Dissertation

WIDEFIELD FUNCTIONAL AND METABOLIC IMAGING FROM 600 – 1300 NM IN THE SPATIAL FREQUENCY DOMAIN

by

YANYU ZHAO

B.S., Beihang University, 2012
M.S., Boston University, 2016

Submitted in partial fulfillment of the

requirements for the degree of

Doctor of Philosophy

2018

Approved by

First Reader

Darren Roblyer, Ph.D.
Assistant Professor of Biomedical Engineering

Second Reader

Mark Pierce, Ph.D.
Associate Professor of Biomedical Engineering
Rutgers, The State University of New Jersey

Third Reader

Tyrone Porter, Ph.D.
Associate Professor of Mechanical Engineering
Associate Professor of Materials Science and Engineering
Associate Professor of Biomedical Engineering

Fourth Reader

Jerome C. Mertz, Ph.D.
Professor of Biomedical Engineering
Professor of Electrical and Computer Engineering

Fifth Reader

David Boas, Ph.D.
Professor of Biomedical Engineering
Professor of Electrical and Computer Engineering

DEDICATION

To my parents, and Xinyue.

ACKNOWLEDGMENTS

To Darren Roblyer, you've been supportive, responsive, and understanding, and guiding me through lots of difficult yet exciting research projects. It is truly fortunate to have you as my advisor. I am deeply grateful for everything you taught me and all the knowledge you shared.

To Mark Pierce, Tyrone Porter, Jerome Mertz, and David Boas, I think I couldn't have asked for a more helpful and friendly bunch of professors for my committee. Your advice and encouragement made my days much easier!

To John Jiang, thank you for your help on multiple of my animal studies. Your experience and expertise saved my time dramatically and made my work a lot easier.

To everyone I worked with, thank you for your time and help along the way!

Special thanks to all my teachers who inspired me with your knowledge and enthusiasm.

Thank you from the bottom of my heart to my parents who have kept me motivated all the years and given me the freedom to study in a whole new country across the Pacific Ocean. Most of all, thanks to my fiancée who has always been supportive and patient with me. You are the sunshine of my life.

WIDEFIELD FUNCTIONAL AND METABOLIC IMAGING FROM 600 – 1300 NM IN THE SPATIAL FREQUENCY DOMAIN

YANYU ZHAO

Boston University College of Engineering, 2018

Major Professor: Darren Roblyer, Ph.D., Assistant Professor of Biomedical Engineering

ABSTRACT

New methods to measure and quantify tissue molecular composition and metabolism are a major driver of discovery in basic and clinical research. Optical methods are well suited for this task based on the non-invasive nature of many imaging and spectroscopy techniques, the variety of exogenous fluorescent probes available, and the ability to utilize label-free endogenous absorption signatures of tissue chromophores including oxy- and deoxy-hemoglobin, water, lipid, collagen, and glucose.

Despite significant advances in biomedical imaging, there remain challenges in probing tissue information in a fast, wide-field, and non-invasive manner. Moreover, quantitative *in vivo* mapping of endogenous biomarkers such as water and lipids remain relatively less explored by the biomedical optics community due to their characteristic extinction spectra, which have distinct spectral features in the shortwave infrared, a wavelength band that has been traditionally more challenging to measure.

The work presented in this dissertation was focused on developing instrumentation and algorithms for non-invasive quantification of tissue optical properties, fluorophore concentrations, and chromophore concentrations in a wide-field imaging format. All of the imaging methods and algorithms developed in this thesis extend the capability of the

emerging technique called Spatial Frequency Domain Imaging (SFDI). First, a new imaging technique based on SFDI is presented that can quantify the quantum yield of exogenous fluorophores in tissue. This technique can potentially provide a new non-invasive means for *in vivo* mapping of local tissue environment such as temperature and pH. Next, an angle correction algorithm was developed for SFDI for more accurate estimation of tissue optical properties as well as chromophore concentrations in highly curved tissue, including small animal tumor models. Next, a wide-field label-free optical imaging system was developed to simultaneously measure water and lipids using the shortwave infrared (SWIR) wavelength region. Last, to break the bottleneck of processing speed in optical property inversion, new deep learning based models were developed to provide over 300× processing speed improvement.

Together, these projects substantially extend the available contrasts and throughput of SFDI, providing opportunities for new preclinical and clinical applications.

TABLE OF CONTENTS

LIST OF TABLES

LIST OF FIGURES

LIST OF ABBREVIATIONS

AC	Alternating current
BAT	Brown adipose tissue
CPU	Central processing unit
CT	Computed tomography
DC	Direct current
dDOSI	Digital diffuse optical spectroscopic imaging
DNN	Deep neural network
GPU	Graphics processing unit
LED	Light-emitting diode
LUT	Look-up table
MC	Monte Carlo
MRI	Magnetic resonance imaging
NIR	Near-infrared
PBS	Phosphate buffered saline
PET	Positron emission tomography
Ph.D.	Doctor of Philosophy
QY	Quantum yield
QYI	Quantum yield imaging
Rd	Diffuse reflectance
SBR	Signal-background ratio

SFDI	Spatial frequency domain imaging
SVM	Support vector machine
SWIR	Shortwave infrared
WAT	White adipose tissue

CHAPTER ONE: INTRODUCTION

1.1: Motivations

Spatial Frequency Domain Imaging (SFDI) is an emerging wide-field imaging technique that allows for the extraction of tissue optical properties (i.e., absorption and reduced scattering) at visible and near-infrared (NIR) wavelengths. It uses projections of simple illumination patterns to determine the optical modulation transfer function (MTF) of biological tissue in the diffusive regime, which can be converted to optical properties using an appropriate inverse model. SFDI can be used to determine chromophore concentrations if optical absorption is determined at multiple wavelengths. It is currently being explored for a number of clinical and preclinical applications. The motivations of this dissertation are extending endogenous contrast, quantifying exogenous contrast, and improving processing throughout with SFDI.

Recently, our group has begun to evaluate the use of SFDI for small animal tumor imaging, with a focus on monitoring treatment response. To date, most work in this area has focused on extraction of tumor oxyhemoglobin and deoxyhemoglobin concentration to monitor and track tumor metabolism and blood supply. Other endogenous chromophores, such as water, lipid, and collagen, are less explored, and may serve as relevant biomarkers of chemotherapy response.[1–6] Water and lipids are indicators of important biophysical processes and several previous clinical studies have shown that these parameters differ significantly in tumors compared to normal tissues. For example, malignant breast tumors have lower mean bulk lipid composition compared to surrounding normal breast tissue. During treatment, chemosensitive breast tumors tend to increase in lipid composition.[3]

Recent work has shown that different lipid compositions can be identified using hyperspectral Stimulated Raman Scattering (SRS), and it may also be feasible to identify different lipid compositions with Diffuse Optical Spectroscopy.[7–9] Past spectroscopy studies involving lipids and water have generally utilized the lipid absorption peak at 930 nm and the strong water peak at 970 nm. While substantially less explored, the lipid absorption peak at 1210 nm is stronger (higher extinction) than the 930 nm peak and may be less obstructed by water absorption in biological tissue.[10,11] In addition, collagen is another important biological component in tumor evolution and chemotherapy treatment. For example, collagen-dense breast tissue increases the risk of breast carcinoma,[12,13] and aligned collagen has been found as a prognostic signature for survival in human breast carcinoma.[6] It has been shown in clinical studies that collagen content is an important indicator for non-invasive assessment of breast cancer risk, and statistically significant discrimination exists in terms of collagen content between breast benign lesions and tumors.[14–17] Furthermore, it has been shown that adding collagen is important for accurate in-vivo determination of endogenous chromophores.[18] Although less explored, collagen may also be highly relevant for monitoring of treatment response in clinical and preclinical settings.

In addition, with the ability to map wide-field tissue optical properties, *in vivo* fluorescence may be corrected to quantify fluorophore quantum yield. When quantum yield changes with temperature or pH, this can be used as an indicator of the local tissue environment.

Last, while SFDI data collection can be relatively fast, the inversion from measured

data to optical properties has become the bottleneck for real-time tissue information extraction. This is also true for some other optical technologies such as digital diffuse optical spectroscopic imaging (dDOSI). Essentially, the current inverse methods are mapping the measured or calibrated data to an optical property. Therefore, with recent thriving deep learning technologies, faster inverse models based on deep neural networks can potentially be developed to speed up inversion for the extraction of tissue information. The proposed dissertation work aims to develop and validate instrumentation and algorithms to fit this need.

1.2 Chapter Summaries

All the work presented in this dissertation focuses on quantification of tissue information using near-infrared (NIR) and shortwave-infrared (SWIR) light, with a combination of instrumentation and algorithms. Chapter 2 provides background and significance on diffuse optical imaging technology, related applications, and chromophore extraction techniques for tissues. Chapter 3 introduces a quantum yield imaging technique for fluorophores, which could potentially allow *in vivo* mapping of tissue local environment, such as temperature and pH. Chapter 4 improves the SFDI technology by providing an advanced angle correction method with convex optimization algorithms. Chapter 5 highlights the novel SWIR wavelength region for simultaneous mapping of tissue water and lipid content, and demonstrates biomedical applications on small animal models as well as on humans. Chapter 6 introduces a superfast inversion method for the extraction of tissue optical properties based on recent deep learning technologies. Finally,

Chapter 7 presents conclusions and future directions.

CHAPTER TWO: BACKGROUND AND SIGNIFICANCE

This chapter presents the background and significance of diffuse optical imaging in the context of biomedical applications such as chemotherapy response monitoring, a major focus of our research group. Details of SFDI technology are introduced as well as methods to quantitatively extract tissue optical properties and chromophores.

2.1: Chemotherapy Response Monitoring

Together with surgery and radiation therapy, chemotherapy is one of the three most common treatments for solid tumors.[19] Chemotherapy refers to the use of drugs for cancer treatment. For many solid tumors, chemotherapy response can be monitored by measuring tumor volume using PET, ultrasound, MRI, or CT.[20] It is valuable to know early if treatment is working, because ineffective therapies cause unwarranted side-effects that may be life threatening, and may lead to worse outcomes (e.g. shorter survival). In addition, continual monitoring also allows for the detection of therapy resistance. Existing methods for monitoring chemotherapy response include biopsy, MRI, PET, and CT. However, they are unable to longitudinally track therapies at frequent time points. For example, biopsy is invasive and there may be sampling errors. MRI, PET and CT are costly, and require ionizing radiation and/or exogenous agents.

A non-invasive method is needed for tracking earlier metabolic, functional, and molecular response to chemotherapy. Diffuse Optical Spectroscopy (DOS) does this by measuring endogenous chromophores.[21] Endogenous chromophores include oxygenated hemoglobin, deoxygenated hemoglobin, water, lipid, and collagen. By knowing their

concentration, useful information can be derived about tissue physiological activities (e.g. tissue oxygenation) as well as treatment efficacy.[22] Currently most work in this area has focused on extraction of tumor oxyhemoglobin and deoxyhemoglobin concentration to monitor and track tumor metabolism and blood supply.[3,22] In contrast, water, lipid, and collagen are less explored as endogenous chromophores, while they may serve as relevant biomarkers of chemotherapy response.[1–6]

Water and lipids are indicators of important biophysical processes and several previous clinical studies have shown that these parameters differ significantly in tumors compared to normal tissues. For example, water content is an important indicator for edema and inflammation, and is elevated in brain tumors.[23] In addition, malignant breast tumors have lower mean bulk lipid composition compared to surrounding normal breast tissue. During treatment, lipid composition generally increases in chemosensitive breast tumors.[3] Recent work has shown that different lipid compositions can be identified using hyperspectral Stimulated Raman Scattering (SRS), and it may be feasible to identify different lipid compositions with diffuse optical techniques as well.[7,21] However, SRS is a microscopic technique with high spatial resolution but small field of view, whereas SFDI samples a larger volume of tissue which is more clinical relevant.

Collagen is an important biological component in tumor evolution. For example, previous studies have shown that collagen-dense breast tissue increases the risk of breast carcinoma, and aligned collagen has been found as a prognostic signature for survival in human breast carcinoma.[6,12,13] It has been shown in clinical studies that collagen content is an important indicator for non-invasive assessment of breast cancer risk, and statistically

significant discrimination exists in terms of collagen content between breast benign lesions and tumors.[14–17] It has been demonstrated that DOS can identify collagen content in biological tissues, but as discussed earlier, DOS can only provide point measurements.[14]

2.2: Small Animal Endogenous Imaging in Oncology

Oxy- and deoxy-hemoglobin, water, lipids, and collagen have all been shown to be important in clinical oncology.[3,6,23,24] In order to improve clinical practice, small animal imaging is needed to better test biological hypotheses regarding treatment response and new drugs. However, current small animal imaging techniques are not capable of extracting and tracking hemoglobin, water, lipids, and collagen simultaneously and most prior small animal tumor monitoring has focused solely on hemoglobin based parameters. [25] The ability to extract more clinically relevant chromophores in the preclinical setting may better help translate new discoveries related to drug scheduling, new therapies, resistance mechanisms, and other important aspects to the clinic using DOS technology. This dissertation focuses on a new diffuse optical imaging method called Spatial Frequency Domain Imaging (SFDI) that is well-suited to small animal imaging. Additionally, the same optical parameters measured with SFDI are directly translatable to the clinic using technologies such as DOS or DOT.

2.3: Spatial Frequency Domain Imaging (SFDI)

The details of SFDI image acquisition and processing have been described in detail elsewhere.[26,27] The imaging geometry, data flow, and look-up table of SFDI are shown in

Fig. 2.3.1. Briefly, SFDI utilizes spatially modulated sinusoidal light patterns of visible or near-infrared light, projected at different spatial frequencies and wavelengths, to separate the relative contributions of absorption and scattering in diffusive media. Raw reflectance images are sequentially measured, demodulated, and calibrated to create diffuse reflectance maps, with pixel values normalized between 0 and 1. Diffuse reflectance (R_d) maps are created for each wavelength and each spatial frequency. The spatial frequency dependence of R_d at each pixel (i.e. the Modulation Transfer Function) then serves as the input to an inverse model, in this case a Monte-Carlo based look-up table method, which provides pixel-by-pixel optical absorption and reduced scattering values.[28]

Key to the extraction of normalized Rd maps is the calibration of the demodulated raw image data (M_{ac}) against a calibration phantom with known optical properties. The calibration phantom is first measured with the SFDI system, and a forward model is used to determine the expected R_d values based on prior optical property knowledge. A second phantom or tissue-of-interest (with unknown optical properties), is then imaged using the same spatial frequencies and wavelengths, and calibrated R_d maps are produced using Eq. (1), which removes the instrument response.

$$R_{d,tis}(f_x) = \frac{M_{ac,tis}(f_x)}{M_{ac,ref}(f_x)} R_{d,ref}(f_x). \quad (1)$$

R_d and M_{ac} refer to diffuse reflectance and demodulated maps, respectively, and subscripts tis and ref refer to the tissue and calibration phantom, respectively.[27]

In some cases, additional corrections are required for measurements of tissue with spatially varying surface height or angle. In order to account for reflectance intensity

perturbations caused by height variation, a height correction method was previously developed.[29] Briefly, a calibration phantom is measured at multiple heights and the demodulated data (M_{ac}) at each height is extracted. Then, a height map of the object or tissue of interest is acquired using optical profilometry. A new $M_{ac,ref}$ map is then calculated by adjusting the M_{ac} values, pixel by pixel, according to the height versus M_{ac} relationship determined from the multi-height calibration measurements. This M_{ac} data is used to replace the calibration $M_{ac,ref}$ term in Eq. (1). The effect of height correction is to create a virtual calibration phantom such that it has the same pixel-wise height as the object.

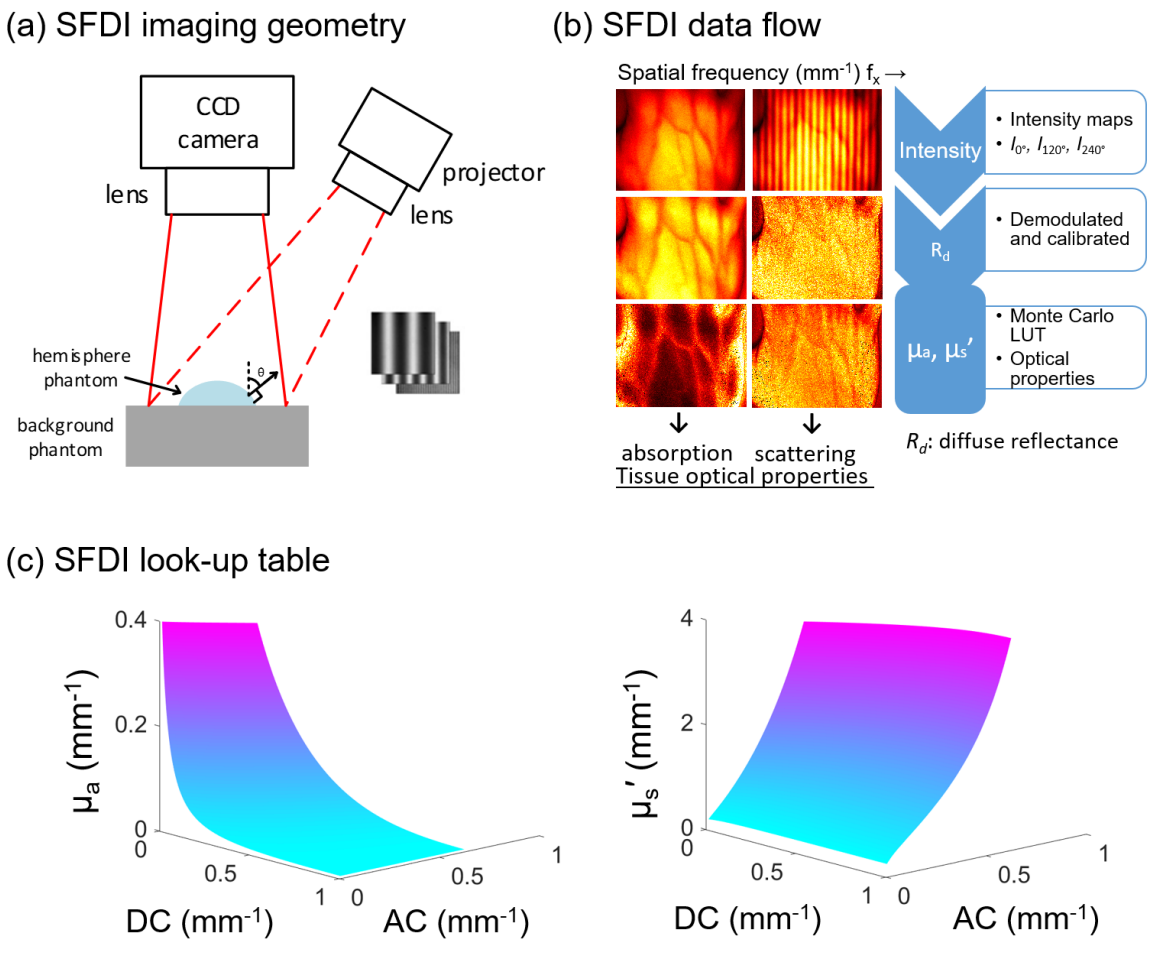

Figure 2.3.1: SFDI imaging geometry, data flow, and look-up-table.

2.4: SFDI Pre-clinical and Clinical Applications

After optical properties at multiple wavelengths are measured, tissue chromophore concentrations can be extracted to help identify disease states, therapy response, and tissue metabolic function. SFDI is being explored for a number of pre-clinical and clinical applications, including skin flap viability, burn wound healing, and subsurface tomography, with the imaging wavelength in the range of 400 nm – 980 nm.[30–43]

Specifically, in Sharif et. al., SFDI has been used to compare oxygen saturation before and after treatment of port-wine stains.[31] In Gioux et al., an SFDI imaging system was applied as a "non-significant risk" device in a clinical trial for measuring hemoglobin concentration.[32] In Rohrbach et. al., a clinic-friendly SFDI system was used to measure oxy- and deoxy-hemoglobin concentrations, as well as total hemoglobin and oxygen saturation for non-melanoma skin cancer.[34]

2.5: Limitations and Improvements of SFDI

While SFDI is increasingly being adopted for both preclinical and clinical studies, we have identified several areas of opportunity for substantially improving this technique in terms of contrasts, accuracy, and throughput. These areas are briefly described here, and then addressed in depth in each chapter of the thesis.

2.5.1: Combining exogenous and endogenous contrasts with SFDI

While SFDI can provide widefield maps of endogenous contrasts such as oxy- and deoxy-hemoglobins, exogenous fluorescence contrast is less explored. The combination of endogenous and exogenous imaging techniques may be able to better quantify tissue fluorescence and extract additional parameters such as fluorophore quantum yield, which

can potentially be used as a microenvironmental biomarker.

2.5.2: SFDI Imaging Artifacts in Small Animal Tumor Models

SFDI is widely used in preclinical imaging such as small animal tumor monitoring. However, due to small feature size and highly curved surface geometry (high angles), SFDI suffers from imaging artifacts near the edge and border of these curved surfaces. Therefore, a correction method is needed for such circumstances.

2.5.3: Imaging Water and Lipids

Current SFDI measurements on endogenous contrast are focused on chromophores such as oxy- and deoxy-hemoglobins and in the wavelength range of near-infrared. Other important biomarkers such as water and lipids, are not available with existing SFDI modalities, due to limited imaging wavelengths.

The absorption spectra of chromophores including water, lipid, oxy- and deoxy-hemoglobin have been described in previous literature, as shown in Fig. 2.5.1.[44,45] Chromophore concentrations can be calculated by fitting optical absorption, which is better done at wavelengths where individual chromophores have high absorbance and not obscured by other chromophores.[46] Past spectroscopy studies involving lipids and water have generally utilized the lipid absorption peak at 930 nm and the strong water peak at 970 nm. While substantially less explored, the lipid absorption peak at 1210 nm is stronger (higher extinction) than the 930 nm peak and may be less obstructed by water absorption in biological tissue.[10,11] Although the lipid 1210 nm peak is still influenced by a nearby water peak (1180 nm) and potentially other spectrally neighboring chromophores, its

absorption is stronger than neighboring chromophores. Studies have also shown notable SWIR absorption features of tissue constituents including water (near 1150, 1450 nm, and 1900 nm), lipids (near 1040, 1200, 1400, and 1700 nm), and collagen (near 1200 and 1500 nm) that are much more prominent than their counterparts in the visible and near-infrared (~400 to 1000 nm).[47,48] Therefore, conducting SFDI in this wavelength range (e.g. for this dissertation, up to 1300 nm) has the potential to provide enhanced sensitivity to chromophores such as water and lipids.

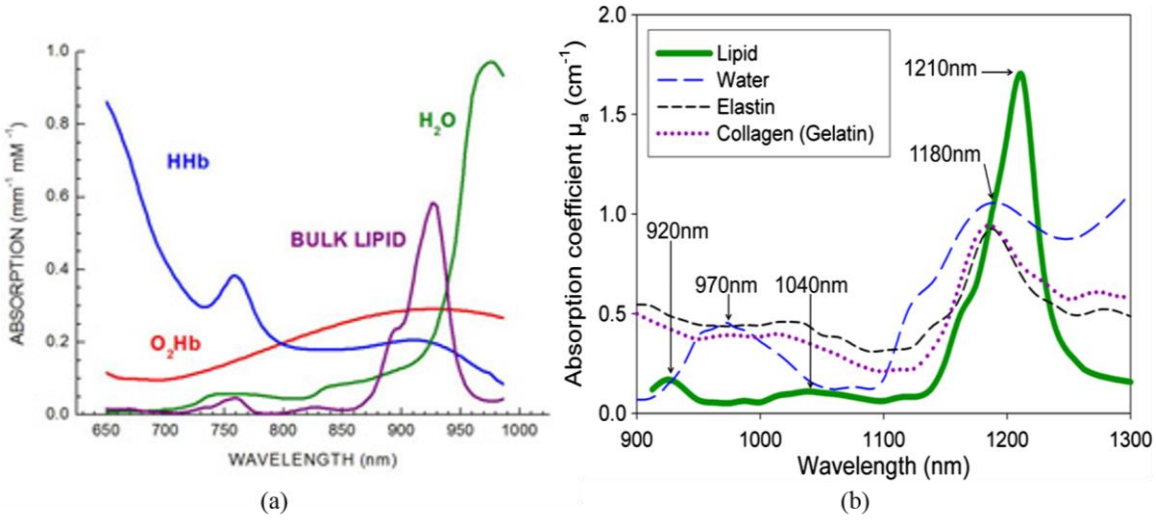

Figure 2.5.1: (a) Absorption spectra of deoxyhemoglobin (Hb), oxyhemoglobin (HbO2), lipid, and water (650 – 990 nm) 44. (b) Absorption coefficient spectra of chromophores including lipid, water, and collagen (900 – 1300 nm) 45. Note that the absorption spectrum of elastin is for demonstration purpose only, and its concentration extraction is beyond the scope of this proposal.

2.5.4: Bottleneck in SFDI processing

While SFDI data collection can be relatively fast, the data processing from measured diffuse reflectance to optical property maps becomes the bottleneck of speed. This is because the inversion from diffuse reflectance to optical properties requires

numerical interpolation at each pixel of the measured maps. In order for real-time feedback of optical properties from SFDI, a higher throughput processing method is needed.

CHAPTER THREE: ENHANCED FLUORESCENCE IMAGING FOR PROBING LOCAL ENVIRONMENT IN DIFFUSIVE MEDIA

Fluorescence imaging with exogenous probes is widely used for preclinical and clinical applications. However, due to effects of tissue absorption and scattering, conventional planar fluorescence imaging is non-quantitative and cannot extract fluorophore quantity or fluorescence efficiency (also known as quantum yield). This chapter presents an enhanced quantitative fluorescence imaging technique that is able to measure key parameters of the local tissue environment in diffusive media. This method utilizes SFDI to quantify tissue optical properties, which are then used to correct planar fluorescence images and extract widefield maps of fluorophore quantum yield. Since quantum yield is sensitive to the microenvironmental state (e.g. pH), this technique can be used to monitor these parameters in a new way.

The work in Chapter Three is published in the Journal of Biomedical Optics [39] with the following contributing authors:

Yanyu Zhao,[1] and Darren Roblyer [1]

[1] *Boston University, Department of Biomedical Engineering, 44 Cummington Mall, Boston, Massachusetts 02215, United States*

3.1: Introduction

Optical imaging with the use of exogenous targeted fluorescent agents (i.e. Molecular Imaging) is increasingly used in the preclinical setting for understanding disease progression and the biological effects of treatments in vivo with high specificity.[49] Probes

that excite and emit in the near-infrared (NIR) (600-1000 nm) allow for deep photon penetration (several mm's) while minimizing tissue autofluorescence. Almost all commercially available fluorescence small animal imaging systems collect planer fluorescence light emission from the tissue surface. One of the major drawbacks of these imaging setups is the inability to extract quantitative fluorescence signals or probe concentrations due to the effects of the surrounding tissue optical properties, namely absorption and scattering. Without additional correction for background optical properties, these systems are unable to provide fluorescence intensity maps that are quantitatively comparable between samples or animals. An additional complicating factor is that the intensity of the collected fluorescence is not only dependent on the fluorophore concentration, but also depends on the quantum yield (QY), which is defined as the ratio of emitted photons to absorbed photons in the respective emission and absorption wavelengths bands.[50] For some fluorophores, the QY is highly sensitive to environmental conditions such as pH, temperature, oxygen concentration, and other factors.[51–55] While a varying QY generally represents a challenge for quantitative fluorescence imaging, it also suggests that QY may be used as a novel microenvironmental biosensor if it can be accurately measured *in vivo*.

In the laboratory setting, fluorescence QY is commonly determined by comparing the fluorescence intensity of a fluorophore with an unknown QY to a standard with known QY, with both samples measured in an optically dilute, non-scattering media.[56–59] QY determination is more difficult in tissue due to the interaction of both the excitation and emission photons with the surrounding medium, where there may be substantial attenuation

due to both absorption and scattering events. However, if the optical properties at both the absorption and emission wavelengths are known, established models allow for a quantitative fluorescence signal to be extracted.[60–62] If one also assumes a known QY, quantitative fluorescence also allows for probe concentrations to be determined. In this work, we posit that if a priori knowledge of the probe concentration is available, the unknown probe QY can be determined.

We present here a quantitative wide-field imaging modality called Quantum Yield Imaging (QYI) that has the ability to spatially map the QY of a fluorophore in diffusive media such as tissue. QYI uses a combination of Spatial Frequency Domain Imaging (SFDI) and planar fluorescence imaging to accomplish this task.[27] SFDI quantifies optical properties of the diffusive media at both the excitation and emission wavelengths, and is used to determine probe concentration using absorption contrast at the excitation wavelength. This information then feeds a modified quantitative fluorescence model that corrects the planar fluorescence raw signal intensity, producing a pixel-by-pixel map of QY values in a wide-field image.[60,61] We demonstrate this method using tissue-mimicking optical phantoms and show that the QY of two fluorophores, rhodamine B, which is highly sensitive to its solvent composition, and SNARF-5, which is pH sensitive, can be quantitated and spatially mapped using QYI under a variety of experimental conditions and background optical properties. QYI may provide a new means to nondestructively determine important tissue microenvironmental parameters *in vivo*, such as local pH, temperature, probe binding, and more.

3.2: Methods

QYI imaging combines SFDI and planar fluorescence with a modified empirical model of quantitative fluorescence. The details of each of these methods are outlined here as well as the overall methodology for combining their information outputs to generate QY maps. Then, the methodology for determining the accuracy of QYI is outlined, namely by extracting the QY of two fluorophores, rhodamine B and SNARF-5, each measured under a variety of experimental conditions.

SFDI is used to extract optical properties from the background media in QYI. SFDI utilizes spatially modulated sinusoidal light patterns of visible or near-infrared light, projected at different spatial frequencies and wavelengths, to separate the relative contributions of absorption and scattering in diffusive media.[27,60] Raw reflectance images are sequentially measured, demodulated, and calibrated to create diffuse reflectance maps. From these maps, optical properties (absorption and reduced scattering) can be extracted from each pixel in the image using a Monte-Carlo based look-up table method.[28] This methodology has been implemented in multiple in vivo studies and has potential applications in subsurface tomography.[36–38,60,61] For this study, we used the OxImager RS SFDI system (Modulated Imaging Inc., Irvine, CA). This system provides LED illumination at up to 11 wavelengths spanning the visible to NIR and images with a 15 cm × 15 cm field of view. The system response is determined with the use of a calibration silicone phantom of known optical properties. For data processing, both height and angle correction of SFDI are applied.[29] For this study, SFDI measurements were taken at 526 nm, near the peak absorbance of both fluorophores tested, and at 591 nm, in the emission

band of the fluorophores. The same light source and camera were used to collect planar fluorescence images with the addition of a cleanup bandpass filter with a center wavelength at 534 nm and a 30 nm passband. A longpass filter with a cutoff wavelength of 561 nm was used in the emission band.

While there are a variety of models available to extract quantitative fluorescence, in this work we utilized the model developed by Gardner et al.[46,60,63] This model is an empirical approach based on semi-infinite, homogeneous Monte Carlo simulations. It accounts for the presence of tissue absorption and reduced scattering, assumes planar illumination, and is simplified to a one-dimensional (1D) problem. This model can be applied to an imaging geometry by separately analyzing each image pixel.[36] SFDI provides μ_a and μ_s' at both excitation and emission wavelengths, which are used as inputs to the model to calculate a fluorescence attenuation correction factor. This factor accounts for optical absorption and scattering, and is applied to a raw fluorescence planar image. The fluorescence correction factor X_{1D} is determined as follows:

$$X_{1D}(\lambda_{ex},\lambda_{em}) = \frac{C_1(\lambda_{ex})C_3(\lambda_{em})}{k_1(\lambda_{ex})/\delta(\lambda_{ex}) + k_3(\lambda_{em})/\delta(\lambda_{em})} - \frac{C_2(\lambda_{ex})C_3(\lambda_{em})}{k_2(\lambda_{ex})/\delta(\lambda_{ex}) + k_3(\lambda_{em})/\delta(\lambda_{em})}$$

C_n and k_n are defined in Table 1 of Gardner et al. as empirical coefficients.[61] They are dependent on the diffuse reflectance R_d. Since R_d is a function of μ_a and μ_s', it can be calculated from the values determined by SFDI measurement. δ refers to optical penetration depth, which is calculated from μ_a and μ_s': $\delta(\lambda) = 1/\sqrt{3\mu_a(\lambda)[\mu_a(\lambda) + \mu_s'(\lambda)]}$.

A flowchart of QYI data processing is shown in Fig. 3.2.1. In general, the determination of an unknown QY requires knowledge of the fluorophore concentration, a

planar fluorescence map corrected for background optical properties, and the instrument response, which is a function of detector sensitivity, imaging geometry, and other instrument related parameters. In order to determine the unknown QY of a sample, the instrument response is first determined from a calibration phantom with known QY and known fluorophore concentration (top box of Fig. 3.2.1). This instrument response is then applied to the sample with unknown QY (bottom box of Fig. 3.2.1). More specifically, first a calibration phantom with known QY is fabricated and SFDI is used to quantify the background optical properties of the diffuse sample over a wide-field area at both the absorption and emission wavelengths for a specific fluorophore. Then, SFDI is used again to determine the additional absorption ($\Delta\mu_a$) at the excitation wavelength caused by the addition of an exogenous fluorophore to the sample. This $\Delta\mu_a$ is used to determine the concentration of the added fluorophore based on the known extinction coefficient at the excitation wavelength. The same information is also extracted from a sample phantom (with unknown QY). The background μ_a, μ_s', and planar fluorescence data are then input into the Gardner model to produce a corrected fluorescence map. The corrected fluorescence map and the calculated probe concentration of the calibration phantom are compared to those of the sample phantom, so that the fluorophores QY can be extracted and mapped over a heterogeneous sample. It is important to note that this methodology requires a stable absorption cross-section regardless of environmental conditions so that the probe concentration can be calculated despite any changes in QY. Both fluorophores used in this study fit this criterion for the absorption wavelengths used.

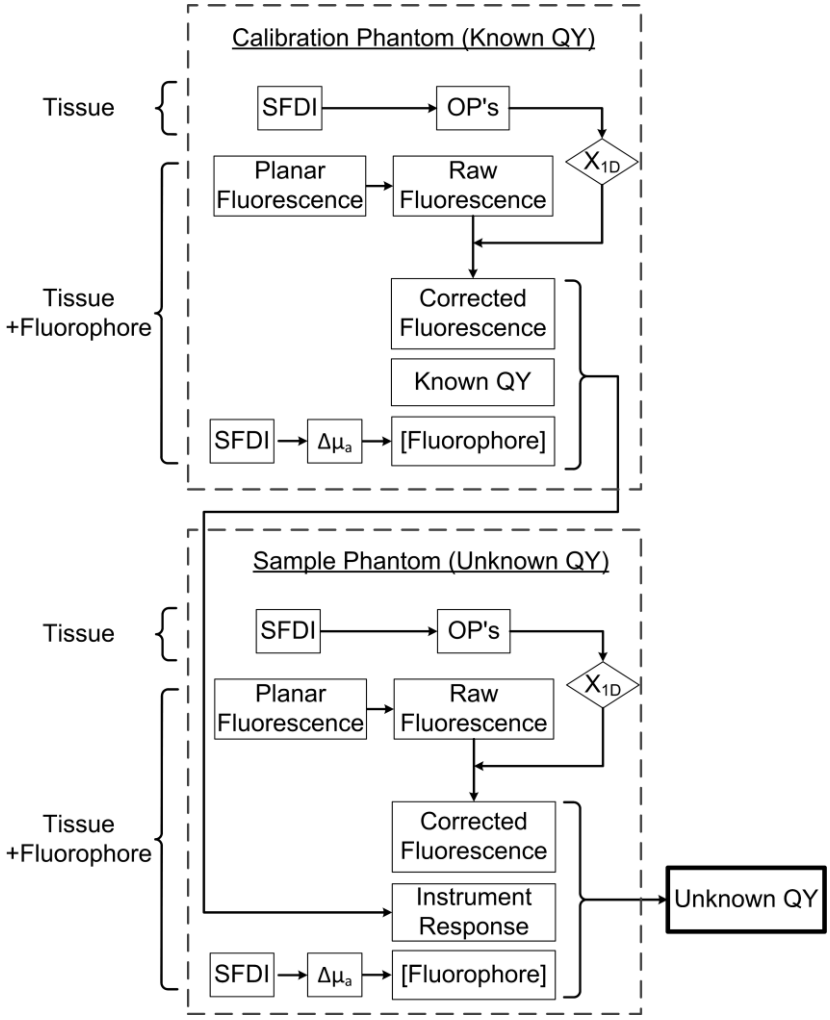

Figure 3.2.1: Flowchart of quantum yield imaging data processing. X_{1D} is the fluorescent correction factor. [Fluorophore] indicated the extracted fluorophore concentration.

The QY of many fluorescent dyes is known to change under different environmental conditions. Previous studies have shown that the QY of rhodamine B is sensitive to solvent effects.[54] In mixed methanol-water solvents, its QY varies from 0.52 to 0.30 while the methanol-water volume ratio changes from 100:0 to 0:100.[54] SNARF-5 (Life Technologies, Carlsbad, CA) exhibits a significant pH-dependent emission shift between acidic and basic conditions and is commonly used as an intracellular pH indicator.[51] Both dyes were used to validate QYI.

The absorption and emission spectra of both fluorophores were measured with a spectrophotometer (Cary 100 Bio UV-Vis, Varian, Palo Alto, CA) and a fluorimeter (FluoroMax 3, Horiba, Kyoto, Japan), respectively. For rhodamine B, nine samples were made with varied methanol-water volume ratios (99:1, 90:10, 80:20, 70:30, 60:40, 50:50, 30:70, 10:90, and 0:100). For SNARF-5 measurements, nine samples with varied pH conditions were made (pH = 6.07, 6.39, 6.82, 7.11, 7.79, 8.13, 8.36, 8.88, and 9.30). The fluorophore concentration was 3 μM for all samples. For QYI experiments, measurements were conducted in liquid phantoms. The prepared liquid phantoms were poured into a 2.5 × 2.5 × 2 cm well embedded in a diffuse silicone phantom. In the rhodamine B experiments, the liquid phantoms had water/methanol mixtures as the solvent, nigrosin as absorber, and titanium dioxide as the scattering agent. For SNARF-5 experiments, phosphate buffered saline (PBS) was used as solvent due to its low solubility in water. Nigrosin was used as the absorber and 1.1 μm polystyrene microspheres as the scatterer, and pH was varied by adding either hydrogen chloride (HCl) or sodium hydroxide (NaOH). The background optical properties were adjusted by varying the amount of absorbers and scatterers.

3.3: Results

Fig. 3.3.1 shows the absorption spectrum of rhodamine B plotted from 450 nm to 650 nm, and the emission spectrum from 561 nm to 660 nm, with an excitation wavelength of 526 nm. 526 nm and 561 nm correspond to the center wavelength of the illumination LED in both SFDI and fluorescence modes, and the cutoff wavelength of the long-pass filter in fluorescence mode, respectively. The solvent methanol-water ratio was varied to

change the QY. Importantly, the absorption of rhodamine B was relatively stable while the emission changed dramatically with solvent.

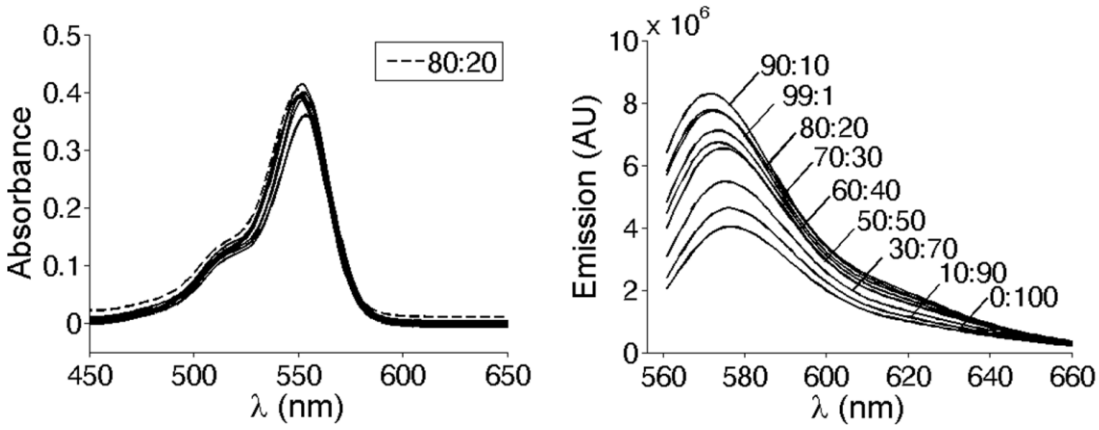

Figure 3.3.1: Rhodamine B excitation and emission spectra.

Liquid Phantom	Excitation wavelength: 526 nm	
	μ_a (mm^{-1})	**μ_s' (mm^{-1})**
Phantom Set 1	0.028	0.55
Phantom Set 2	0.022	1.04
Phantom Set 3	0.051	0.53
Phantom Set 4	0.045	0.99
Phantom Set 5	0.074	0.51
Phantom Set 6	0.070	0.96

Table 1. Background optical properties of liquid phantoms (rhodamine B).

To validate the QYI method, a series of 54 liquid phantoms were prepared, each with different combination of solvent and optical properties. For simplicity, the concentration of rhodamine B was kept at 3 μM for all liquid phantoms. At each of the nine methanol-water mixture ratios (99:1, 90:10, 80:20, 70:30, 60:40, 50:50, 30:70, 10:90, and 0:100), six liquid phantoms of varied optical properties were made (Table 1). Note that the background optical properties of the liquid phantoms were measured without the presence of fluorescent dye, after which the dye was added to the liquid phantoms and then the fluorescence intensities were measured. The fluorophore concentration was calculated by comparing optical absorption at the excitation wavelength before and after adding the fluorophore, and with knowledge of rhodamine B's extinction coefficient at this wavelength. For each of the 54 liquid phantoms, the QY was determined by averaging within a region-of-interest (ROI) corresponding to each liquid phantom and comparing these to literature values as shown in Fig. 3.3.2. Each colored dot represents a separate liquid phantom and different dot colors correspond to unique excitation wavelength background optical properties. The solid black line indicates known QY's from literature.[54] Calculated QY's vary less than 10% from known values. Among the neighboring groups of the estimated QY's (grouped by solvent composition), the following pairs, 99:1/80:20, 80:20/60:40, 70:30/50:50, 50:50/30:70, 30:70/10:90, and 10:90/0:100, are statistically different, confirmed by Student's t-test (p-value < 0.05). Calibration phantoms were made with a 50:50 methanol/water ratio.

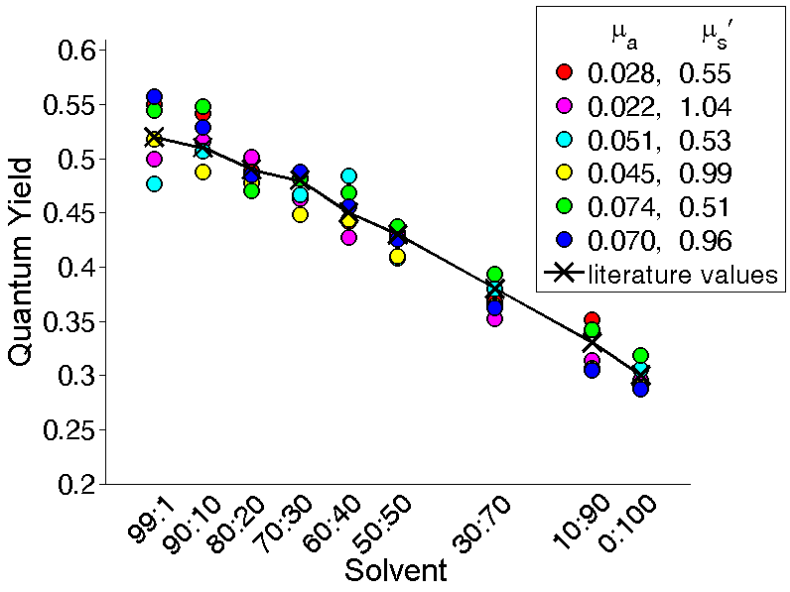

Figure 3.3.2: Measured quantum yields vs. literature values (rhodamine B).

The QYI method also allows spatial mapping of QY on pixel-by-pixel basis. A series of 9 liquid phantoms were made and poured into 9 wells embedded in a diffuse silicone phantom. These 9 phantoms were imaged with SFDI and planar fluorescence, and pixel-level QY information was extracted as shown in Fig. 3.3.3. The middle panel shows raw fluorescence, which is highest in the liquid phantoms with the lowest background absorption (middle panel, left column). The right panel shows QY spatial mapping, demonstrating that correct QY's can be extracted regardless of background optical properties. The predicted and measured average QY in each well were within a 10% agreement on average. The image processing for spatial mapping was performed in Matlab (Mathworks, Natick, MA). The optical property maps of the background phantom were denoised by a close operation with a disk-shape template of 5-pixel radius, followed by median filtering with a 5-by-5 neighborhood around each pixel. The computed QY maps were filtered by 10-by-10 median filtering. For the rhodamine B experiments, the overall

accuracy for QY determination was 0.021. This was calculated by determining the differences between the measured QY's and the literature values for each optical property combination, and then averaging over the entire experiment.

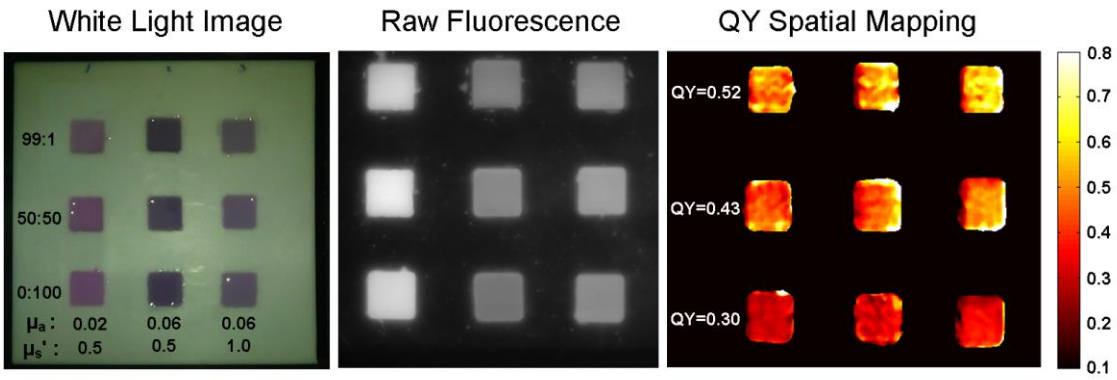

Figure 3.3.3: Spatial mapping of quantum yield (rhodamine B).

The QY of SNARF-5 was measured under varying pH conditions to demonstrate the ability of QYI to perform as a non-invasive pH indicator. First, the absorbance and emission spectra of SNARF-5 were measured under different pH conditions in non-diffuse media using a spectrophotometer and fluorimeter. Fig. 3.3.4 shows the absorption spectrum of SNARF-5 collected from 400 nm to 700 nm, and the emission spectrum from 561 nm to 850 nm, with excitation wavelength of 526 nm. The QY of SNARF-5 was calculated by comparing these measurements to the spectra of a rhodamine B sample with 50:50 methanol-water solvent compositions. The rhodamine B sample has a known QY and was measured under the same spectrophotometer and fluorimeter settings. Results are listed in Table 2, which shows that the QY of SNARF-5 becomes larger with increasing pH. Additionally, the QY plateaus at both high and low pH values.

pH	Quantum Yield
6.07	0.0586
6.39	0.0626
6.82	0.0744
7.11	0.0901
7.79	0.1511
8.13	0.1819
8.36	0.1953
8.88	0.2149
9.30	0.2209

Table 2. SNARF-5 quantum yields vs. pH.

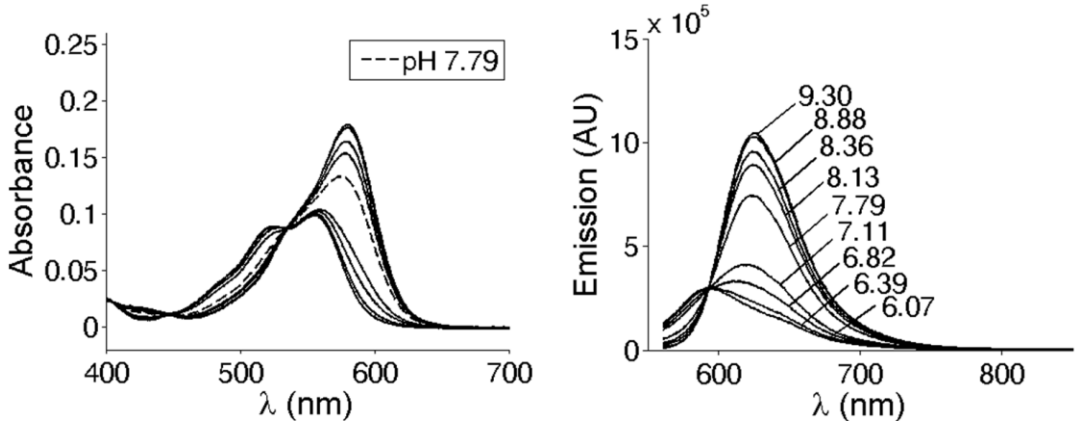

Figure 3.3.4: SNARF-5 excitation and emission spectra.

QYI imaging of SNARF-5 was tested in a 4x4 set of liquid phantoms, with four pH conditions (pH = 6.07, 7.11, 8.36, and 9.30) and four different background optical property combinations. The pH was measured with a pH meter (Oyster-10, Extech Instruments, Nashua, NH). The optical properties of each of the four liquid phantoms are shown in Table 3. For simplicity, the concentration of SNARF-5 was kept at 3 μM for all phantoms. QY's were extracted and compared to standard values, as shown in Fig. 3.3.5. Each colored dot in Fig. 3.3.5 represents a liquid phantom and dot color indicates a unique combination of background optical properties. Calculated QY's are within 20% of known values. This is inferior to the rhodamine B experiments (10%), likely due to the fact that SNARF-5 QY's are generally much lower than those of rhodamine B, leading to larger percent differences. Calibration phantoms had a pH of 7.79.

To demonstrate spatial mapping of QY for SNARF-5, a series of four liquid phantoms were measured, and pixel-level QY information was extracted, as shown in Fig. 3.3.6. The right panel shows QYI spatial mapping. For the wells in the right panel, top row, the measured average QY's are 0.22 and 0.26, with standard deviations (SD) of 0.025 and 0.024, respectively. The expected QY for this row, based on spectrophotometer and fluorimeter measurements, was 0.22. The average measured QY's of the bottom row are 0.032 (SD=0.0031) and 0.038 (SD=0.0048), while the expected QY was 0.059. In general, SNARF-5 QY's were determined with accuracy of 0.012 based on accuracy calculations averaged over all phantoms. The optical property and QY maps were processed in the same manner as described for rhodamine B experiments.

Liquid	Excitation wavelength: 526 nm	
Phantoms	μ_a **(mm^{-1})**	μ_s' **(mm^{-1})**
Phantom Set 1	0.018	0.39
Phantom Set 2	0.015	0.81
Phantom Set 3	0.031	0.38
Phantom Set 4	0.029	0.79

Table 3. Background optical properties of liquid phantoms (SNARF-5).

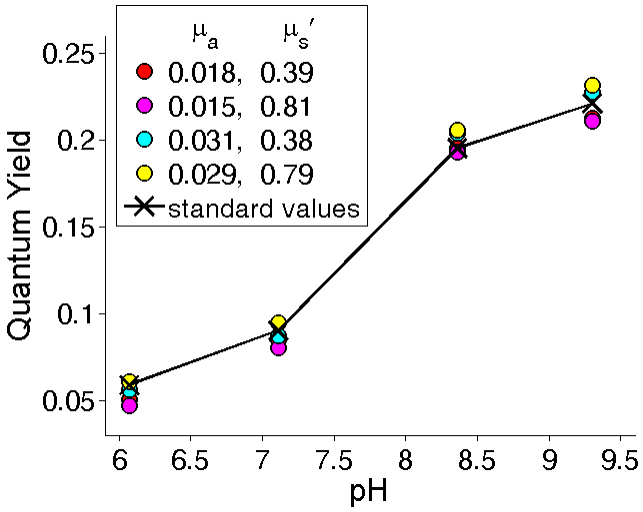

Figure 3.3.5: Measured quantum yields vs. standard values (SNARF-5).

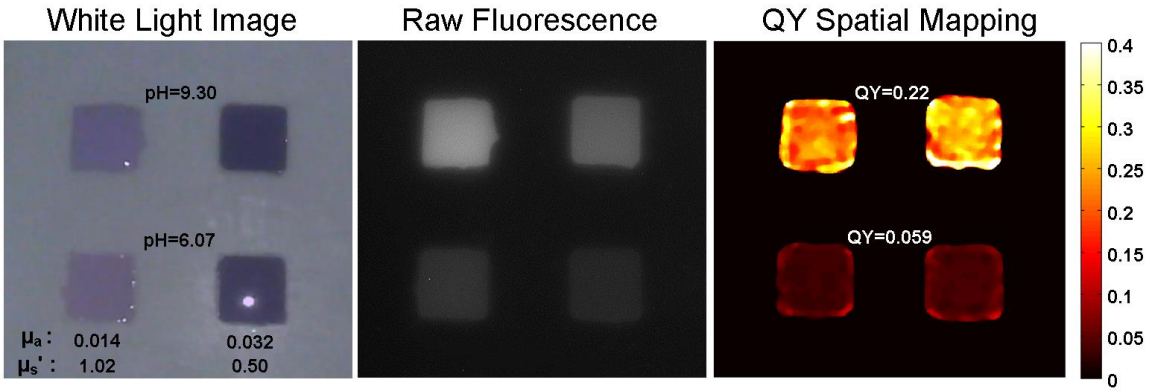

Figure 3.3.6: Spatial mapping of quantum yield (SNARF-5).

To illustrate a dynamic, time-varying spatial mapping of QY, a 160 ml liquid phantom was made in a 10.55 × 6.82 × 2.23 cm well embedded in a diffuse silicone phantom. SNARF-5 was added at a concentration of 3 μM, with phantom background optical properties of μ_a = 0.016 mm^{-1} and μ_s' = 0.533 mm^{-1} at 526 nm. Sequential ml samples of 1M HCl or 1M NaOH were added from the upper left corner of the well with a pipette. HCl/NaOH diffused through the media, causing the local pH of the liquid phantom to change, and consequently the local QY. After the diffusion process, the liquid phantom was manually mixed and the pH was measured with a pH probe for validation. During this process, QY maps were collected and made at 3 second intervals, each frame had an integration time of 2 seconds. In order to link sample pH values to QY measurements, a sigmoid function was used to fit to data from Table 2. The fitted function is as follows:

$$QY = 0.0548 + \frac{0.1692}{1 + 10^{1.0261(7.6727 - pH)}}$$

The pH of the sample was then extracted from QY values and a corresponding pH movie was created (supplemental Fig. 1 of the paper).[39] The pH was measured by the pH probe four times in total. Before adding any HCl/NaOH, the pH was measured as 7.54, and the average pH from the extracted QYI pH map was 7.46 (SD=0.11). After adding 0.64 ml 1M HCl and manual mixing, the pH was measured as 6.85, and the average pH from the pH QYI map was 6.74 (SD=0.17). Then, after adding another 0.64 ml 1M HCl and the manual mixing, the pH was measured as 6.17, and the average pH from the pH map was 4.58 (SD=0.55). In the end after adding 1.28 ml 1 M NaOH and manual mixing, the pH was measured as 7.54, and the average pH from the pH map was 7.41 (SD=0.16). This

dynamic process is shown in the supplemental movie 1 of the paper; Fig. 8 shows two frames from the movie.[39]

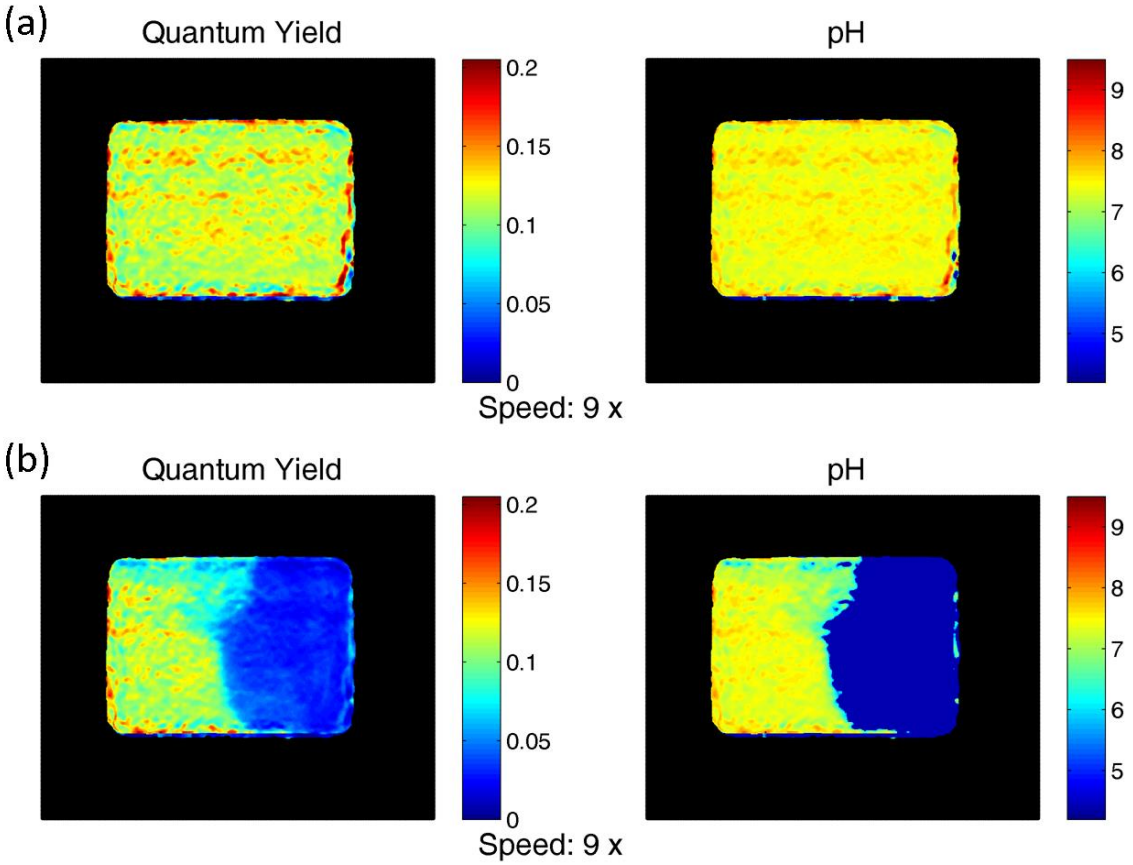

Figure 3.3.7: Frames from supplemental movie: dynamic spatial mapping of quantum yield and pH. The SNARF-5 concentration was 3 μM, with background optical properties of μ_a = 0.016 mm^{-1} and μ_s' = 0.533 mm^{-1} at 526 nm. QY maps were collected and made at 3 second intervals while the fluorescence images were taken with exposure time of 2 seconds. The supplemental video has 316 total frames. (a) Baseline, no acid/base added. The baseline pH was measured as 7.54 with pH probe. (b) After 1M HCL added by pipette at the surface of the liquid phantom, acid is diffusing through the media, reducing the QY and pH of the solution. The movie plays at a speed of 9 times of the actual process, hence the text "Speed: 9 ×".

3.4: Discussion

We have demonstrated a new imaging method, called QYI, which uses SFDI and planar fluorescence to extract QY values from a fluorescent dye within an optically

diffusive background. QYI extends prior quantitative fluorescence methods which assume a constant and known QY for a given fluorophores of interest.[28,61,62] By separately measuring fluorophore concentration in the relatively stable absorption band, we are able to determine the QY of the fluorophore by correcting raw planar fluorescence signal in the emission band, where fluorescence intensity changes greatly with environmental conditions. QYI was demonstrated using two fluorophores, rhodamine B and SNARF-5, which are sensitive to solvent and pH conditions respectively. The QY of these fluorophores was measured and validated in optical phantoms with different background optical properties. Additionally, pixel-level mapping of optical properties with SFDI allowed for spatial mapping of QY for both of the fluorophores. Finally, a supplemental movie was made showing dynamic changes of both QY and environmental pH values using the SNARF-5 dye.

The QY - pH relationship suggests one of the potential future applications of this method: mapping of local tissue pH *in vivo* using pH sensitive fluorophores. Due to absorption and scattering, measuring pH and other parameters is currently difficult in thick tissue. For example, pH is currently measured in tissue with either invasive probes or ratiometric pH dyes.[54,64] Invasive probes have limited applicability to longitudinal studies, and ratiometric dyes may be unreliable in thick tissue due to the wavelength dependence of optical properties. There has been some work done in using fluorescence lifetime measurements to determine pH conditions in tissue, but this requires relatively complex and expensive pulsed laser systems and time-correlated single photon counting techniques.[65] With QYI, quantitative pH can be non-invasively measured in thick tissue

with pH sensitive dyes. Moreover, fluorophores which are sensitive to temperature, oxygen content, or protein binding can also be used with QYI, potentially allowing a variety of microenvironmental conditions to be determined non-invasively.

Several assumptions were made in this study in order to simplify the processing required to generate QYI maps, and there are limitations to the use of this methodology for certain applications. For example, the Gardner model assumes homogeneity in depth, which may limit the method's use for some *in vivo* applications. Additionally, QYI requires the use of a dye with a stable absorption band, which was the case for both rhodamine B and SNARF-5 at the wavelengths used here, but does not apply for all molecular imaging agents. Additionally, SFDI measurements were required before and after adding the fluorophore to the diffuse background in order to determine the probe concentration prior to calculating the QY, limiting the use of QYI for some real-time applications. Despite these requirements and limitations, QYI imaging should still be useful for *in vivo* preclinical imaging, and the methodology is amenable to the use of more complex quantitative fluorescence models that would allow for tomographic reconstructions with depth resolved information. Additionally, these same methods are applicable to quantitative spectroscopic modalities such as frequency and time-domain diffuse optical systems if combined with fluorescent measurements, providing deeper tissue depth penetration and possible *in vivo* human applications.

In summary, QYI is able to extract fluorophore QY regardless of background optical properties, highlighting the possibility of using QYI with environmentally sensitive fluorophores to create novel biomarkers to probe tissue microenvironment *in vivo*.

3.5: Acknowledgements

The authors wish to thank Irving Bigio, Amaan Mazhar, David Cuccia, and Bruce Tromberg for their helpful discussions. The authors gratefully acknowledge funding from the American Cancer Society (Grant RSG-14-014-01-CCE).

CHAPTER FOUR: IMAGE ARTIFACT CORRECTION IN SPATIAL FREQUENCY DOMAIN IMAGING (SFDI) FOR SMALL ANIMAL IMAGING

While SFDI is able to provide quantitative tissue optical properties, it has limitations when used on objects with highly curved surface. For example, SFDI is currently being explored for small animal tumor imaging, but severe imaging artifacts occur for highly curved surfaces (e.g. the tumor edge). We propose a modified Lambertian angle correction, adapted from the Minnaert correction method for satellite imagery, to account for tissue surface normals up to 75°. The method was tested in a hemisphere phantom study as well as a small animal tumor model. The proposed method reduced μ_a and μ_s' extraction errors by an average of 64% and 16% respectively compared to performing no angle correction, and provided more physiologically agreeable optical property and chromophore values on tumors.

The work in Chapter Four is published in the Biomedical Optics Express [66] with the following contributing authors:

Yanyu Zhao,[1] Syeda Tabassum,[2] Shaheer Piracha,[1] Mohan Sobhana Nandhu,[3] Mariano Viapiano,[3] and Darren Roblyer[1]

[1] Boston University, Department of Biomedical Engineering, 44 Cummington Mall, Boston, Massachusetts 02215, United States

[2] Boston University, Department of Electrical & Computer Engineering, 8 Saint Mary's Street, Boston, Massachusetts 02215, United States

[3] Brigham and Women's Hospital, Harvard Medical School, 4 Blackfan Circle, Boston, Massachusetts 02115, United States

4.1 Introduction

Spatial Frequency Domain Imaging (SFDI) is a wide-field imaging technique that can be used to quantify optical properties (absorption and reduced scattering) of diffusive media including biological tissue.[26,27] When optical properties at multiple wavelengths are measured, tissue chromophore concentrations can be extracted to help identify disease states, therapy response, and tissue metabolic function. SFDI is being explored for a number of preclinical and clinical applications, including skin flap viability, burn wound healing, and subsurface tomography.[30–43]

Recently, our group and others have begun to investigate SFDI as a new tool to understand the *in vivo* tumor state in small animal oncology models. The application of SFDI to small animal imaging is complicated by the relatively small feature size of the tissues of interest, and the relative high surface curvature of subcutaneous tumors, which may protrude near-orthogonal to surrounding tissue for some models. Observationally, tumor edges, and other surfaces with a high surface normal angle in reference to the camera line of sight, suffer from extreme edge artifacts in SFDI, leading to physiologically implausible optical properties and chromophore concentrations in these regions. Typically, these artifacts manifest as underestimates of diffuse reflectance at low spatial frequencies. One potential method to mitigate these artifacts is to eliminate these steep surfaces from the data using a threshold method based on tissue angle. Unfortunately, this has the effect of censoring large parts of the tumor, which may be unacceptable for many applications.

Gioux *et al*. reported a Lambertian correction method for SFDI which could mitigate edge imaging artifacts for surface angles up to 40°.[29] For this method, a cosine

divisor term was applied to SFDI data after image demodulation to increase diffuse reflectance values for surfaces at tilt angles. This method was shown to improve optical property extraction on tissue-simulating phantoms and human hand data, although corrections were limited to angles less than 40°. We expand on this work by applying the so-called Minnaert Correction, which was first proposed for lunar photometry and later developed to angle-correct satellite imagery from the effects of solar illumination angles and relative terrain angles.[67,68] In the context of SFDI measurements, we refer to this correction as the Modified Lambertian Correction (MLC). The MLC is a parameter optimization method that adds an additional correction factor to the Lambertian correction by empirically accounting for inter-object diffuse reflectance (e.g. light reflected off surrounding normal tissue onto the tumor), as well as other possible contributions to inaccurate diffuse reflectance values, especially near the tumor edge.

To validate the MLC method, SFDI measurements were taken on hemispheric tissue-simulating optical phantoms with a range of optical properties and different sizes, fabricated to mimic the geometry of subcutaneous xenografted tumors. The MLC method was compared against non-angle and the standard Lambertian correction for both lower angles (<40°) and higher angles (up to 75°). Additionally, MLC was applied to live mouse tumor data. Experimental results show that MLC yields similar improvements compared to standard Lambertian correction for low angles, and outperforms no-angle correction and standard Lambertian correction at higher angles, and MLC provides more physiologically reasonable optical property and chromophore values on live mouse tumor data, especially at the tumor edge, as will be reported here.

4.2 Methods

4.2.1: Spatial Frequency Domain Imaging (SFDI)

The details of SFDI image acquisition and processing have been described in detail elsewhere.[26,27] Briefly, SFDI utilizes spatially modulated sinusoidal light patterns of visible or near-infrared light, projected at different spatial frequencies and wavelengths, to separate the relative contributions of absorption and scattering in diffusive media. Raw reflectance images are sequentially measured, demodulated, and calibrated to create diffuse reflectance maps, with pixel values normalized between 0 and 1. Diffuse reflectance (R_d) maps are created for each wavelength and each spatial frequency. The spatial frequency dependence of R_d at each pixel (i.e. the Modulation Transfer Function) then serves as the input to an inverse model, in this case a Monte-Carlo based look-up table method, which provides pixel-by-pixel optical absorption and reduced scattering values.[28]

Key to the extraction of normalized R_d maps is the calibration of the demodulated raw image data (M_{ac}) against a calibration phantom with known optical properties. The calibration phantom is first measured with the SFDI system, and a forward model is used to determine the expected R_d values based on prior optical property knowledge. A second phantom or tissue-of-interest (with unknown optical properties), is then imaged using the same spatial frequencies and wavelengths, and calibrated R_d maps are produced using Eq. (1), which removes the instrument response.

$$R_{d,tis}(f_x) = \frac{M_{ac,tis}(f_x)}{M_{ac,ref}(f_x)} R_{d,ref}(f_x). \qquad (1)$$

R_d and M_{ac} refer to diffuse reflectance and demodulated maps, respectively, and subscripts

tis and ref refer to the tissue and calibration phantom, respectively.[27]

4.2.2: Height correction

In order to account for reflectance intensity perturbations caused by height variation, a previously described height correction method was used.[29] Briefly, a calibration phantom is measured at multiple heights and the demodulated data (M_{ac}) at each height is extracted. Then, a height map of the object or tissue of interest is acquired using optical profilometry. A new $M_{ac,ref}$ map is then calculated by adjusting the M_{ac} values, pixel by pixel, according to the height versus M_{ac} relationship determined from the multi-height calibration measurements. This M_{ac} data is used to replace the calibration $M_{ac,ref}$ term in Eq. (1). The effect of height correction is to create a virtual calibration phantom such that it has the same pixel-wise height as the object.

4.2.3: Modified Lambertian Correction (MLC)

In prior work by Gioux et. al.,[29] a Lambertian angle correction was applied as a cosine term to the demodulated raw data of the tissue-of-interest, as shown in Eq. (2).

$$M_{AC,corrected} = M_{AC,uncorrected} \times \frac{1}{\cos(\theta)}. \qquad (2)$$

The angle, θ, refers to the tilt angle of a flat phantom, or more generally, the angle of the tissue/phantom surface normal relative to the camera axis as shown in Figure 4.2.1. θ is determined for each pixel in the image using an optical profilometry methodology previously described.[29] The Lambertian correction increases the demodulated image intensity for surfaces at higher surface normal angles.

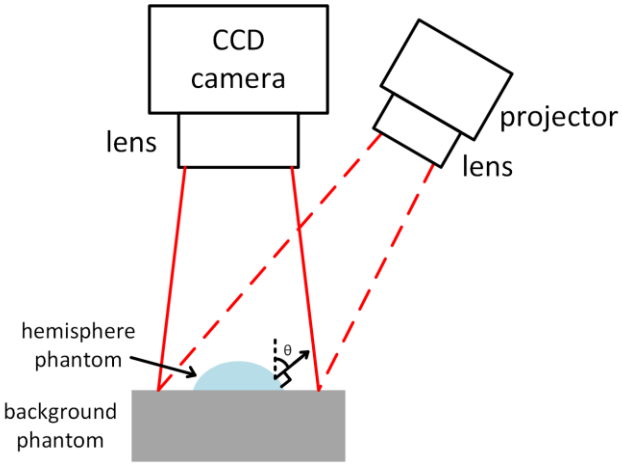

Figure 4.2.1: Diagram of angle θ in SFDI imaging geometry.

The proposed MLC method adds a coefficient *k* to the cosine term, as shown in Eq. (3). This coefficient accounts for the object-to-object diffuse reflectance (i.e. reflectance from an object's background onto the object), and potentially other phenomenon not accounted for by the standard Lambertian method. When *k* is equal to 0, no angle correction occurs, and when *k* is 1, the MLC is equivalent to the standard Lambertian correction.

$$M_{AC,corrected} = M_{AC,uncorrected} \times \frac{1}{\cos(\theta)^k}. \qquad (3)$$

In order to find an appropriate coefficient *k* for each M_{ac} map of an object-of-interest, we propose a parameter optimization method (Eq. 4). Note that for SFDI, there is a demodulated M_{ac} map for each spatial frequency and wavelength, and the coefficient *k* is different for each demodulated map.

$$k = \arg\min_{k\in[0,1]} \sum_{i=1}^{n} \left(M_{ac}(f_x)_i \frac{1}{\cos(\theta_i)^k} - M_{ac,ref} \right)^2 \qquad (4)$$

In Eq. 4, f_x, θ, i, and n refer to spatial frequency, surface angle at the pixel location, pixel index, and total number of pixels in the optimization region of interest (ROI), respectively. The ROI (i.e. the tumor) is manually selected on the uncorrected M_{ac} map. $M_{ac,\,ref}$ is the average M_{ac} value of the low-angle areas with ≤10° thresholding within the ROI. It is used as a "gold standard" M_{ac} for the minimization. In a practical sense, the low-angle area is a region of the ROI where surface angle effects are minimal. The parameter optimization will find the k value that minimizes the difference between MLC-corrected M_{ac} and $M_{ac,ref}$ for the ROI. The optimization is solved using Newton's method.[69] The determined k value is then applied to all pixels on the object to get the corrected Mac map. A different k value is determined for each spatial frequency and wavelength. The corrected M_{ac} maps are used to calculate diffuse reflectance maps (Eq. 1), from which optical properties and chromophores are determined using Monte-Carlo look-up table method and linear fitting, respectively.

4.2.4: Experimental validation

The OxImager RS SFDI system (Modulated Imaging Inc., Irvine, CA) was used for all optical measurements in this study. This system provides LED illumination at up to 11 wavelengths spanning the visible to NIR and images with a 15 cm × 20 cm field of view. Height correction is applied in data processing.[29] SFDI measurements were taken at 526 nm and 659 nm for phantom studies, and a series of spatial frequencies were used: 0, 0.05, 0.1, 0.15, 0.2, 0.3, and 0.5 mm^{-1}. The integration time of each image is adjusted from tens to hundreds of milliseconds to utilize the dynamic range of the camera.

Non-angle corrected, standard Lambertian, and MLC angle corrected SFDI

measurements were compared using a set of hemisphere tissue-simulating optical phantoms. The hemispheres were fabricated using silicone as the base solvent, Nigrosin as the absorber, and titanium dioxide (TiO_2) as the scatterer. Hemispheres were made with diameters of 1 cm, 2 cm, or 3 cm. These diameters were chosen to mimic the expected range of preclinical xenograft tumors. The maximum surface normal angle of the hemispheres was 75°. Hemispheres were made with a range of optical properties; each phantom was homogenous. The optical properties of the phantoms were adjusted by varying the amount of absorbers and scatterers.

First, the effect of different *k* coefficients on demodulated M_{ac} values for measurements on the hemispheres were compared over a line profile taken through the center of the hemisphere. Then, the relationship between spatial frequency and optimized *k* values was explored for hemispheres of different sizes, optical properties, and for different background phantoms. Then, the root-mean-square-errors (RMSE) of extracted μa and μ_s' were compared for non-angle, standard Lambertian, and MLC correction methods for all hemispheres. Errors were compared over a small angle range (<40°), which matches the reported range for the standard Lambertian correction, as well as for the full angle range (up to 75°). For RMSE calculations, calculations were done using all pixels within the angle range being analyzed.

The angle correction methods were also compared on a mouse tumor model. A malignant glioma cell line (GBM34-Lum) were injected subcutaneously on the flank of a nude mouse. The tumor was treated with combination of temozolomide and the anti-angiogenic bevacizumab. The mouse was measured with SFDI under isofluorane

anesthesia, 4 days after the end of a treatment session, with a tumor size of 11.6 mm × 10.5 mm. The mouse was measured at 659 nm, 691 nm, 731 nm, and 851 nm illumination and tumor optical absorption and reduced scattering was extracted at these wavelengths. Tissue-level chromophore concentrations, including oxy and deoxyhemoglobin, were calculated using the extracted optical absorption by linear fitting. All animal procedures were approved by the Brigham and Women's Hospital Animal Care and Use Committee.

4.3 Results

4.3.1: Optical properties of fabricated hemisphere phantoms

Fig. 4.3.1 shows white light images and optical properties (at 526nm) of the 2 cm diameter hemisphere phantoms. Their optical properties at 526 nm and 659 nm are shown in Table 4. The 1 cm and 3 cm diameter hemispheres were made from the same phantom batch and had closely matching optical properties.

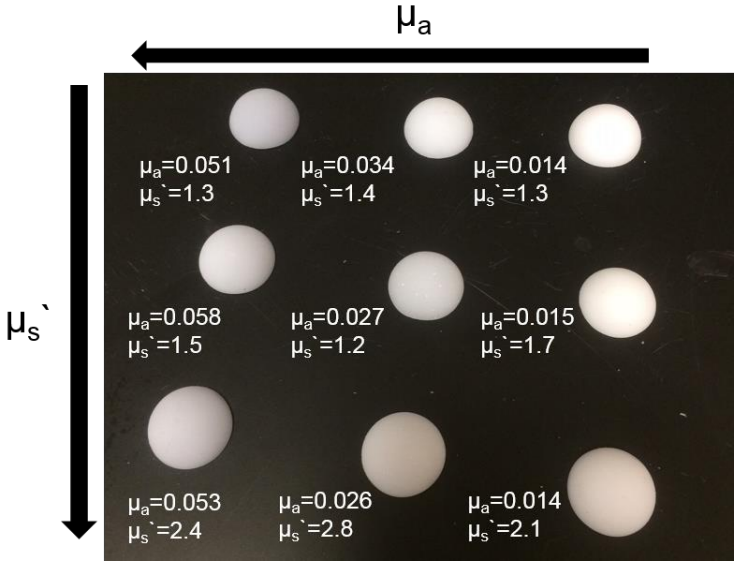

Figure 4.3.1: White light image of the 2 cm diameter hemisphere phantoms. Optical properties are shown for 526 nm.

λ	Hemisphere	#1	#2	#3	#4	#5	#6	#7	#8	#9
526 nm	μ_a (mm^{-1})	0.014	0.015	0.014	0.027	0.034	0.026	0.051	0.058	0.053
	μ_s` (mm^{-1})	1.3	1.7	2.1	1.2	1.4	2.8	1.3	1.5	2.4
659 nm	μ_a (mm^{-1})	0.019	0.020	0.019	0.037	0.032	0.036	0.066	0.069	0.068
	μ_s` (mm^{-1})	0.90	1.4	1.6	0.88	1.0	2.2	0.97	1.3	1.9

Table 4. Optical properties of the 2 cm diameter hemisphere phantoms. 1 cm and 3 cm hemispheres were fabricated from the same batch and had closely matching optical properties.

4.3.2: M_{ac} line profiles for varied k coefficients

The effect on angle corrected demodulated image data with different MLC *k* coefficients was first explored on hemispheric phantoms. Fig. 4.3.2 shows the line profiles of demodulated image data through the center of a 2 cm diameter optically diffusive homogeneous hemisphere phantom measured at 526 nm with optical properties of μ_a = 0.014 mm-1 and μ_s' = 1.3 mm^{-1}. The hemisphere was imaged on a flat background phantom with optical properties of μ_a = 0.053 mm-1 and μ_s' = 1.2 mm^{-1}. The left subfigure corresponds to SFDI data collected at 0 mm^{-1} spatial frequency (i.e. DC), whereas the right subfigure corresponds to 0.15 mm^{-1}. The dashed black line in the figure represents the expected M_{ac} value (i.e. the "gold standard" value) determined by the average M_{ac} of the low-angle areas with ≤10° thresholding. The colored lines correspond to angle-corrected data with different *k* coefficient values ranging from 0 to 1.

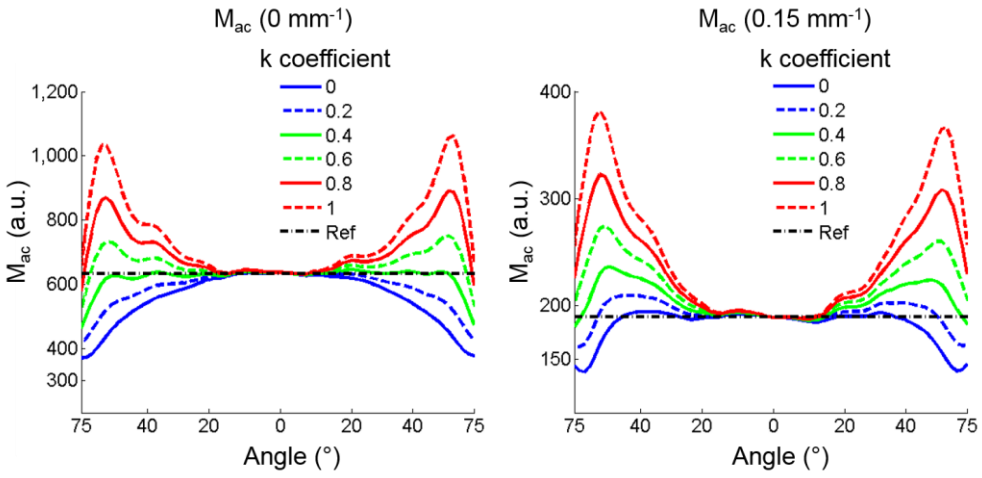

Figure 4.3.2: Angle-corrected M_{ac} versus coefficient k.

The solid blue line represents the demodulated intensity without any angle correction (k=0). For the 0 mm^{-1} spatial frequency (Fig 4.3.2. Left), M_{ac} values are increasingly under-reported as the hemisphere surface normal angle increases from 0° (the center of the hemisphere) to 75° (the distal edge of the hemisphere). The red dashed line shows Lambertian correction (k=1), which substantially over-corrects the demodulated intensity. For the higher spatial frequency, 0.15 mm^{-1} (Fig 4.3.2. Right), non-angle corrected (k=0) provides a better match to the expected M_{ac} than Lambertian correction (k=1) or other non-zero k values. In general, Fig. 4.3.2 visually supports the idea that some ideal k coefficient exists, which is spatial frequency dependent, which can minimize angle artifacts for homogenous hemispheric phantoms.

4.3.3: k coefficient determined by parameter optimization

The effect of spatial frequency and object (hemisphere) and background optical properties on the choice of k coefficient was explored. Fig. 4.3.3 shows the MLC

coefficient *k* for a range of spatial frequencies determined by the parameter optimization. For the left subfigure, a 2 cm diameter hemisphere phantom (μ_a = 0.068 mm^{-1}, μ_s' = 1.9 mm^{-1}) was placed on five background phantoms with different optical properties. Each combination was measured with SFDI at 659 nm. Each line in the left subfigure represents a distinct background optical phantom whose optical properties are listed in the legend. The solid blackline represents a black background phantom, which has strong absorption and little scattering. The left subfigure shows that the coefficient *k* approaches 0 at higher spatial frequencies regardless of the optical properties of the background phantom. With a black background, *k* approaches 1 (Lambertian correction) for low spatial frequencies. For the right subfigure, six 2 cm diameter hemisphere phantoms with different optical properties were measured on the same background phantom (μ_a = 0.053 mm^{-1}, μ_s' = 1.2 mm^{-1}). Fig. 4.3.3 shows that higher overall hemisphere optical attenuation requires higher *k* values and that *k* values are dependent on object optical properties and imaging spatial frequency.

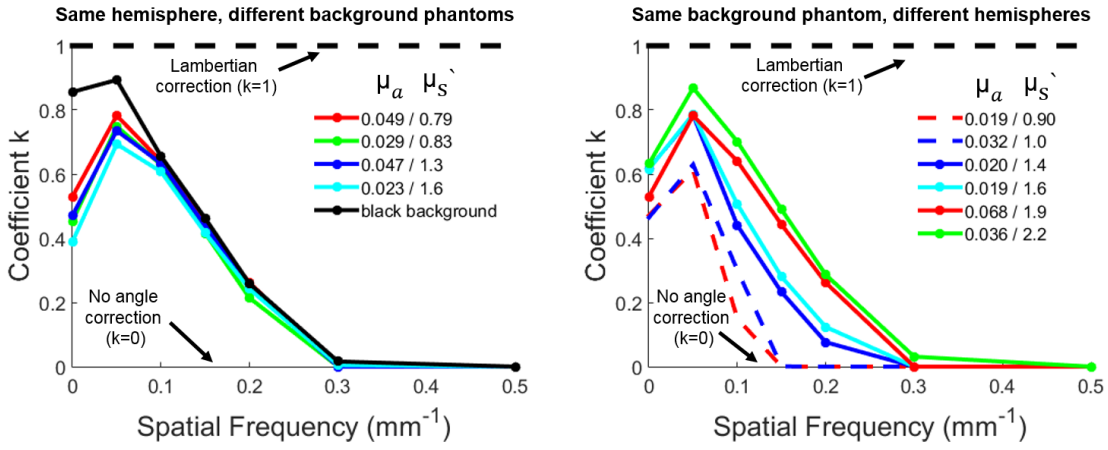

Figure 4.3.3: Coefficient *k* versus spatial frequency.

4.3.4: Comparison of non-angle, standard Lambertian, and MLC on hemisphere phantoms

Comparisons were made between errors in optical property extractions for non-angle, standard Lambertian, and the MLC method. Fig. 4.3.4 shows the line profiles of the absorption and reduced scattering through the center of a 2 cm diameter hemisphere placed on a background phantom (μ_a = 0.053 mm^{-1}, μ_s' = 1.2 mm^{-1}) measured at 526 nm. The dashed black line represents the expected μ_a / μ_s' values ("gold standard"). The dashed blue line, dashed green line, and solid red line correspond to non-angle, standard Lambertian, and MLC corrected μ_a / μ_s' data, respectively. For absorption, non-angle correction leads to overestimation of μ_a, while the Lambertian correction underestimates μ_a, causing it to be near 0 at the edges of the hemisphere (high angle areas). The MLC corrected μ_a is very close to the gold standard, outperforming the other two methods. For the reduced scattering, the non-angle correction and MLC are nearly identical, and both outperform standard Lambertian.

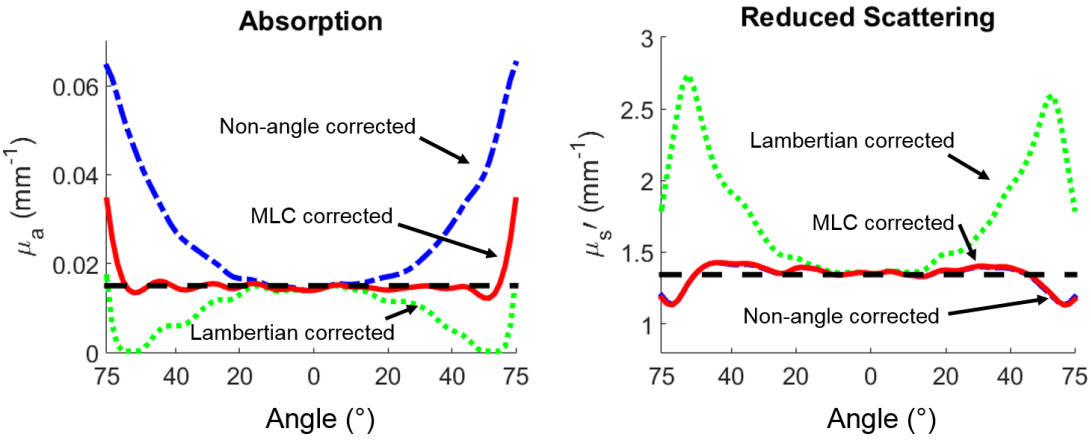

Figure 4.3.4: Line profiles of absorption and reduced scattering through the center of a 2 cm diameter hemisphere using different angle correction methods.

Fig. 4.3.5 shows 3D absorption and reduced scattering maps rendered for the same hemisphere and background phantom. The black arrows indicate the "gold standard" μ_a / μ_s' values. The 3D visualizations and histograms demonstrate that non-angle corrected data skews towards μa values higher than the known value at high angles, and the standard Lambertian correction skews towards lower μa values at high angles. Lambertian correction also overestimates μ_s' at high angles, whereas MLC gives μ_a and μs' values that are close to the "gold standard". It is of note that standard Lambertian correction produces a substantial number of pixels with μa values close to 0 mm^{-1}, and μ_s' values close to 2 mm^{-1}, the upper limit of displayed values. In contrast, the MLC data have a tighter distribution around the gold standard values, with modest μ_a underestimates at the extreme hemisphere edge.

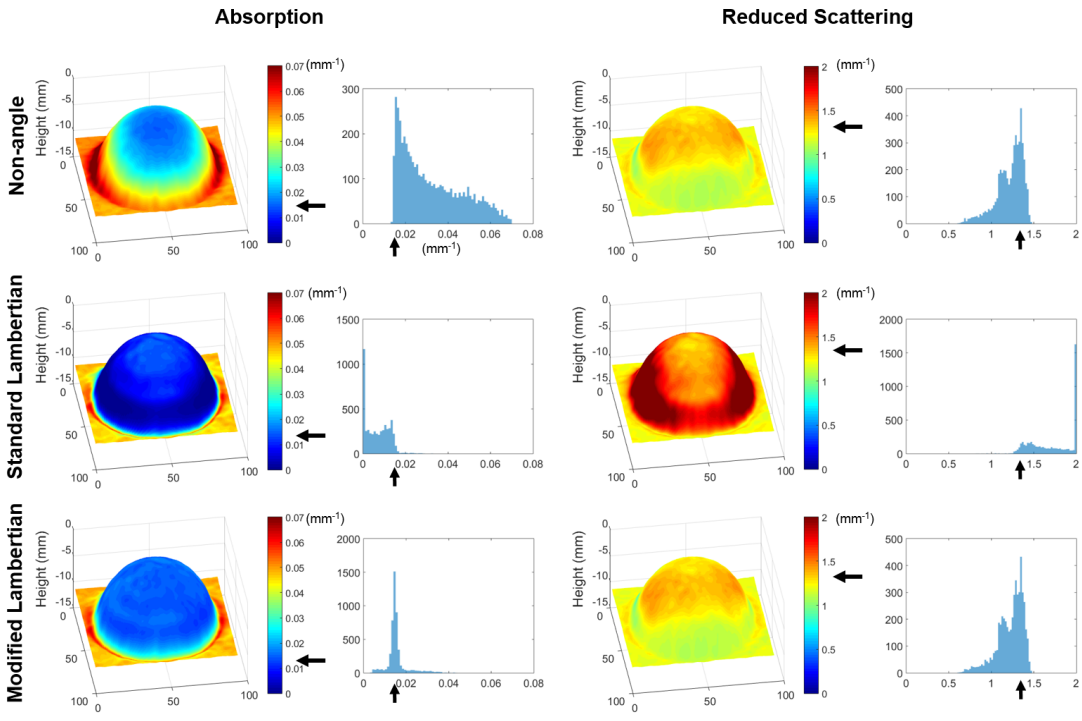

Figure 4.3.5: Absorption and reduced scattering plots rendered with 3D heights, and histograms of the hemisphere region. Optical properties are shown for a 2 cm diameter hemisphere at 526 nm.

To quantitatively compare non-angle, standard Lambertian, and MLC correction methods, groups of hemisphere phantoms with different sizes and optical properties were measured at 526 nm and 659 nm. Their μ_a and μ_s' values were extracted, the three correction methods were applied, and the root-mean-square-errors (RMSE) were calculated for both low angles (<40°), and higher angles (up to 75°). Representative RMSE values for the larger angle range (up to 75°) are shown in Fig. 4.3.6. Values are plotted as bar plots representing the error between the known optical properties and the corrected optical properties over the entire hemisphere. This group has nine middle size hemisphere phantoms (2 cm diameter), measured at 659 nm. The average μ_a RMSE of non-angle, standard Lambertian, and MLC of this group was 0.026, 0.017, and 0.008 mm^{-1}, respectively. For μ_s' the average RMSE for the three methods was 0.295, 0.387, and 0.256 mm^{-1}, respectively. The MLC method reduces the μ_a RMSE by 68.9% and 52.4% respectively over non-angle and standard Lambertian correction, and reduces the μ_s' RMSE by 13.2% and 33.9% respectively.

Comparing the three methods for angles less than 40° across all hemispheres (n=27) and background phantoms (n=5), the overall average μ_a RMSE of non-angle, standard Lambertian, and MLC was 0.0094, 0.0063, and 0.0052 mm^{-1}, respectively. For μ_s' the overall average RMSE for the three methods for angles less than 40° was 0.16, 0.20, and 0.15 mm^{-1}, respectively. These results demonstrate improved but comparable error levels for the standard Lambertian and MLC methods for smaller angles.

The overall average μ_a RMSE for angles up to 75° across all hemispheres was 0.029, 0.019, and 0.010 mm^{-1}, respectively. For μ_s' the overall average RMSE for the three

methods was 0.250, 0.454, and 0.209 mm^{-1}, respectively. On average, the MLC method reduces the μ_a RMSE by 63.7% and 49.9% respectively over non-angle and standard Lambertian correction, and reduces the μ_s' RMSE by 15.9% and 51.9% respectively. In general, data from all measured hemispheres revealed that the MLC method greatly improved μ_a extractions over the other two methods for larger angles. For μ_s', MLC did little to improve non-angle correction, but as expected, outperformed standard Lambertian correction which is not valid at angles higher than 40°.

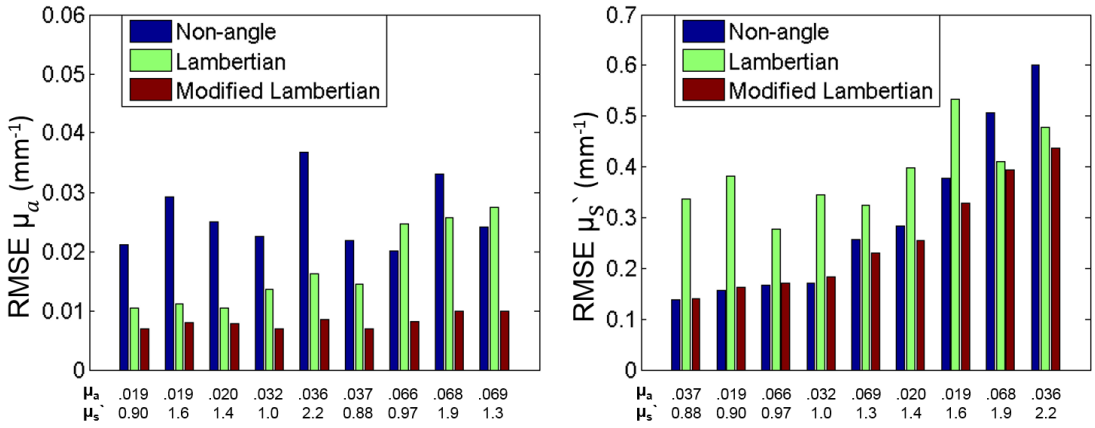

Figure 4.3.6: RMSE bar plots of 2 cm diameter hemisphere phantoms, measured at 659 nm.

4.3.5: Comparison of non-angle, standard Lambertian, and MLC on live mouse tumors

Fig. 4.3.7 compares non-angle, standard Lambertian, and MLC on a live mouse tumor model. The μ_a and total hemoglobin concentration were extracted using the three methods respectively. The extracted tumor data distributions are also presented in the histograms. For non-angle correction, the tumor absorption values skew higher on the edges (high angles), with corresponding higher estimated total hemoglobin concentrations. For standard Lambertian correction, a perimeter at the base of the tumor has 0 mm^{-1} μ_a

values, with corresponding 0 μM total hemoglobin values at these areas. Although "gold standard" values are not available for the mouse tumor, the extracted data distributions are tighter with the MLC method, and μ_a and total hemoglobin values are physiologically plausible throughout the tumor ROI.

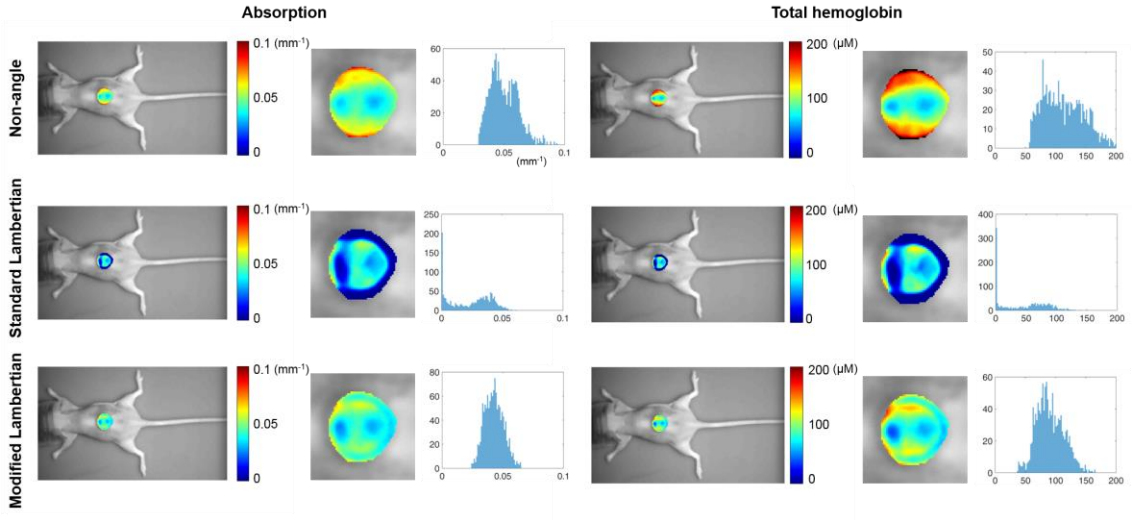

Figure 4.3.7: Comparison of three methods on mouse tumor data and their distributions shown in histograms, measured at 659nm, 691 nm, 731 nm, and 851 nm. The plotted absorption data was measured at 659 nm. Optical properties are only shown for the tumor ROI. Zoomed-in figures are shown for the tumor optical absorption and total hemoglobin.

4.4 Discussion and conclusion

MLC correction for SFDI reduced μ_a extraction errors over a range of phantom hemisphere dimensions and optical properties by an average of 63.7% compared to performing no angle correction. Additionally, in contrast to non-angle correction and standard Lambertian correction, MLC produced optical property and chromophore extractions that better match physiologically reasonable values on a xenograft mouse tumor model, especially at the tumor edge. The empirical approach taken here to determine *k* requires measurement of surface angle, but does not require explicit knowledge,

measurement, or input of background optical properties or instrument geometry, allowing it to be practically implemented in tumor monitoring studies regardless of specific instrument used and with little additional analysis effort.

The experiments performed in this study revealed that angle related effects in SFDI are dependent on the optical properties of the object of interest and background, the spatial frequency, the wavelength, and the imaging surface normal angle. For example, it was demonstrated that lower *k* values are required at high spatial frequencies, and almost no angle correction (k=0) was required for spatial frequencies of 0.3 mm^{-1} and above. This suggests that data collected at higher spatial frequencies are less affected by both Lambertian effects and inter-object reflections. Since higher spatial frequencies are preferentially sensitive to tissue optical scattering,[27,70] μ_s' data is preserved even without angle correction (i.e. $k = 0$), which was demonstrated by the relatively low RMSE values observed in scattering data when no angle correction was used. At DC, greater correction was required and *k* approached 1 (i.e. Lambertian correction) when the diffusive phantom was imaged on a dark, highly absorbing background. When hemisphere phantoms were imaged on a diffuse background, intermediate correction (i.e. $0 < k < 1$) was required as the standard Lambertian correction significantly overcorrected R_d values for surfaces at higher angles. This is likely due to the inter-object reflections occurring between the background phantom and the hemisphere, which increase measured light intensity at the hemisphere edge. These angle dependent inter-object reflections have previously been described in the context of correcting satellite imagery.[68] At low AC spatial frequencies (e.g. 0.05 mm^{-1}), higher *k*-values were needed, suggesting that Lambertian effects

dominate. Although not explicitly explored in this work, effects related to the increase in projected imaging spatial frequency on the highly curved surfaces likely contribute to edge effects.

There are several limitations of the MLC correction method related to the assumptions required for its implementation. For example, the MLC method assumes that the M_{ac} value of low-angle areas are representative of the entire region or object-of-interest, and large heterogeneities are likely to introduce errors. Specifically, under scenarios where low angle zones are not available or there are large inherent heterogeneities, the optimization could be invalid. Despite this limitation, MLC provided better optical property and chromophore extractions on actual tumors compared to non-angle or standard Lambertian corrections at the tumor edge. Another limitation is that the hemisphere phantoms tested here were fabricated with a maximum 75° surface normal relative the vertical since the angle dependence relationship of R_d above 75° deviated from the relationship observed below 75°, possible because of noise in the optical profilometry data or due to more complex interobject effects. It is of note that the mouse tumors imaged for this study had almost no pixels >75°, suggesting this may not be a limiting factor for small animal tumor imaging. Finally, MLC was only tested for a limited set of geometric shapes, and the method was tested only for corrections on a limited region-of-interest within the field-of-view (i.e. the tumor).

In the future, MLC will be tested for its ability to correct optical property extractions from more complex object geometries with spatially varying optical properties (i.e. an entire mouse). This is likely to require spatially varying k values, although the

general trends observed in this study relating k to object and background optically properties and spatial frequency may allow for simpler implementations under constrained conditions, such as a limited range of optical properties throughout the field-of-view and known background optical properties.

The MLC method described here is likely to be useful for small animal tumor imaging as it provides a relatively simple method to recover high-angle data that would otherwise have to be censored from the data set. The application of MLC to SFDI for longitudinal drug response studies in subcutaneous mouse tumor models may allow for the identification of prognostic optical biomarkers of therapy response and resistance that can then be translated to *in vivo* human imaging using SFDI and other diffuse optical imaging technologies.

4.5 Acknowledgments

The authors wish to thank Irving Bigio, Amaan Mazhar, and David Cuccia for their helpful discussions. The authors gratefully acknowledge funding from the American Cancer Society (Grant RSG-14-014-01-CCE), the Department of Defense (Award No. W81XWH-15-1-0070) and the Boston University/Brigham and Women's Hospital Collaborative Pilot Grant.

CHAPTER FIVE: LABEL-FREE, NON-INVASIVE MAPPING OF TISSUE WATER AND LIPID CONTENT

Non-invasive quantification of functional tissue biomarkers has broad implications in basic research, pre-clinical studies, and in clinical practice. Optical methods are well suited to this task, based on the characteristic absorption signatures of chromophores including oxy/deoxyhemoglobin, water, lipid, and glucose. Yet, quantitative in vivo mapping of biomarkers such as water and lipids still remains a challenge, due to turbidity of biological tissues and limited accessibility by NIR. Here, we demonstrate for the first time, a new method for label-free *in vivo* mapping of water and lipid with shortwave infrared (SWIR) structured illumination. We first validated the accuracy of extracting water and lipid concentrations in phantom models. We then examined the capabilities of our system in multiple pre-clinical and clinically-relevant settings. For example, we dynamically tracked the concentration of water (i.e. edema) in superficial tissues during induced inflammation in a small animal model. Next, we imaged water and lipids in preclinical tumors, and validated the results using histologic staining. Further, we identified in vivo small animal interscapular brown adipose tissues within intact skin, demonstrating the potential for longitudinal studies of obesity and thermoregulation. Finally, we highlighted monitoring of blood lipids content in human volunteers, and validated the results by blood draws and a lipid panel.

5.1: Label-free, Non-invasive Mapping of Water and Lipid Content in Tissue with shortwave-infrared SFDI

The work in part 5.1 is to be submitted to a scientific journal with the following contributing authors:

Yanyu Zhao,[1] Matthew Applegate,[1] John Jiang,[1] John Paul Dumas,[2] Mark Pierce,[2] and Darren Roblyer [1]

[1] *Boston University, Department of Biomedical Engineering, 44 Cummington Mall, Boston, Massachusetts 02215, United States*

[2] *Rutgers, The State University of New Jersey University, Department of Biomedical Engineering, 599 Taylor Road, Piscataway, New Jersey 08854, United States*

5.1: Introduction and Background

The ability to non-invasively map the concentration of functional tissue components with high spatio-temporal resolution is important in many areas of basic research, pre-clinical studies, and in clinical practice. Alterations in oxy/deoxy-hemoglobin, water, lipid, collagen, glucose, and other components are known to be implicated in major diseases including cancer, atherosclerosis, diabetes, and stroke.[2,5,22,23,71] Current methods for quantifying these components are often limited to single-point, spatially averaged values derived from extracted fluids and tissue samples.[72]

Optical spectroscopy has long been used to estimate the absorbance of species within dilute solutions, across the UV-VIS-NIR wavelength range. This approach has been extended to allow measurements in turbid media, including biological tissues *in vivo*.[8,73,74] Following measurement of the diffuse reflectance, analytical or numerical models are used

to determine the absorption and scattering coefficients of tissue. These techniques are most often implemented using fiber-optic probes to deliver light to and from the tissue, yielding a single measurement averaged over the volume of interrogated tissue.

Spatial frequency domain imaging (SFDI) is an emerging technique that allows for tissue absorption and reduced scattering coefficients to be quantitatively mapped across an entire region of tissue.[27] SFDI works by projecting structured illumination patterns onto the tissue surface, measuring the remitted light on a camera, and using a calibrated phantom to establish the diffuse reflectance of the tissue at each spatial frequency. Determining the diffuse reflectance at more than one spatial frequency allows tissue optical properties to be decoupled and quantified using an appropriate inverse model.

Absorption and reduced scattering spectra can be constructed with SFDI, again as spatially-resolved 2D maps. The measured absorption spectrum represents the combined effect of multiple absorbers within tissue, but if these components exhibit distinct absorption spectra, the measured spectrum can be decomposed into concentration-dependent contributions from the primary chromophores.[46]

To-date, SFDI has been implemented in the visible (VIS) and near-infrared (NIR) spectrum (400 – 900 nm). This has allowed in vivo wide-field mapping of oxy- and deoxy-hemoglobin as these chromophores have absorption spectra with distinct features in the NIR region.[41,43,75] However, other important biomarkers, including water, lipid, and collagen, lack distinct absorption features in the VIS-NIR, instead displaying strong absorption bands in the shortwave infrared (SWIR) region (900 – 2,000 nm).[47,76] Therefore, implementing SFDI at SWIR wavelengths has the potential to provide enhanced sensitivity

to these chromophores.

Previous attempts have been made to extend SFDI into the shortwave infrared range by extrapolating measurements from the NIR out to longer wavelengths.[77] However, the optical properties were fit by planar illumination rather than measured from structured illumination for most SWIR wavelengths. A few other works explored SFDI for extraction of water content.[30,78,79] However, validation (e.g. in phantom models) was yet conducted for such extraction of water contents. In addition, no lipid measurements were available in prior SFDI studies.

5.2: Methods and materials

Here, we demonstrate SFDI across VIS-NIR-SWIR wavelengths with 1 nm central wavelength resolution from 680 – 1,300 nm, as illustrated in Fig. 5.5.1a. A liquid phantom composed of blood, oil, and water is measured, as shown in Fig. 5.1.1b. Hyperspectral optical absorption cubes are generated for both NIR and SWIR wavelengths. The hemoglobin area shows distinct absorption features in the NIR, while the oil area shows maximum absorption at 1,210 nm in the SWIR. Absorption spectra are plotted in single pixel locations from blood, oil, and intralipid, respectively. It shows that blood has strong absorption in the NIR compared to water and lipid. In contrast, the oil area has the highest absorption at 1,210 nm, which corresponds to the lipid absorption peak in the SWIR wavelengths. With measured NIR absorption, maps of oxy-hemoglobin and deoxy-hemoglobin concentration can be reconstructed using Beer's law. The maps of water and lipid content, on the other hand, can be reconstructed with the SWIR absorption

information, as shown in Fig. 5.1.1c. We also conducted phantom studies to validate the concentration extraction of water and lipid. The measured absorption (μ_a) and reduced scattering (μ_s') spectra of a series of homogenous phantoms with varying water and lipid concentrations are shown in Fig 5.2.1a,b respectively. The extracted water and lipid concentrations are compared with known ground truth in Table 5. The average error for water concentration extraction is 1.9 %, and the average error for lipid is 1.1 %.

Intuitively, the reduced scattering should increase with increasing scattering content in optical phantoms. However, this is not the case for the lipid phantoms in Fig. 5.2.1 b. This is potentially due to particle interactions under relatively high concentrations or electric charges.[80] This could also be due to that the distance between particles is comparable or less than the wavelength under high scatterer concentrations. In addition, it has been shown in previous study that the reduced scattering of lipid phantoms may not increase with higher lipid content.[81]

The effective penetration depth of SFDI is dependent on tissue optical absorption and scattering: $(\lambda) = 1/\sqrt{3\mu_a(\lambda)[\mu_a(\lambda) + \mu_s'(\lambda)]}$,[27] the improved penetration depth was benefited from decreased scattering intensity at SWIR region. In addition, based on optical properties in literature, [78] we identified SWIR penetration window near 1,100 nm in bio-tissues (Fig. 5.2.2a). [82] This improved penetration depth at 1,100 nm was also confirmed with Monte Carlo simulations (Fig. 5.2.2b). To experimentally demonstrate the improved penetration depth within turbid media at SWIR region compared to NIR, we conducted a phantom study where tubes containing absorbing mixture were placed at depths from 1 mm to 4 mm within a homogenous absorbing and scattering liquid (Fig. 5.2.2c). The mixture

exhibits the same absorption at 680 nm and 1,100 nm, while the background liquid phantom also has the same absorption at 680 nm and 1,100 nm (Fig. 5.2.2d). The absorption maps and line profiles (Fig 5.2.2e,f respectively) show that absorption contrast can be measured at increased depths at 1,100 nm compared to at 680 nm. In addition, signal-to-background ratio (SBR) is quantitatively compared for the two wavelengths in Table 6. It shows that SBR can be increased with SWIR wavelength at all four tube depths. In particular, at 4 mm depth, while the NIR 680 nm can no longer detect absorption contrast, the 1,100 nm SWIR wavelength still has a 1.2 SBR.

In the rest of this work, we demonstrate longitudinal mapping of tissue water content in an *in vivo* small animal model of simulated edema as well as inflammation. We illustrate the use of SWIR-SFDI for measuring lipid biomarker in a tumor xenograft. In addition, we demonstrate the ability of SWIR-SFDI to non-invasively map brown adipose tissue (BAT) within intact skin in a small animal model, biomarker of topical relevance in the fields of body thermoregulation and metabolism. Finally, we highlight the capacity of SWIR-SFDI to non-invasively probe blood lipids in humans, verified with blood draw and lipid panel.

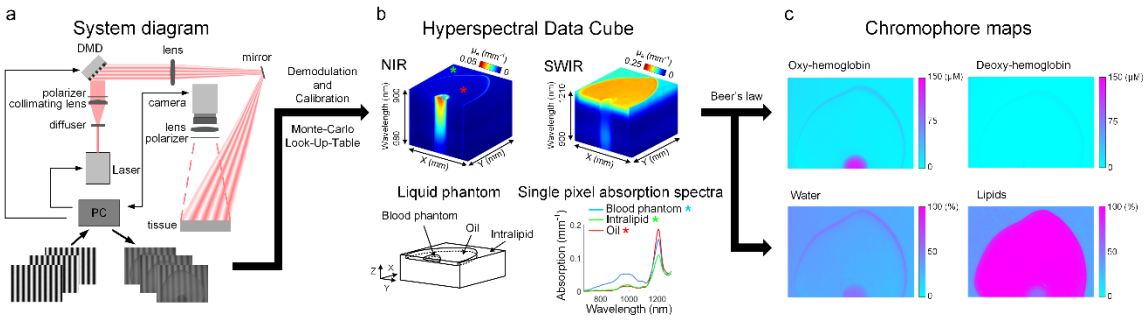

Figure 5.1.1: Hyperspectral SWIR-SFDI system and mapping of endogenous chromophores. In the system a collimated laser illuminates a digital micromirror device (DMD) which projects SWIR

structured illumination patterns at 0°, 120°, and 240° onto the sample plane. Backscattered light is collected by the camera. Orthogonal polarizers are positioned to remove specular reflection from images. The raw reflectance images are then demodulated, calibrated, and mapped with a Monte-Carlo Look-Up-Table to obtain optical properties (absorption and reduced scattering) at each wavelength. Here a liquid phantom is made by having soybean oil on top of intralipid, and a semi-circular blood phantom at the top of the oil. The liquid phantom is measured at both NIR and SWIR wavelengths and optical properties are extracted (shown for absorption). Hyperspectral absorption spectra at blood, oil, and intralipid locations are plotted respectively. Hemoglobin and lipid absorption features are clearly visible in the spectral plots. Chromophore maps for oxy-hemoglobin, deoxy-hemoglobin, water, and lipids can be extracted from the measured optical absorption.

5.2.1 Design of a hyperspectral SWIR-SFDI system

The system diagram and data processing steps are shown in Fig. 5.1.1a. The primary components of the system are an ultrafast pulsed laser, tunable from 680 – 1,300 nm in 1 nm increments (InSight DS+, Spectra-Physics, Santa Clara, California), a digital micro-mirror device (DMD) (CEL5500 Light Engine, Digital Light Innovations, Austin, Texas), and a TriWave germanium camera with spectral sensitivity over the 300 – 1,600 nm range (Infrared Laboratories, Inc., Peabody, MA). In order to reduce collection of specularly reflected light from samples, a linear polarizer (VersaLight™, Meadowlark) was placed in front of the projection lens, with a second polarizer, orthogonal to the first, in front of the camera lens.

While the laser operates as a mode-locked femtosecond pulsed source, it effectively serves as a continuous wave light source in the SWIR-SFDI setup, due to the camera integration times used. The output beam is expanded to a collimated diameter of 2.5 cm before illuminating the DMD, which is imaged on to the sample plane with ×8.3 magnification by a 75 mm focal length projection lens. Illumination is generated by programming the DMD with planar (DC, 0 mm^{-1}) and structured (sinusoidal, 0.1 mm^{-1}) patterns. Separate images are acquired as each pattern is projected on the sample plane with

0°, 120°, 240° phases at each wavelength across the tuning range of the laser source. Demodulated images are calculated for each of these two spatial frequencies at each illumination wavelength according to $I = (I_0^2 + I_{120}^2 + I_{240}^2)^{1/2}$.[27] Demodulated images are finally converted to diffuse reflectance images by normalizing to a calibrated phantom. Optical absorption and reduced scattering coefficients are estimated at each wavelength from a look-up table generated by Monte-Carlo simulations with diffuse reflectance at 0 mm^{-1} and 0.1 mm^{-1} as inputs.[27] Concentrations are then extracted by fitting absorption values at multiple wavelengths using known basis spectra for each chromophore.[46]

5.2.2 Phantom preparation and imaging

Liquid phantoms were made with varying ratios of water and lipid contents. The lipid content is provided by Intralipid (State Surgical Supply, Siloam Springs, AR, USA) and soybean oil (Sigma-Aldrich, St Louis, MO, USA). The soybean oil is mixed with Triton X-100 (Sigma-Aldrich, St Louis, MO, USA) as an emulsifying agent.[72] Mixtures were blended for 1 min to obtain homogeneous phantoms. Water concentration varied from 90% to 60%, with lipid concentration varying from 10% to 40%. SWIR-SFDI measurements were conducted at wavelengths from 900 – 1,300 nm in 5 nm increments. The measured optical property spectra were smoothed in Fig. 5.2.1a and Fig. 5.2.1b for visualization by a simple moving average (n = 3). The calibration phantom for these measurements was made of 10% Intralipid, whose optical properties were obtained from previous studies.[44,45]

For the depth penetration study (Fig. 5.2.2c), the absorbing tubes and background

liquid phantoms were composed of water, nigrosin (Sigma-Aldrich, St Louis, MO, USA), NIR dye (NIR1054WD, QCR Solutions Corp, Port St. Lucie, FL, USA), and TiO2 (Sigma-Aldrich, St Louis, MO, USA). The absorbing tubes were made with ~10× absorption compared to the background phantom (Fig. 5.2.2d). The absorbing tubes were made from hollow tubes filled with 0.05 g/L nigrosin and 0.055 g/L NIR dye solution. The background phantom was made with 0.061 g/L nigrosin solution with sonicated TiO2. Optical property maps were measured at 680 nm and 1,100 nm, with 0 mm^{-1} and 0.1 mm^{-1}.

5.2.3 Optical absorption of water-lipid phantoms

The absorption of water-lipid phantoms was calculated as the sum of absorption of individual chromophores (water and lipid). The absorption of each chromophore is calculated as chromophore concentration × extinction coefficient spectra, where the concentration is known when making the phantoms, and the chromophore spectra are available in literature. [44,45] The error of optical absorption measurements is determined as a percentage average of the difference between the measured values and the known values.

5.2.4 In vivo water monitoring study for simulated edema

BALB/c mice (Charles River Laboratories, Cambridge, MA, USA) were used in the study in accordance with an institutionally approved protocol and federal guidelines. Hair was removed before the measurements. Simulated edema was induced by subcutaneous injection of 10% phosphate-buffered saline (PBS). An amount of 0 ml, 0.1 ml, and 0.2 ml were used for each group, respectively. There were 4 mice per group.

Baseline measurements were taken before injection, and longitudinal measurements were taken every 5 minutes for a 2-hour duration post-injection. The mice were maintained under anesthesia throughout the experiment. SWIR-SFDI measurements were conducted from 970 – 1,270 nm with 60 nm increments to extract water content. 0 mm^{-1} and 0.1 mm^{-1} spatial frequencies were used in the measurements.

5.2.5 In vivo water monitoring study for acute inflammation

BALB/c mice (Charles River Laboratories, Cambridge, MA, USA) were used in the study in accordance with an institutionally approved protocol and federal guidelines. Hair was removed before the measurements. TPA (12-O-Tetradecanoylphorbol 13-acetate, Sigma-Aldrich, St. Louis, MO, USA) was dissolved in acetone (Sigma-Aldrich, St. Louis, MO, USA) with a concentration of 1 μg/μl. A dosage of 10 μl TPA solution was injected to a group of mice (n=4) to induce acute inflammation. [83,84] The same amount of PBS was injected to the control group (n=4). Baseline measurements were taken before the injection, and longitudinal measurements were taken every 5 minutes for a 2-hour duration post-injection. The mice were maintained under anesthesia throughout the experiment. SWIR-SFDI measurements were conducted from 970 – 1,270 nm with 60 nm increments to extract water content. 0 mm-1 and 0.1 mm-1 spatial frequencies were used in the measurements. The white blood cells counting were conducted with Bright-Line Hemacytometer (Hausser Scientific, Horsham, PA, USA). The preserved tissues were sectioned and H&E stained by the Specialized Histopathology Core of Dana-Farber / Harvard Cancer Center. The stained slides were read by a certified pathologist from the same institution.

5.2.6 Ex vivo mapping of tumor lipid content

The PC3/2G7 prostate tumor xenograft model was used for this study.[70] The PC3/2G7 cells were grown and expanded at 37°C in a humidified 5% CO2 atmosphere in RPMI-1640 culture medium containing 7% fetal bovine serum. 100 Units/ml penicillin and 100 μg/ml streptomycin cells were split in 1:3 or 1:4 when cells reached 70-80% confluence to maintain holoclone-forming ability (approximately one passage every 3 days). Severe combined immunodeficient (SCID) hairless outbred mice (SHO MouseCrl:SHO-PrkdcscidHrhr), age 5 to 6 weeks old (21-23 gram), were purchased from Charles River Laboratories (Cambridge, MA, USA), and housed in the Boston University Laboratory Animal Care Facility in accordance with an institutionally approved protocol and federal guidelines. Autoclaved cages containing food and water were changed once a week. On the day of tumor cell inoculation, 4×10^6 PC3/2G7 cells were subcutaneously injected on the posterior flank of a SCID mouse in 0.2 ml serum-free RPMI using a U-100 insulin syringe with a 28.5-gauge needle. Tumor length (L) and width (W) was measured every 3 days. Tumor volume was calculated as $\text{Vol} = (\pi/6) \times (L \times W)^{3/2}$. After volume exceeded 3000 mm^3, the tumor was rapidly resected and cut in half. The cut face of the tumor was imaged by SWIR-SFDI at wavelengths from 910 nm – 1,290 nm, with 20 nm increments. The edges of the tumor cross-sections were marked with green and yellow permanent inks to help guide later co-registration of microscopic analysis. After imaging, the tissue was snap frozen and sectioned at 10 μm thickness. The sections were stained using Oil Red O with hematoxylin counterstain for lipid content.[85] The stained sections were imaged using a bright-field microscope with ×10 objective (Nikon TE200). Cross-

sections from three tumor samples were measured and stained for lipid content in this study. In the histology slide, the green ink mark was identified and then starting there a rectangular ROI across the tumor sample was imaged by the microscope. The width of the ROI is approximately 1.1 mm. For each tumor sample, the rectangular ROI was separated into 10 sub-areas to calculate individual lipid fractions, and then compared with corresponding areas on the lipid content map measured by SWIR-SFDI. The lipid fraction is defined as number of lipid pixels divided by total number of pixels. The staining of the tissue slides was conducted by the Specialized Histopathology Core of Dana-Farber / Harvard Cancer Center. Images of the stained slides were later read by a certified pathologist from the same institution to confirm identification of lipid pixels.

In order to automatically identify pixels representing lipid in all the microscopic images, over 1,800 pixels were first manually labeled as lipid or non-lipid by visual inspection in those images (the labeling was confirmed by certified pathologist). Then we compared two classification methods: simple thresholding and nearest-neighbor. We randomly separated the labeled data as training set and test set. The training set was composed of 500 lipid pixels and 1,000 non-lipid pixels. The test set was composed of 150 lipid pixels and 150 non-lipid pixels. For the thresholding method, we explored both RGB space and HSV space of the data, and identified that thresholds in the HUE channel could best separate the two classes with 92.6% and 91.1% accuracies for lipid and non-lipid, respectively on the training set. On the test set, the thresholding method had 80% and 93.3% performance for lipid and non-lipid samples, respectively. For the nearest-neighbor method, we first converted each pixel from RGB to HSV, and then combined both spaces

into a 6-channel vector with RGB channels normalized to [0, 1]. The classification was conducted by searching for closest pixel in the training set with Euclidean distance. It achieved 100% accuracy in the training set and 98.0% accuracy for both classes in the test set. For all the microscopic images, we applied the nearest-neighbor classification on each pixel and generated binarized lipid maps where lipid pixels were labeled as 1. The lipid fractions were then calculated from those binarized lipid maps as ratio of the number of lipid pixels with the total number of pixels in the image.

5.2.7 In vivo identification of brown adipose tissue

A total of ten healthy C57BL/6 mice (Charles River Laboratories, Cambridge, MA, USA) were included for brown adipose tissue classification study. Adipose tissues were excised at anatomical locations known to contain brown and white fat.[86] These BAT and other tissue samples were imaged with SWIR-SFDI from 900 nm – 1,300 nm, yielding measurements of optical absorption and reduced scattering with 5 nm spectral increments. From these 81 measured wavelengths, a subset was selected by a feature selection algorithm: 1,145 nm, 1,205 nm, and 1,245 nm.[87] SWIR-SFDI measurements at these three wavelengths were then used to train a support vector machine (SVM) classifier to identify BAT. [88] Only data of pixels from the training set mice (n=7) was used in wavelength selection and training the classifier. The trained SVM was tested on adipose tissue data from another three mice. Under anesthesia, in vivo measurements were conducted for those mice, and the same SVM was used to distinguish BAT from other tissues through skin.[87] Tissues from the prediction area were sampled and preserved for verification of the SVM

classification. The preserved tissues were sectioned and H&E stained by the Specialized Histopathology Core of Dana-Farber / Harvard Cancer Center. The stained slides were read by a certified pathologist from the same institution.

5.2.8 Blood lipids study in humans

This study was conducted in accordance with an institutionally approved protocol and federal guidelines. Ten human subjects were measured with SWIR-SFDI in the morning and afternoon of 5 hours apart the measurements, respectively, at 730 nm – 1250 nm with 40 nm increments and 0 mm^{-1} and 0.1 mm^{-1} spatial frequencies. Blood draws were conducted immediately after each measurement by a professional phlebotomist (Boston Clinical Laboratories, MA, USA), and lipid panel analysis was performed by the same company. The chemical analysis on blood draws was considered gold standard in this study. The total blood lipids content from lipid panel (triglycerides + total cholesterol) was correlated with SWIR-SFDI measured lipid content.

5.3: Results

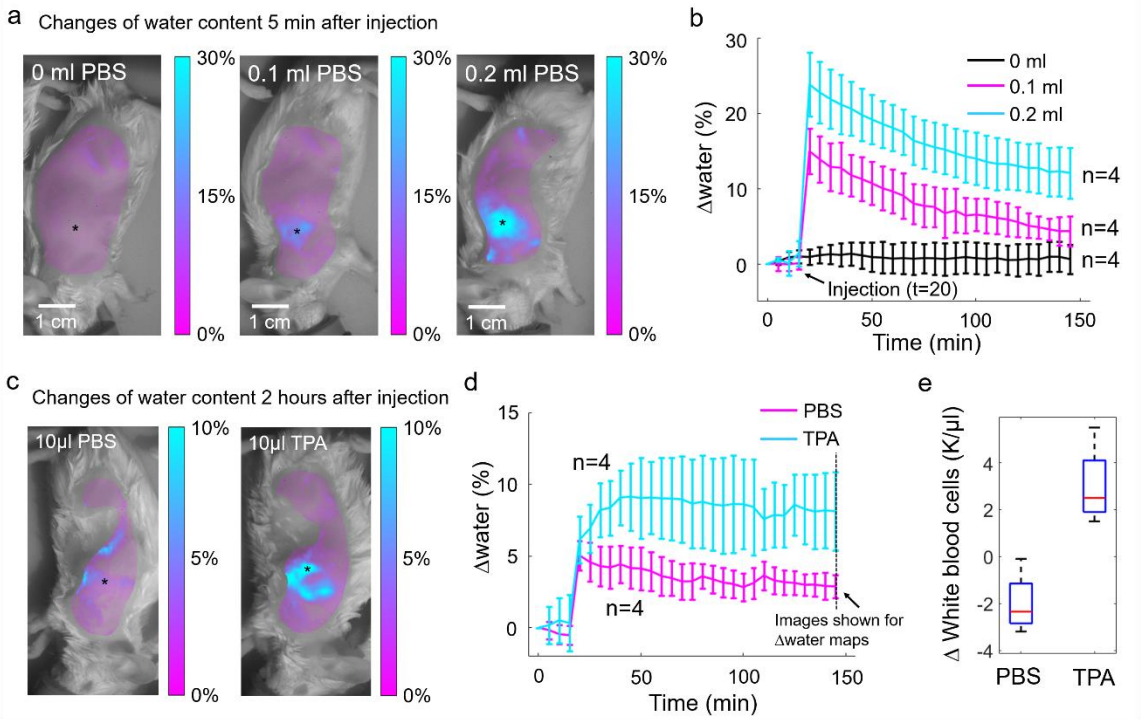

Figure 5.1.2: Non-invasive in-vivo monitoring of water content for simulated edema and acute inflammation. a, Three dosages of PBS were respectively applied to individual groups of mice (n=4). Color-coded water content changes at the injection site are shown on a representative mouse of each group. Star sign represents the location of injection. b, Time series of the mean and standard deviation of the mean values of all four mice in each group. For the 0 ml group, there was no significant water content changes of before and after the injection (p=0.94). For the 0.1 ml and 0.2 ml groups, both had significant water content changes of before and after the injection (p=7.9e-5 and p=6.2e-5, respectively). c, A dosage of 10 µl PBS and TPA were respectively applied to two groups of mice (n=4). Changes of water content are color-coded and shown on a representative mouse of each group. d, Time series of the mean and standard deviation of the mean values of all four mice in each group. For the 10 µl PBS group, the water content gradually decreased after the initial injection. In contrast, for the 10 µl TPA group, the water content continued increasing after injection, indicating accumulation of water content and potential inflammation (later confirmed with histology analysis by certified pathologist). At the end of monitoring the water content of the two groups are significantly different from each other (p=0.0035). e, Blood samples were collected from tail vein for all mice in both PBS and TPA groups, at before the injection and 5 hours after injection. White blood cells (WBCs) as indicator of inflammation were counted and the changes in WBCs were compared. The TPA group shows significant increase in WBCs compared to the PBS control group (p=0.0038).

5.3.1 In vivo water content monitoring

Tissue water content is an important indicator for edema and inflammation.[23] *In vivo* tissue water content was monitored longitudinally over 2 hours in a small animal

model of simulated edema (Fig. 5.1.2a). Different amounts (0 ml, 0.1 ml, and 0.2 ml) of PBS were subcutaneously injected to mice in each group (n=4). Fig. 5.1.2a demonstrates representative mice from each group with changes of water content mapped on fur-free area of the mouse body right after injection. The 0 ml mouse shows no increase of water content, and the 0.1 ml mouse shows a moderate increase. As expected, the 0.2 ml mouse shows the highest increase in terms of measured water content. Fig. 5.1.2b demonstrates time series of the mean and standard deviation of the mean values of changes of water content around injection site for all four mice in each group. The 0 ml group has relatively stable water content over the course of monitoring. The 0.1 ml and 0.2 ml groups both have significant increase of water content caused by the injection, and the water content gradually decreases after the injection.

To further demonstrate water content monitoring for a physiological process, acute inflammation was induced by injection of 10 µl TPA, and the same amount of PBS was used in the control group, as shown in Fig. 5.1.2c. Changes of water content 2 hours after the injection was mapped on body fur-free area for representative mice from both groups. The Δwater map for the PBS mouse shows that 2 hours after the injection, only slight increase of water content can be observed. In contrast, the TPA mouse shows large increase of water content caused by the injection of 10 µl liquid. Fig. 5.1.2d demonstrates the time series of the water content around injection site for the two groups. For the PBS group, the water content gradually decreased towards baseline after the injection. In contrast, for the inflammation (TPA) group, water content continued to increase after the injection, and then stayed relatively stable till the end of monitoring. To verify existence of inflammation in

the TPA group, blood samples were collected from tail vein of all mice in both PBS and TPA groups, at before the injection and 5 hours after injection. White blood cells (WBCs) as indicator of inflammation were counted (Supplementary Table 7) and the changes in WBCs were compared, as shown in Fig. 5.1.2e. The TPA group shows significant increase in WBCs compared to the PBS control group ($p=0.0038$). In addition, after the imaging measurement, tissues from injection site were cut and preserved. The tissue samples were then stained with H&E. The stained tissue slides were rated by certified pathologist. Presence of cellular acute inflammation was found in samples of TPA group, although in some samples the signs of inflammation was minimal, potentially due to the fact that the mice were sacrificed only 5 hours after exposure to TPA. No signs of cellular acute inflammation were found in samples of PBS group.

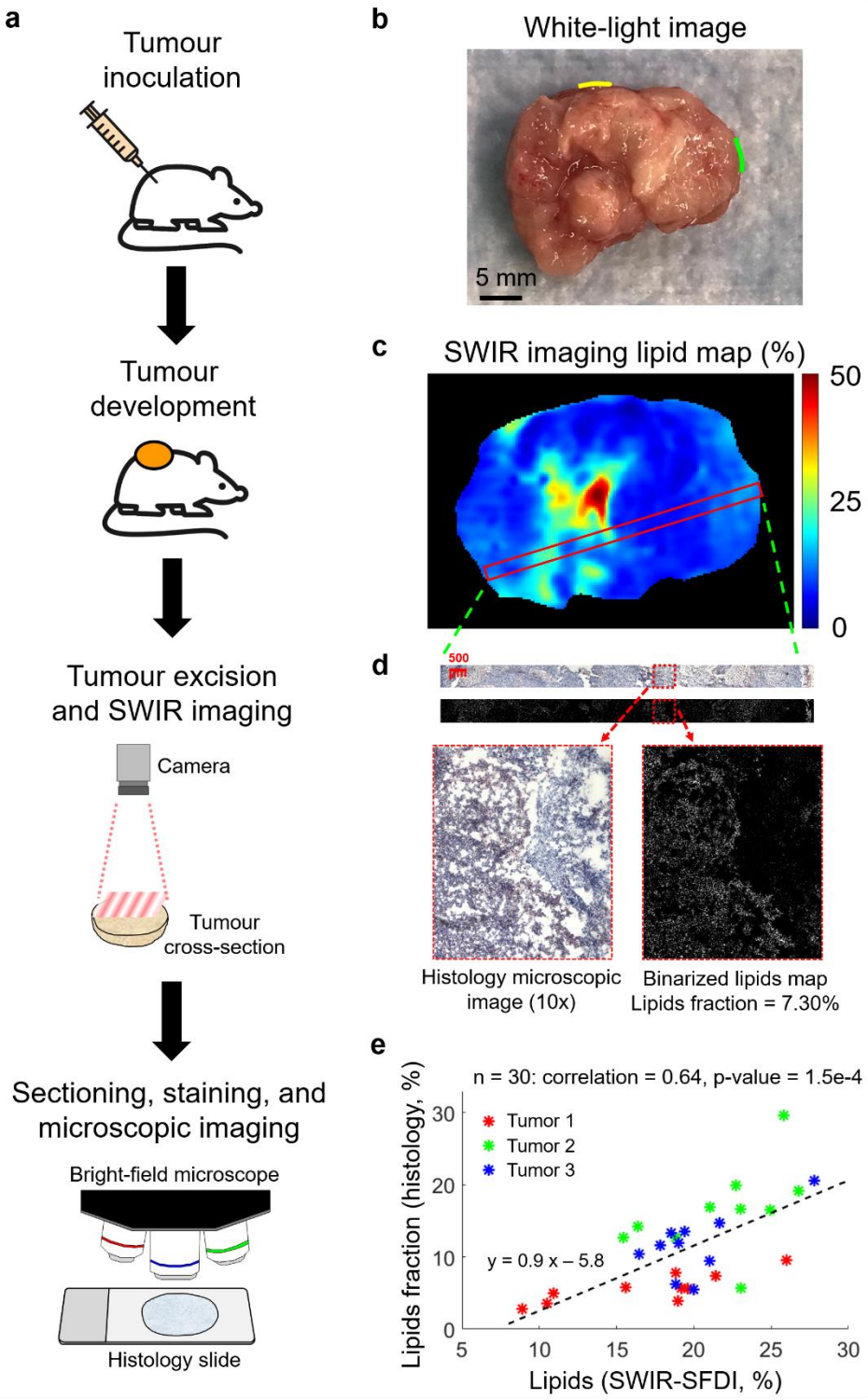

Figure 5.1.3: ***Ex vivo*** **mapping lipid in tumor. a, Tumor cells are inoculated in small animal and the grown tumor is excised and the cross-section of the tumor is imaged with SWIR-SFDI for lipid**

mapping. The tumor samples (n=3) are then sectioned, stained, and imaged under bright-field microscope for lipid fraction analysis. b, White-light image of a representative tumor cross-section. Green and yellow marks are made by permanent inks for co-registration with histology slides. c, Lipid content map measured by SWIR imaging. The red box indicates corresponding area on the histology slide for lipids correlation. Microscopic images are collected from the histology slide area and corresponding binarized lipid maps are generated, as shown in (d). d, The imaged histology slide area is divided into 10 sub-areas and lipids fraction is calculated as the number of lipids pixels over the total number of all pixels, in each sub-area image. e, Correlation plot of SWIR-SFDI results and histology staining. X-axis shows lipid content measured by SWIR-SFDI, and Y-axis shows lipid fraction identified by microscopic images. Black dashed line indicates the best fit line. The Pearson correlation coefficient of the lipid results is 0.64, indicating agreement of histology results with SWIR-SFDI measurements. Colour of data points corresponds to cross-sections from three different tumors.

5.3.2 Ex vivo mapping of tumor lipid content

Phenotypic and functional heterogeneity is known to exist among cancer cells within the same tumor, as a consequence of genetic change, environmental differences and reversible changes in cell properties.[89] The role of intra-tumor heterogeneity in predicting therapeutic response and tumor progression has recently been brought to attention.[90,91] There is a growing recognition that intra-tumor heterogeneity within the same patient is clinically relevant for making treatment decisions.[89] Improved scientific approaches are therefore still needed to probe tumor heterogeneity and further study drug response biomarkers.[89,92]

Figure 5.1.3 demonstrates ex vivo mapping of lipid content in a subcutaneous tumor model using SWIR-SFDI. The study procedures are illustrated in Fig. 5.1.3a. After inoculation and development, the tumor was cut in half and imaged with SWIR-SFDI. Tissue samples were collected for sectioning and lipid staining, and then imaged with bright-field microscopy. While visual heterogeneity can be observed in the white light image (Fig. 5.1.3b), SWIR-SFDI unveils qualitative heterogeneities in biomarker spatial distributions (Fig. 5.1.3c). The lipid composition is derived from binarized lipids map of

the microscopic image, illustrated in Fig. 5.1.3d. Binarized lipids map of other tumor cross-sections are shown in Fig. 5.2.3. Quantitative measurement of tumor lipid content determined by SWIR-SFDI was compared to lipid content in Oil Red O stained tumor sections. Rectangular regions of interest (ROIs) across the cut face of the bisected specimens were analyzed for 3 tumor samples, and correlated with SWIR-SFDI results (Fig. 5.1.3e). These corresponding ROIs in the SWIR-SFDI lipid concentration map exhibited strong correlation with levels of lipid composition identified by microscopic staining.

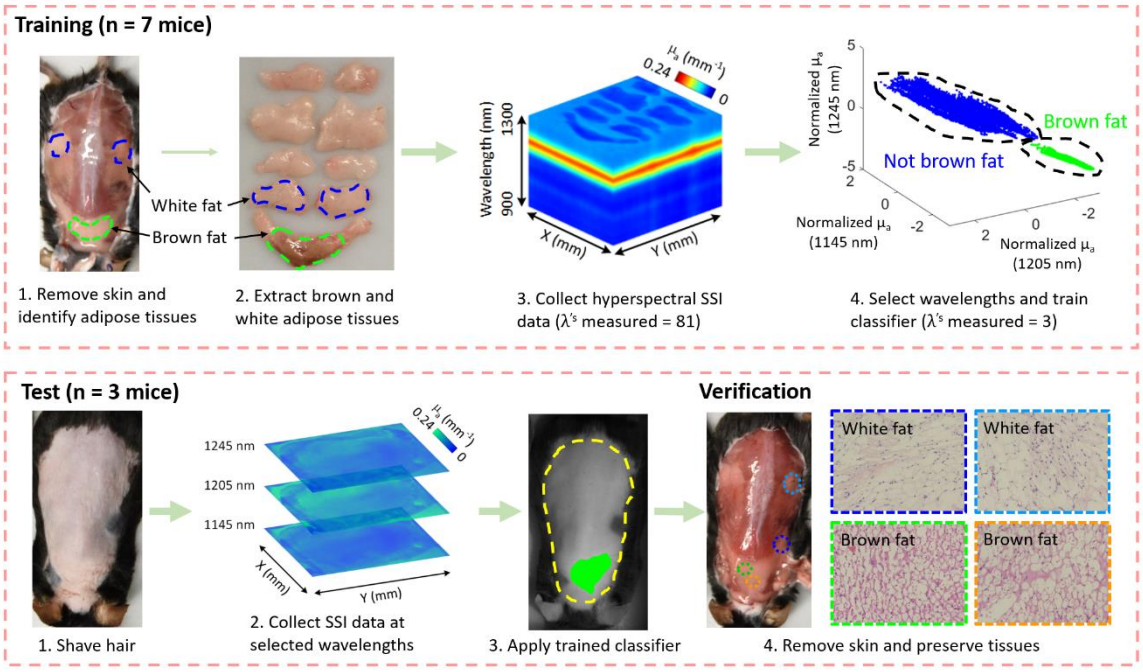

Figure 5.1.4. *In vivo* classification of brown adipose tissue. A machine learning framework is designed, implemented, and verified for identifying in vivo brown fat within intact skin. In the training phase (n=7), mouse skin is removed and brown adipose tissue as well as other tissues are extracted. Hyperspectral (900 – 1,300 nm) SWIR-SFDI data is collected for the ex vivo tissues. With a wavelength feature selection algorithm, three wavelengths are selected to train an SVM classifier for identifying brown adipose tissue. In the test phase (n=3), SWIR-SFDI data is collected at selected wavelengths with the mouse hair shaved and the skin being intact. Within the region-of-interest (ROI) indicated by the yellow dashed line, the SVM classifier is used to map subcutaneous BAT on a per-pixel basis (green overlay) non-invasively in vivo. For verification, the mouse skin was removed after SWIR-SFDI imaging, and tissue samples were collected from predicted brown fat and other tissue type areas. The

predicted brown fat and other tissues were stained with H&E, and imaged under bright-field microscope. The data shows that the SVM prediction matches the histology results (confirmed by a certified pathologist).

5.3.3 In vivo identification of brown adipose tissue

Brown and white adipose tissue (BAT and WAT, respectively) are the two major types of adipose tissue. BAT is well-known for its role in thermoregulation and anti-obesity,[93,94] while WAT is primarily responsible for storage of energy and providing thermal insulation.[86] Being present in most adults,[95] BAT has also been found to contribute to longevity.[96] WAT is predominantly found in the subcutaneous and visceral areas of the body, while BAT is located primarily at the interscapular area and in the large blood vessels of the thorax.[86] On the cellular level, brown adipocytes may appear and develop in WAT in response to thermogenic stimuli in a process termed the "browning" of WAT.[97,98]

Here we demonstrate the use of SWIR-SFDI for non-invasive *in vivo* differentiation of brown adipose tissue from other types of tissues such as white adipose tissue. First, hyperspectral SWIR-SFDI data from seven C57BL/6 mice were used to select a subset of wavelengths where the measured absorption coefficients exhibit the potential to discriminate between BAT and other tissue types.[87] The top three performing wavelengths (1145 nm, 1205 nm, and 1245 nm) were applied to data from another three mice, demonstrating feasibility of separating BAT and other tissues by their spectral features (Fig. 5.1.4 upper panel). A support-vector-machine (SVM) was trained to distinguish BAT,[88] achieving over 87% accuracy on out-of-sample test data. The trained SVM classifier was applied to each pixel within a defined region of interest in a dataset acquired in separate mice in vivo. The identified BAT region on a representative mouse (Fig. 5.1.4

lower panel, subfigure 3) agrees well with the anatomical distribution of BAT in mice.[86] For verification, the mouse skin was removed after imaging, and tissue samples were collected from predicted brown fat and other tissue type areas. The predicted brown fat and other tissues were stained with H&E. The stained slides were imaged with bright-field microscope and the prediction results were confirmed by certified pathologist. Verifications on other mice in the test set are included in Fig. 5.2.4.

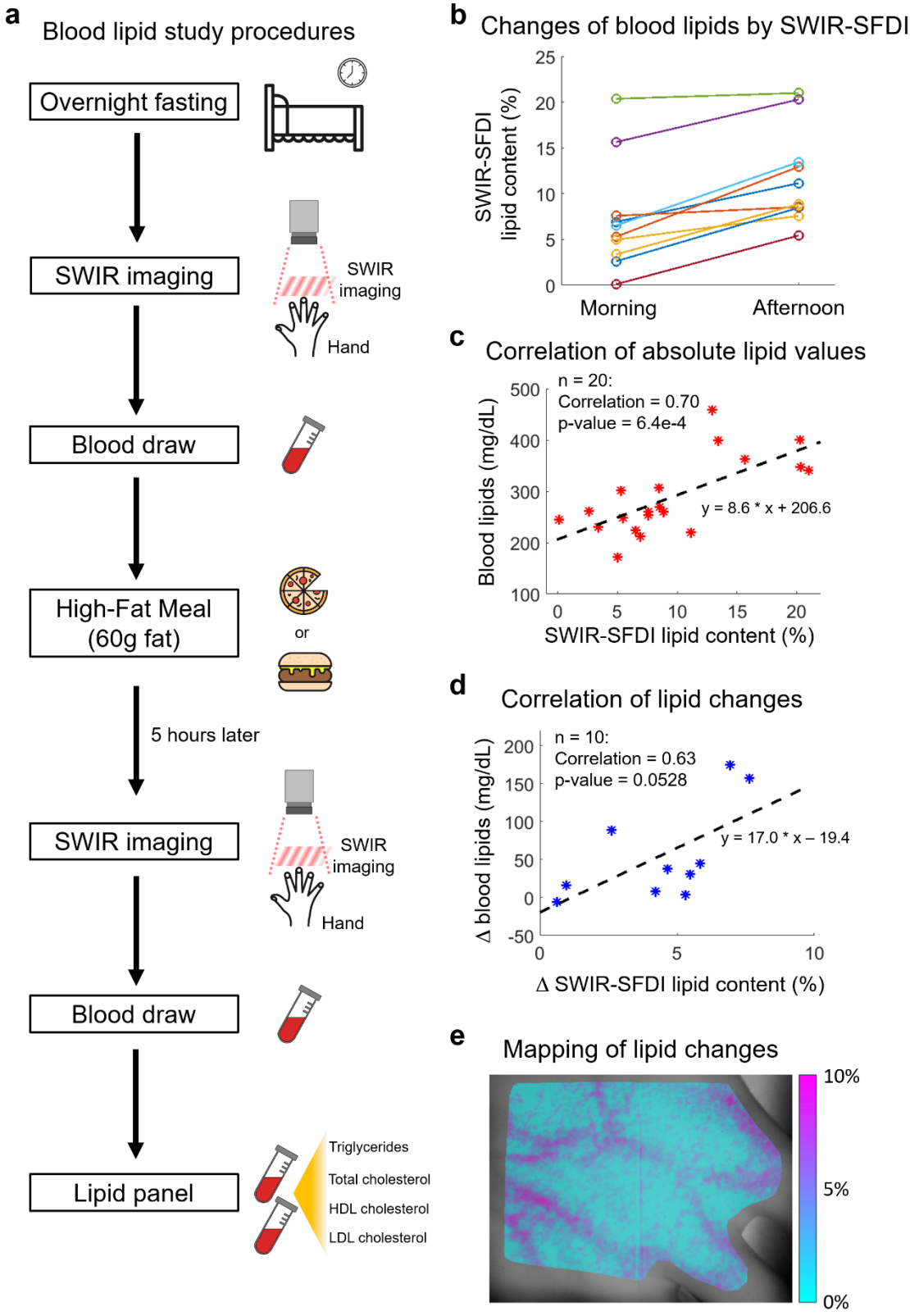
a
Blood lipid study procedures
Overnight fasting
SWIR imaging
SWIR imaging
Hand
Blood draw
High-Fat Meal (60g fat)
or
5 hours later
SWIR imaging
SWIR imaging
Hand
Blood draw
Lipid panel
Triglycerides
Total cholesterol
HDL cholesterol
LDL cholesterol
b
Changes of blood lipids by SWIR-SFDI
SWIR-SFDI lipid content (%)
Morning
Afternoon
c
Correlation of absolute lipid values
n = 20:
Correlation = 0.70
p-value = 6.4e-4
y = 8.6 * x + 206.6
Blood lipids (mg/dL)
SWIR-SFDI lipid content (%)
d
Correlation of lipid changes
n = 10:
Correlation = 0.63
p-value = 0.0528
y = 17.0 * x – 19.4
Δ blood lipids (mg/dL)
Δ SWIR-SFDI lipid content (%)
e
Mapping of lipid changes
10%
5%
0%

Figure 5.1.5. Blood lipids measurement on human subjects. a, Blood lipid study protocol. After 10 hours overnight fasting, the subjects are measured with SSI in the morning, immediately followed by a blood draw. A high-fat meal is then provided to the subjects as breakfast. Five hours later, another measurement and blood draw are conducted. Blood lipids (triglycerides and cholesterol) content obtained from the blood draws are considered gold standard in this study. b, Correlation of absolute blood lipid values between SSI measurements and blood draws. With 20 data points being measured from both modalities, the correlation coefficient is 0.70, indicating a strong correlation and agreement of SWIR-SFDI measurements with the gold standard. c, Correlation of the changes in blood lipids content between SWIR-SFDI measurements and blood draws. With 10 subjects being measured from both modalities and at two time points, the correlation coefficient is 0.63, which shows strong agreement between the SWIR-SFDI measurements and the gold standard. d, A map of changes in lipid content on the subject's hand. Structural features of hand vessels are clearly visible in the Δlipid map, indicating a higher increase of lipid content in the veins compared to non-vascular tissues.

5.3.4 Non-invasive blood lipids monitoring in humans

Blood lipids level is known to correlate with cardiovascular disease.[99] Currently in order to determine blood lipid levels, invasive methods such as blood draws are required in the clinics. To demonstrate SWIR-SFDI for non-invasive measurement of blood lipids, we measured the hand of human subjects, and compared the results from blood draws (with lipid panel). Furthermore, while high-fat diets are known to cause increase in blood lipids,[100] we longitudinally measured those healthy volunteers before and after a high-fat meal, and compared with blood draws. Fig. 5.1.5a demonstrates the blood lipid study procedures. Blood lipids were measured twice for each subject, respectively in the morning before the high-fat meal, and 5 hours later in the afternoon. The measured lipid content levels at both time points are shown in Fig. 5.1.5b. Obvious increase in blood lipid content were observed by SWIR-SFDI, which matches the lipid panel results from blood draws (Table 8). In addition, the total blood lipids from blood test and SWIR-SFDI measured lipid content are compared in Fig. 5.1.5c, with a strong correlation of 0.70 (n=20). In addition, the measured changes of blood lipids from SWIR-SFDI and the blood test are

also compared in Fig. 5.1.5d, with a strong correlation of 0.63 (n=10). Moreover, a lipid subtraction map from a representative subject is derived by subtracting reconstructed lipid concentration map of 5 hours after meal, from the lipid concentration map of the baseline (before meal). Areas of blood veins are clearly visible, and it highlights the increase of lipid content in the veins, as shown in Fig. 5.1.5e.

5.4: Discussion

We have shown for the first time in vivo simultaneous mapping of water and lipid with a SWIR-SFDI system. Building such a system brought challenges in instrumentation, such as light source, structured illumination, and camera. The light source needs to be tunable and have hyperspectral capability. The illumination component needs to be able to project flexible structured patterns, from VIS-NIR to SWIR regions. The camera should be sensitive to a broad wavelength range, breaking the sensitivity limitation of regular silicon detectors. To overcome those difficulties, we used a tunable pulsed laser and a Germanium camera to project and collect structured light patterns from VIS-NIR to SWIR region (up to 1,300 nm).

The system was first validated with a phantom study and demonstrated for increased penetration depth in the SWIR region. We also demonstrated *in vivo* water content monitoring as a potential application for studying inflammation and edema. It has been shown in previous study that water and lipid are important biomarkers for tumor.[2,3,23] We then measured an *ex vivo* tumor for those biomarkers, with validation by microscopic staining images. While chromophore concentrations can be calculated by fitting optical

absorption, this is better done at wavelengths where individual chromophores have high absorbance and not obscured by other chromophores.[46] As described in previous literature, notable shortwave infrared absorption features of tissue constituents including water, lipids, and collagen are much more prominent than their counterparts in visible and NIR.[44,45,47] Therefore, SWIR wavelengths are essential for accurate extraction of biomarkers, such as water and lipid in the tumor.

With importance to body thermoregulation and metabolism, we demonstrated *in vivo* distinguishing of brown adipose tissue with intact skin on a small animal model. Such capability has important application potentials. Accumulation of excess WAT has deleterious consequences for metabolic health.[94] The development of beige adipocytes in WAT (browning) would raise energy expenditure and reduce adiposity.[101] Thus, being able to detect BAT over WAT and other tissues opens the potential of longitudinal monitoring of 'browning' which is related to the reduce of adverse effects of WAT and could help to improve metabolic health.[94]

Finally, we demonstrated *in vivo* probing of blood lipids in humans, with importance to cardiovascular risk monitoring. In addition, for patients with high concentration of lipids in the blood, lipid-lowering therapy with statins is widely used in the clinics to reduce the risk of cardiovascular events as well as overall mortality in primary and secondary preventions.[102,103] However, with a lack of convenient blood lipids monitoring, it has been shown that overtreatment and undertreatment for hyperlipidemia are frequent in clinical practice.[103] Therefore, the demonstrated system can potentially be applied in lipid-lowering treatment for optimal dosage and improved treatment outcome.

There are other potential applications of the SWIR-SFDI system, such as surgical guidance, tumor biology, and surgeries (skin flaps).[34,75,104]

5.2: Supplementary Materials

The work in part 5.2 is to be submitted as supplementary document for part 5.1 with the following contributing authors:

Yanyu Zhao,[1] Matthew Applegate,[1] John Jiang,[1] John Paul Dumas,[2] Mark Pierce,[2] and Darren Roblyer [1]

[1] *Boston University, Department of Biomedical Engineering, 44 Cummington Mall, Boston, Massachusetts 02215, United States*

[2] *Rutgers, The State University of New Jersey University, Department of Biomedical Engineering, 599 Taylor Road, Piscataway, New Jersey 08854, United States*

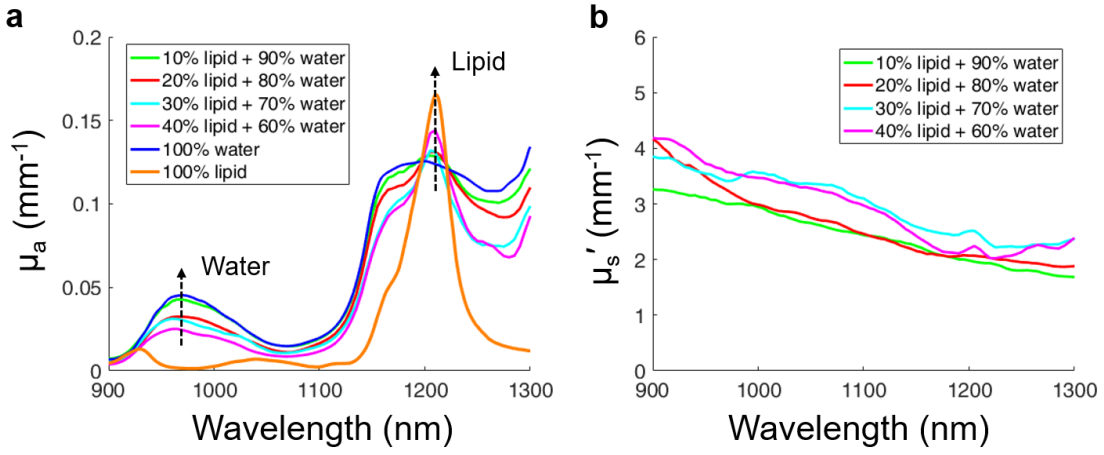

Figure 5.2.1. a, Measured optical absorption (μ_a) spectra of water-lipid phantoms. Absorption spectra of 100% water and 100% lipid are also plotted in (a) for reference. At the water absorption peak of 970 nm, the measured optical absorption increases with elevated water concentration in the phantoms, and at the lipid peak of 1,210 nm, the measured absorption also increases with lipid concentration. b, Measured optical scattering (μ_s') spectra of the phantoms. It can be observed that the measured optical scatterings were similar between phantoms.

Known concentration		Extracted concentration		Error	
Water	Lipid	Water	Lipid	Water	Lipid
90.0%	10.0%	92.2%	9.1%	2.2%	0.9%
80.0%	20.0%	81.3%	19.0%	1.3%	1.0%
70.0%	30.0%	66.5%	28.4%	3.5%	1.6%
60.0%	40.0%	59.4%	41.0%	0.6%	1.0%

Table 5. Extracted water and lipid content from water-lipid phantoms. Water and lipid concentrations are extracted from SWIR-SFDI measurements by fitting the optical absorption spectra, then the extracted concentrations are compared with known concentrations. The average error for water is 1.9%, and the average error for lipid is 1.1%.

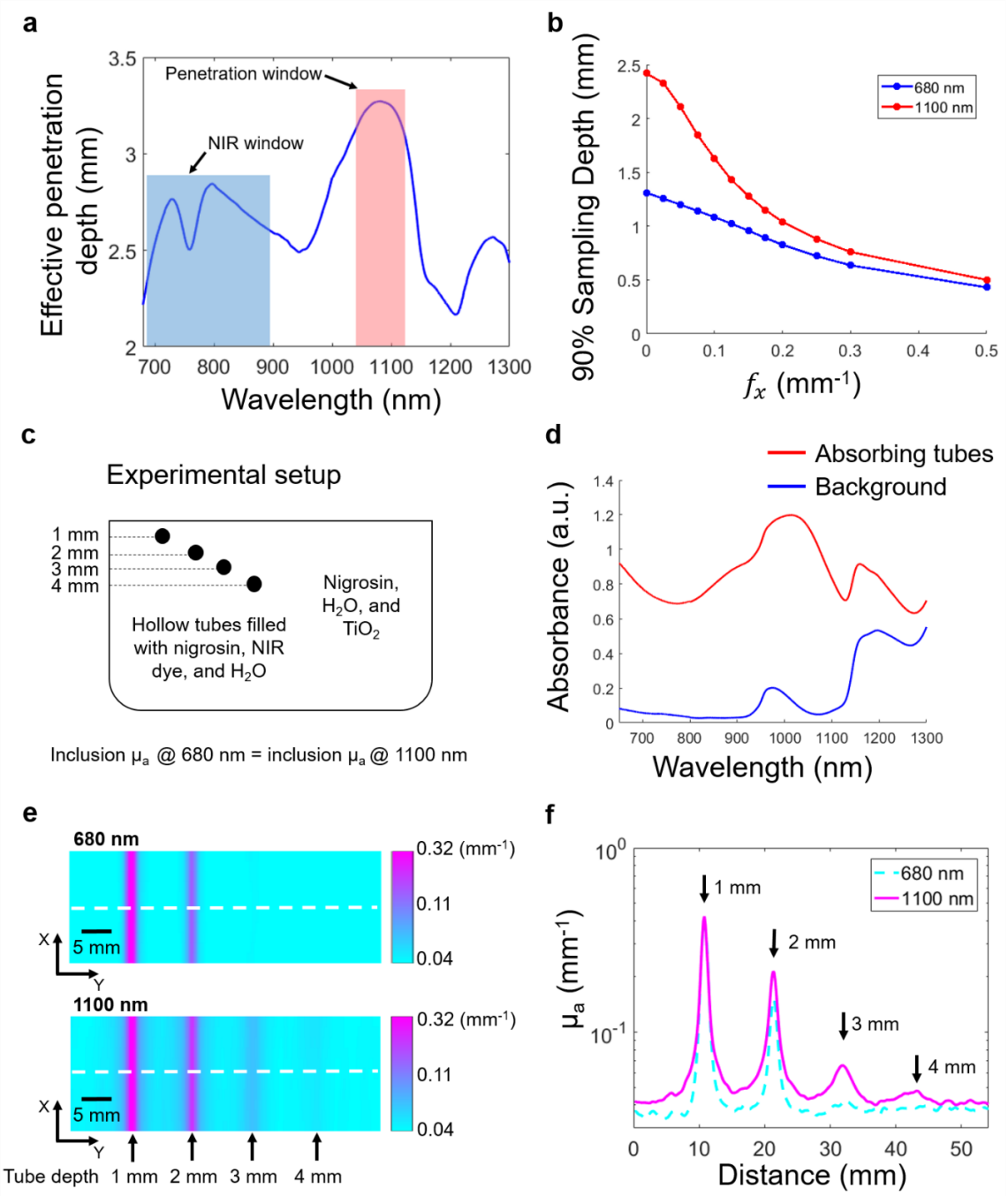

Figure 5.2.2. Increased penetration depth with SWIR wavelengths. a, SWIR penetration window near 1,100 nm is identified by calculating SFDI effective penetration depth using mouse data. [78] It shows that SWIR wavelengths can significantly improve penetration depth compared to the NIR window. b, Improved penetration depth at SWIR window verified by Monte Carlo simulations. Depth statistics for both wavelengths and spatial frequencies are presented as 90% photon visitation depths. The depth statistics show 1.31 mm probing depth at DC for 680 nm and 2.42 mm depth for 1,100 nm, respectively. c, Measurement setup of the experiment (side view). Four absorbing tubes were place underneath the

background liquid phantom, at 1 mm – 4 mm depths. d, Calculated absorbance spectra of absorbing tubes (red line) and background liquid phantom (blue line), respectively. The absorbance spectra were calculated based on spectrophotometer measurements of nigrosin, water, and NIR dye. e, Optical absorption maps measured at 680 nm and 1,100 nm wavelengths. f, Line profiles of measured optical absorption corresponding to the dashed white lines in (e).

SBR	1 mm	2 mm	3 mm	4 mm
680 nm	9.4	3.8	1.1	1.0
1100 nm	10.0	5.1	1.6	1.2
Improvement	6.4%	34.2%	45.5%	20%

Table 6. Quantitative comparison of signal-to-background ratio at 680 nm and 1,100 nm.

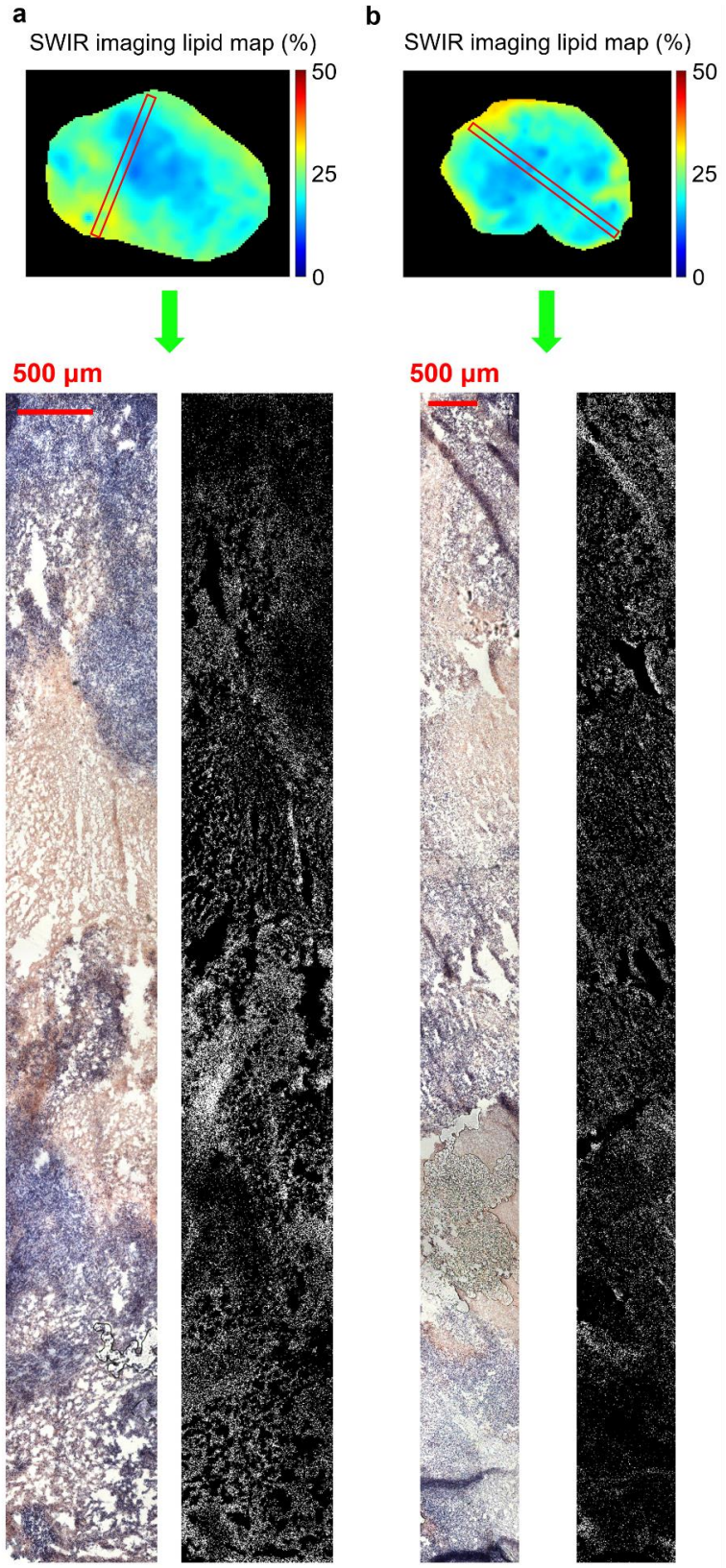
a
SWIR imaging lipid map (%)
50
25
0
500 µm
b
SWIR imaging lipid map (%)
50
25
0
500 µm

Figure 5.2.3. Tumor cross-section lipid maps from SWRI-SFDI and histology microscopic images. a, SWIR imaging lipid map of tumor #2 of Fig. 5.1.3d. Histology image and corresponding binarized lipid map are shown for the red rectangular ROI. b, SWIR imaging lipid map of tumor #3 of Fig. 5.1.3d. Histology image and corresponding binarized lipid map are shown for the red rectangular ROI.

Mice	PBS				TPA			
	#1	#2	#3	#4	#1	#2	#3	#4
Before	13,200	13,700	14,400	9,800	12,500	11,800	9,800	12,200
After	11,000	11,200	11,200	9,700	18,000	13,300	12,500	14,500

Table 7. White blood cells counting before and 5 hours after injection.

Subjects	**Triglycerides (mg/dL)**		**Total cholesterol (mg/dL)**		**HDL cholesterol (mg/dL)**		**LDL cholesterol (mg/dL)**	
	Morning	Afternoon	Morning	Afternoon	Morning	Afternoon	Morning	Afternoon
#01	52	61	160	159	61	60	81	77
#02	135	290	167	169	46	42	89	88
#03	61	142	111	119	60	60	35	36
#04	136	182	227	219	46	49	126	126
#05	163	159	184	182	63	62	96	91
#06	80	253	144	146	62	55	46	44
#07	46	56	199	193	64	62	125	118
#08	92	141	170	166	62	57	89	84
#09	64	82	190	188	49	47	119	118
#10	76	105	154	156	52	54	83	82

Table 8. Lipid panel from blood draws for all human subjects.

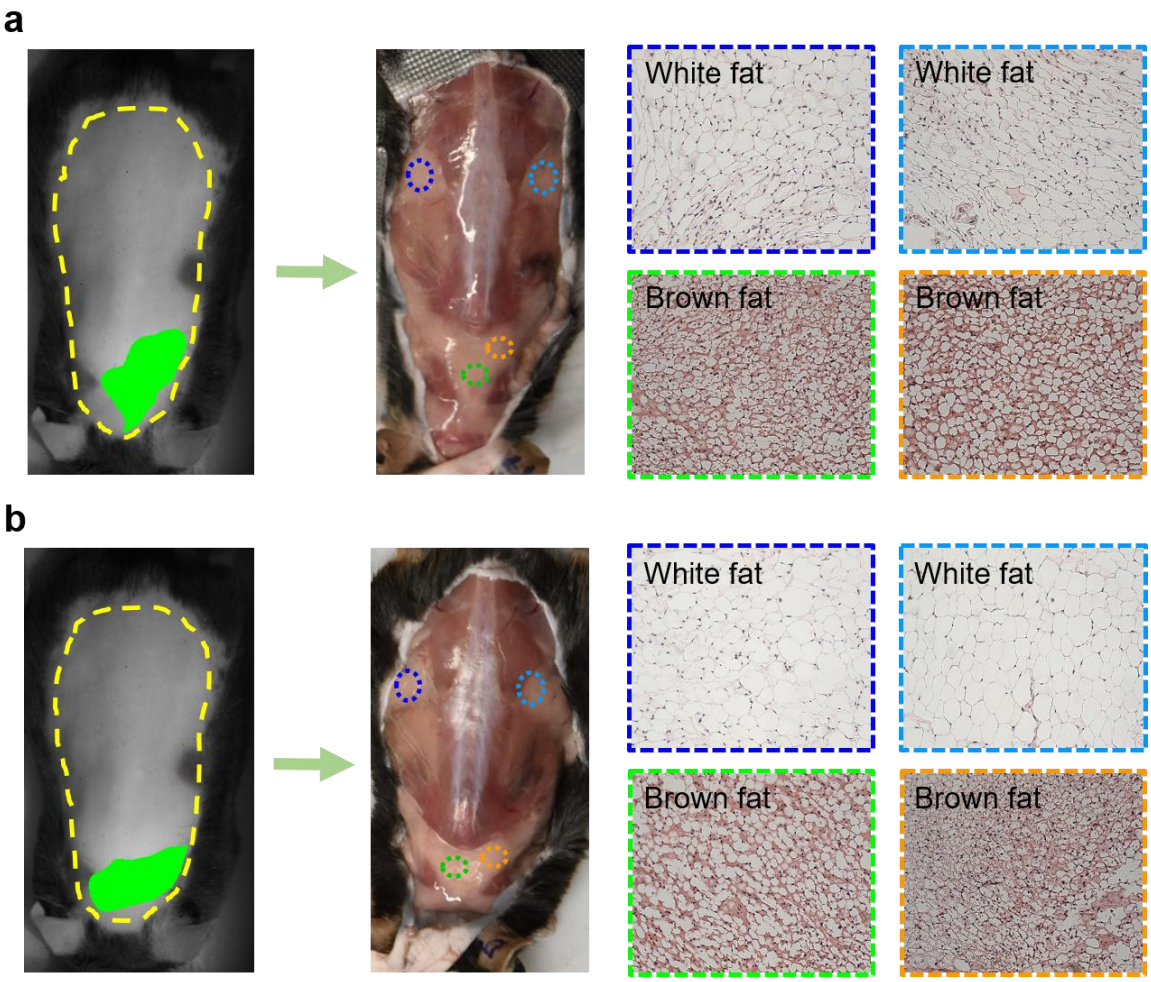

Figure 5.2.4. Classification and verification of in vivo brown fat identification. a, The trained SVM is applied on out-of-sample mouse for brown fat identification. The predictions are verified with H&E of tissue samples. b, The trained SVM is applied on another mouse for brown fat identification. H&E stained tissue samples are used for verification of predictions.

CHAPTER SIX: DEEP LEARNING INVERSE MODEL FOR SPATIAL FREQUENCY DOMAIN IMAGING (SFDI)

Spatial frequency domain imaging (SFDI) becomes increasingly popular as it is able to provide quantitative and wide-field tissue optical properties, as well as and chromophore concentrations. SFDI conducted with 2 spatial frequencies (2-fx) has been widely used in pre-clinical and clinical studies. It has been known that with multiple frequencies (multi-fx) the estimation of optical properties can be more accurate with reduced uncertainty. However, performing SFDI with multi-fx is limited in practice, with the major bottleneck being the speed of inversion from measured diffuse reflectance (R_d) to optical properties. We present a deep learning solution that solves the inverse problem in a fast and accurate manner. Particularly, we present the deep learning model with similar or improved optical property inversion accuracy than previous methods. We also demonstrate that the proposed method is ×300 – ×100,000 faster than the other methods. Combined with real-time data acquisition techniques, the proposed deep learning inverse model may enable immediate hemodynamic information and surgical guidance in the clinic.

The work in Chapter Six is to be submitted to a scientific journal with the following contributing authors:

Yanyu Zhao,[1] Yue Deng,[2] Feng Bao,[3] and Darren Roblyer [1]

[1] *Boston University, Department of Biomedical Engineering, 44 Cummington Mall, Boston, Massachusetts 02215, United States*

[2] *Samsung Research, 665 Clyde Avenue, Mountain View, CA 94043, Mountain View, California 94043, United States*

[3] *Tsinghua University, Department of Automation, Beijing, 100084, China*

6.1: Introduction

Tissue optical properties including absorption (μ_a) and reduced scattering (μ_s') can provide important information about tissue oxygenation and molecular composition.[31,46,105,106] Being able to map such information is useful in both pre-clinical and clinical scenarios.[31,32,63,75] Spatial Frequency Domain Imaging (SFDI) is an emerging technology that allows quantitative measurements of tissue optical properties (OPs).[26,27] It has been widely used in a number of biomedical applications, such as small animal imaging, burn wound monitoring, clinical tissue flap monitoring.[30,39,42,43,63,75,107]

In order to separate absorption from scattering, SFDI requires a minimum of 2 spatial frequencies (2-fx) for the inversion from diffuse reflectance (R_d) to optical properties (OPs). In this process, the tissue spatial-frequency-dependent response is calibrated against a phantom with known optical properties to determine tissue R_d values at corresponding spatial frequencies, which is then used to extract optical properties. In the case of 2-fx, R_d will be a 2-d vector, and optical properties can be extracted by interpolating R_d with a Look-Up-Table (LUT) generated by Monte Carlo simulations.[27,28] While SFDI data collection can be relatively fast (up to tens of milliseconds), this inversion process from R_d to OPs is relatively slow, especially when more than 2 spatial frequencies are used.

Angelo *et al.* reported a fast inversion method for SFDI, which could speed up the inversion significantly.[108] With this method, a LUT is pre-computed with a Monte Carlo

forward model. The measured R_d is then compared to each sample in the new LUT, and OPs of the closest sample is assigned as the estimated OPs of the measured tissue. While being fast, the accuracy of the method depends on the density of the pre-computed LUT. If densely sampled, the computational speed will be compromised. In addition, this method was only for the case of 2-fx.

While using 2-fx in SFDI can separate absorption from scattering, it may cause uncertainty problems in the extracted OPs.[109] For 2-fx, although spatial frequency combination, such as [0, 0.1] mm^{-1}, may be optimized to reduce the estimation uncertainty, this is limited to a relatively small range of optical properties.[75] In contrast, the strategy to use a combination of multiple spatial frequencies, such as [0, 0.05, 0.1, 0.2, 0.4] mm^{-1}, in the inversion of OPs can help minimizing the error as well as the impact of uncertainties of diffuse reflectance measurement. [110] Moreover, the use of above spatial frequencies (5-fx), can significantly reduce uncertainties in the extracted optical properties in some OP ranges of the tissue, as shown in Fig. 6.1.1.[109] The upper panel shows estimation uncertainties of μ_a and μ_s', respectively, when SFDI is conducted with only 2-fx. Each point in the plot represents a combination of optical properties. The colored stars in the plots represent literature optical property values of different biological tissues.[46,111–117] The lower panel is the counterpart of the upper panel, showing estimation uncertainties when SFDI is conducted with 5-fx ([0, 0.05, 0.1, 0.2, 0.4] mm^{-1}). The uncertainty plots show that for some tissue optical properties, measurement uncertainty can be over 15% with 2-fx. In contrast, with more spatial frequencies, such uncertainties can be significantly reduced.

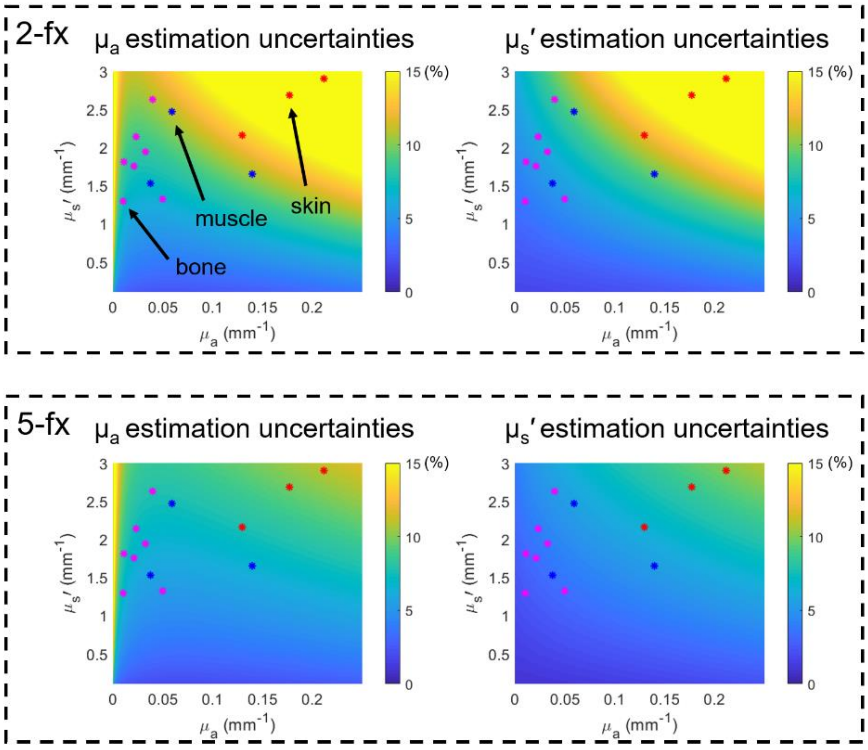

Figure 6.1.1. Estimation uncertainties of extracted optical properties for 2-fx and 5-fx, respectively.[109]

Therefore, compared to 2-fx, the use of 5-fx in SFDI is beneficial in that it can improve estimation uncertainty of OPs for a number of biological tissues and in a larger range of optical properties. However, this does not come for free. While data collection of SFDI can be relatively fast for both 2-fx and 5-fx, it is important to note that different than the 2-fx, the inversion from R_d to OPs with multiple spatial frequencies, such as the 5-fx, is an iterative process, which can be time consuming. Although the method proposed by Angelo *et al.* could potentially be expanded to multi-fx, the accuracy as well as speed will still both be limited by the density of the pre-computed LUT.

Deep learning is a computational technique that has been successfully applied in numerous real world tasks, such as image recognition, speech recognition and translation,

medical image analysis, board games, video games, and many others.[118–123] The power of deep learning lies partially in its ability to automatically detect and approximate nonlinear patterns in the high dimensional space with proper optimization algorithms, as well as training samples and corresponding labels.[118] For example, in the detection of diabetic retinopathy in retinal fundus photographs, training samples are the retinal fundus images, and the corresponding labels are disease grading generated by ophthalmologists.[121] The deep learning model will then learn a high-dimensional mapping from training samples to their labels. Note that such ability is ideal for the sake of multi-fx SFDI inversion. Therefore, in this paper we propose a deep neural network (DNN) inverse model for multi-fx SFDI, which can estimate μ_a and μ_s' simultaneously. The DNN method was tested on a large range of OPs, and compared with existing multi-fx iterative method. We also expanded the fast inversion method by Angelo *et al.* from 2-fx to 5-fx (referred as nearest-search), and then compare with the proposed method. Experimental results show that DNN yields comparable or better accuracy than iterative method, and improves computational speed by multiple orders of magnitude.

6.2: Methods

6.2.1: Spatial frequency domain imaging (SFDI)

The details of SFDI image acquisition and data processing have been describe in detail elsewhere.[27] Briefly, SFDI instrument projects spatially modulated sinusoidal light patterns onto the tissue, and at the same time raw reflectance images are captured by the camera, as shown in Fig. 6.2.1a. Fig. 6.2.1b illustrates the dataflow of SFDI optical

property extraction. After collected by the camera, the raw reflectance images at different spatial frequencies are demodulated and calibrated with a phantom of known optical properties, to get diffuse reflectance at each spatial frequency, denoted as R_d. The R_d at each pixel then serves as input to the inverse model, which provides extraction of optical absorption and reduced scattering values at corresponding pixels. The inversion from R_d to OPs can be based on a Monte Carlo model (refer as "MC") or a diffusion equation model (refer as "diff"). Note that the raw reflectance of the tissue is captured as images, therefore relatively fast. In contrast, the inverse model is applied pixel-by-pixel in the R_d images, which is therefore the bottleneck of speed in the dataflow of optical property extraction.

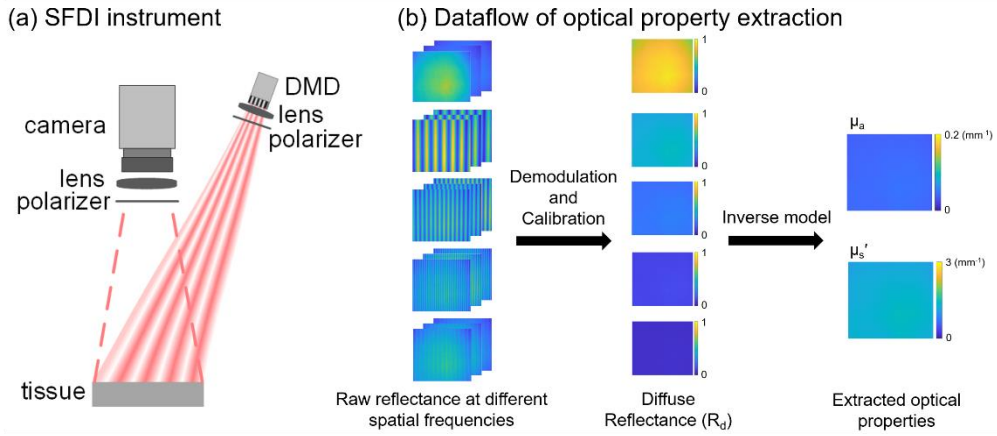

Figure 6.2.1. Diagram of SFDI instrument and illustration of SFDI dataflow for optical property extraction.

6.2.2: Inverse methods

Existing inverse method for multi-fx SFDI operates in an iterative manner, as shown in Fig. 6.2.2a. First, initial guess on OPs is made, and the corresponding theoretical Rd is generated by a forward model, which can be either MC or diff, as discussed in previous sections. The generated R_d is compared with the measured R_d where the difference

is minimized by the iterative algorithm. The OPs will be updated to generate new R_d values to further reduce the difference until convergence is reached for the minimization. Finally, the corresponding OPs from the R_d of convergence will be the output of the iterative process and considered as the OPs of the measured tissue. In previous literature this method has been implemented with the "fminsearch" function in Matlab (MathWorks Inc, Natick, MA, USA).[27]

In addition, we adopted the inverse method originally proposed for 2-fx by Angelo *et al.*, and expanded it to multi-fx, as shown in Fig. 6.2.2b. First, possible combinations of OPs are sampled and sent to the forward model to generate a corresponding R_d set. The measured R_d is compared to each R_d vector in the pre-computed R_d set under Euclidean distance. The corresponding OPs of the closest R_d vector will be determined as the extracted optical properties. This method is also implemented in Matlab and the pair-wise Euclidean distance is calculated using the "pdist2" function in Matlab.

In contrast to the above two methods, the proposed deep learning inverse model (DNN) takes the measured R_d as input, and directly output OPs.

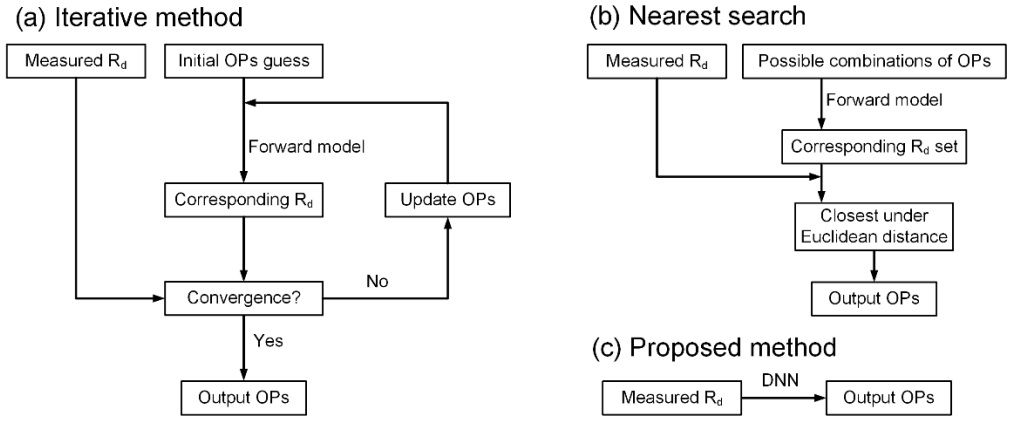

Figure 6.2.2. Comparison of inverse methods for the inversion from measured R_d to optical properties (OPs).

6.2.3: Deep neural network inverse model

The structure of the proposed DNN model is shown in Fig. 6.2.3a. The input of the model is the R_d values at different spatial frequencies. Here we demonstrate the case of 5-fx discussed in section 6.1 and previous literature.[110] The model has 6 fully-connected hidden layers and there are 10 neurons in each layer. The activation function is a hyperbolic tangent sigmoid transfer function, which is nonlinear and maps data from $(-\infty, +\infty)$ to (-1, 1). The model outputs both μa and μ_s' simultaneously.

The training data was generated by the "white" Monte Carlo model, with μ_a sampled from 0.001 mm^{-1} to 0.25 mm^{-1} using 0.001 mm^{-1} increments, and μ_s' sampled from 0.01 mm^{-1} to 3 mm^{-1} using 0.01 mm^{-1} increments.[28] The spatial frequencies were [0, 0.05, 0.1, 0.2, 0.4] mm^{-1}, as discussed in above sections. The training of the deep learning model used Matlab neural network toolbox as well as TensorFlow with Keras as high-level API. Hyperparameters such as number of layers and number of neurons were tuned in Keras using Adam optimization with an initial learning rate of 0.001 and batch size of 128. To reduce potential overfitting, Levenberg-Marquardt optimization with Bayesian regularization was used in the Matlab neural network toolbox. The training was completed after 2000 epochs. Finally, the trained model was implemented in Matlab in order for speed comparison. After training of the DNN model, a number of 10,000 combinations of OPs were randomly selected in the range of [0, 0.25] mm^{-1} for μ_a and [0, 3] mm^{-1} for μ_s', and corresponding 5-fx R_d values were generated by the MC forward model for the test of the trained model. The expected OPs and estimated OPs are demonstrated in Fig. 6.2.3b. The blue dots are the randomly generated OP points. The red lines are the linear fit from the

blue dots. Fig. 6.2.3b shows that the outputs of the DNN match closely with expected ground truth values, indicating no signs of overfitting of the neural network.

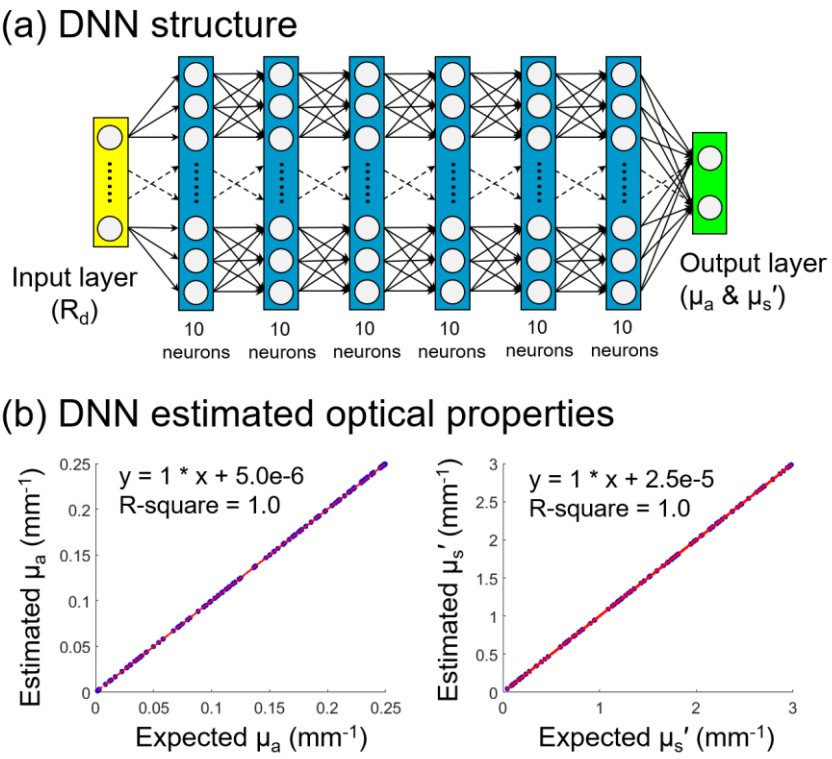

Figure 6.2.3. Structure of proposed deep learning model and estimations on randomly generated test data.

6.2.4: Comparison on randomly generated data

In order to compare the iterative, nearest-search, the proposed DNN method, a new test set of 10,000 combinations of OPs were randomly generated in the range of [0, 0.25] mm^{-1} for μ_a and [0, 3] mm^{-1} for μ_s', and corresponding 5-fx R_d values were generated by the MC forward model. The above inverse methods were used to process the test set for the inversion of R_d to OPs. Both MC and diff as forward model were used in the iterative method. Both inversion accuracy and computational speed were compared between the

above methods. In addition, in order to test inversion performance with existence of noise, a separate test set was made by adding 0 mean and 2% Gaussian noise on the R_d values. The computation was conducted on a desktop computer with Intel i7-7700K 4.20GHz CPU and 16 GB RAM.

6.3: Results

6.3.1: Comparison of Iterative method, nearest-search, and DNN on accuracy

Fig. 6.3.1 shows the extracted optical properties against their expected values without noise on the R_d values. Each blue dot represents an optical property data point. The red line in each subplot represents the identify prediction line, where a perfect OPs estimation should be located exactly on it. The mean and standard deviation values of percent errors of extracted OPs are shown in each subplot. Fig. 6.3.1b shows the results of the iterative method using diffusion equation as the forward model, which gives relatively the worst accuracy among all methods. The nearest-search method in Fig. 6.3.1c has better performance than the diffusion equation iterative method, but worse than the DNN and iterative MC method. Fig. 6.3.1d shows the results of the proposed DNN method, which is better than the diffusion equation iterative method and the nearest-search method. It also has similar performance compared to the MC iterative method.

Fig. 6.3.2 shows the extracted optical properties against their expected values with 2% Gaussian noise on the R_d values. The diffusion equation iterative method still has the worst performance. The nearest-search method has slightly worse accuracy than the MC iterative method. In general, most observations made in Fig. 6.3.1 still hold in Fig. 6.3.2.

Notably, the proposed DNN method achieves better performance than the MC iterative method with smaller estimation error and variance.

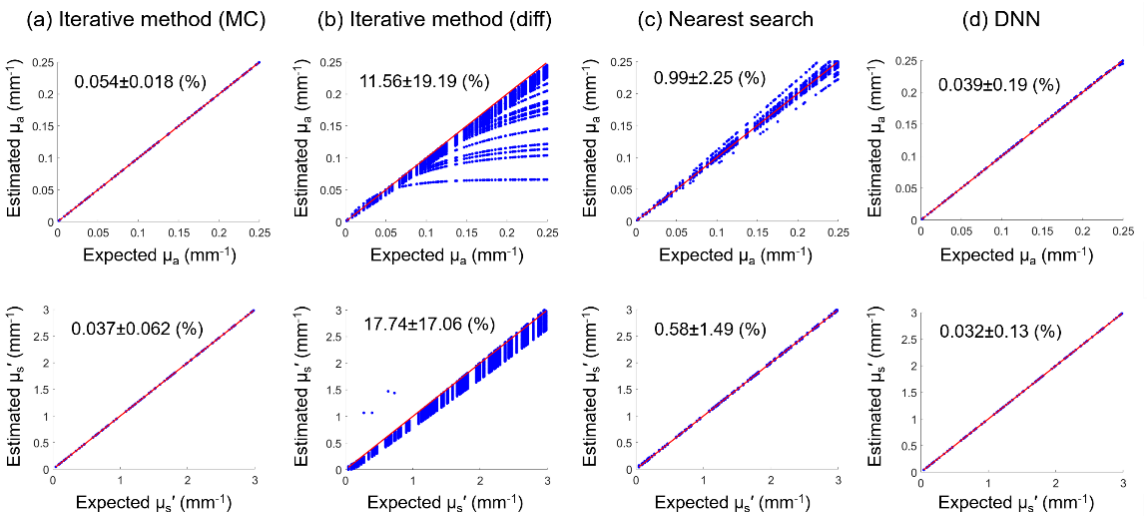

Figure 6.3.1. Comparison of accuracy for the inversion from R_d to OPs without noise.

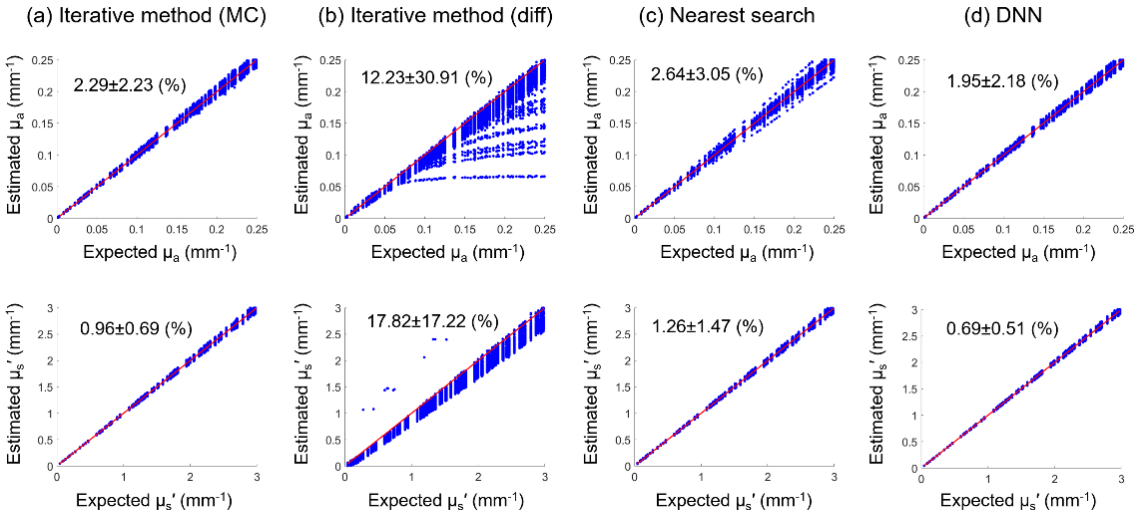

Figure 6.3.2. Comparison of accuracy for the inversion from R_d to OPs with 2% Gaussian noise.

6.3.2: Comparison of iterative method, nearest-search, and DNN on speed

Table 9 shows the speed comparison of the inversion methods where each computation was repeated 10 times. For a total of 10,000 inversions from R_d to OPs, the MC iterative method took over 670 seconds, while the other iterative method using diffusion equation as forward model took 15.6 s. The nearest-search method took 1.7 s which was faster than both versions of iterative methods. The proposed DNN method only took 0.0050 s, which was two orders of magnitude faster than the nearest-search, three orders of magnitude faster than the diffusion equation iterative method, and five orders of magnitude faster than the MC iterative method. Such speed improvement is also true when processing larger scale inversions with 696×520 data points.

Speed / # data point	Iterative method (MC)	Iterative method (diff)	Nearest-search	DNN
10000	673.60±15.32 s	15.62±0.10 s	1.70±0.087 s	**0.0050±6.4e-4 s**
696×520	39412.34±8744.94 s	467.08±4.85 s	60.16±0.69 s	**0.23±0.0085 s**

Table 9. Comparison of speed for the inversion from R_d to OPs.

6.4: Discussion and Conclusion

With noise-free R_d values, the MC iterative method shows similar accuracy with the DNN method due to the fact that the iterative searching algorithm is able to effectively search entire optical property space in a continuous manner. In contrast, the proposed DNN model was only trained with a relatively sparsely sampled data points from the optical property space (250 × 300). The diffusion equation iterative method shows worst accuracy, potentially due to the fact that the inversion is based on a different forward model other

than the Monte Carlo.

The accuracy of nearest-search and DNN can both potentially be improved with more densely sampled OPs in the optical property space. With both accuracy and speed as metrics, the DNN method outperforms existing methods as well as other modified fast inversion method. In addition to the 5-fx demonstrated in this work, we expect the proposed deep learning framework can be adopted and trained for other combinations of spatial frequencies as well.

Being able to perform fast optical property extraction for multi-fx SFDI can be useful for real-time SFDI applications with enhanced accuracy performance, and reduced uncertainty in extracted OPs.[124,125] Given pre-determined wavelengths and proper training data, one could also go directly from multi-fx R_d input values to chromophore concentrations, such as hemodynamic values, which makes real-time feedback for surgical guidance possible.

In this work, we introduced a deep learning framework in multi-fx SFDI for fast and accurate inversion of diffuse reflectance to optical properties. The proposed method shows outstanding accuracy compared to previous methods. The proposed method is also ×300 – ×100,000 faster than the other methods.

CHAPTER SEVEN: CONCLUSIONS AND FUTURE WORK

The final chapter summarizes the conclusions of this body of work, offers ideas for related future work, and presents some additionally preliminary results.

7.1: Summaries

Chapter 3 presents fluorophore quantum yield mapping in diffusive media. A fluorescence correction model is applied based on measured tissue optical properties by SFDI. Fluorophore quantum yield in diffusive media such as tissues can be estimated from the corrected fluorescence. This method is shown to have accurate results on fluorophore quantum yield estimation. It is also demonstrated to be effective on different fluorophores. This method has potential application on probing tissue potential local environment such as pH or temperature.

Chapter 4 proposes and validates an image artifact correction algorithm for SFDI. It is shown that compared to previous method, more accurate optical properties and chromophore extraction can be achieved with the proposed correction algorithm for SFDI, when applied to objects that have highly curved surface geometry.

Chapter 5 presents SFDI in the SWIR wavelengths and enables extraction of widefield biomarker information, such as water and lipid content in tissues. Multiple applications are demonstrated with the proposed SWIR-SFDI system. Water content is dynamically monitored in simulated edema and inflammation in small animal model. Lipid content on small animal tumor is also measured and validated with histology staining. *In vivo* classification of adipose tissue type through intact skin is demonstrated. Last, the system is applied to human blood lipids monitoring on a number of ten volunteers, and the

results are compared with blood draws with a lipid panel.

Chapter 6 addresses the bottleneck of SFDI processing. A deep learning framework is designed and validated. The SFDI inversion speed from diffuse reflectance to optical properties is improved by ×300 – ×100,000.

7.2: Future Work

The work in this thesis provides many potential future directions, a few of which are discussed here:

1. The fluorophore quantum yield mapping presented in Chapter 3 has potential as an *in vivo* tool. Tissue local environment such as temperature and pH can potentially be non-invasively measured with this method. With a pH sensitive dye such as SNARF-5, pH in small animal tumor model may be extracted and monitored longitudinally in a new way. Furthermore. Fluorophores such as ICG that are FDA-approved can also be explored for *in vivo* human applications.
2. Chapter 5 presents *in vivo* mapping of water and lipid with shortwave infrared wavelengths. In particular, blood lipid measurements are correlated with blood draw lipid panel. This highlights the possibility of non-invasive longitudinal blood lipids monitoring with this technique. With a two-layer model that takes into account the superficial skin-layer, blood lipids can potentially be measured with improved accuracy.
3. In addition to simultaneous mapping of water and lipid content using SWIR wavelengths, other chromophores with absorption signatures in this wavelength

range can also be probed, such as collagen. The spectral un-mixing in the presence of multiple chromophores is likely to be challenging.

4. Deep learning has been proven useful in many other fields, and there will be increasingly more applications in biomedical optics as well. Chapter 6 demonstrates deep neural network to speed up SFDI optical property inversion by ×300 – ×100,000. This framework can also be extended to other inverse problems, such as the optical property inversion in digital diffuse optical spectroscopic imaging (dDOSI), where the post-processing being a major bottleneck for the speed of tissue information extraction. Potentially it can also be applied to diffuse optical tomography in 3-D optical property reconstruction for tissues.

7.3: Preliminary results

This section presents some preliminary results based on the possible futures direction in previous section.

7.3.1: Extraction of Collagen Concentrations with SFDI

Collagen is an important protein and is also the most abundant in humans.[126] Similar to lipids, it has absorption features in the shortwave infrared. [45] Here measurement on real tissues is conducted and a theoretical analysis of collagen concentration estimation is discussed.

In addition, in order to simulate the spectral un-mixing of water, lipid, and collagen, a theoretical analysis is conducted. Figure 7.3.1 shows percent error of simulated concentration extraction of water, lipid, and collagen in tissues. Possible combinations are

sampled with water in the range of 5% – 90%, lipid in the range of 1% – 90%, and collagen in the range of 1% – 90%, where the total of the three components remains 100%. Specifically, known extinction spectra of those chromophores are sampled to generate theoretical μ_a at 900 – 1300 nm, with either 5 nm or 40 nm increments. Then 2% Gaussian noise is added to the μ_a spectra. Chromophores are reconstructed using Beer's law with the noisy spectra and then compared to the ground truth. The goal of the simulation is to get a sense of how the extraction accuracy potentially relates to the wavelength density in measurement. Fig. 7.3.1 shows that in the 900 – 1300 nm wavelength range, even with 81 wavelengths, with 2% Gaussian noise in the absorption, the percent error could still be relatively high for collagen. With fewer wavelengths, the average percent error for collagen can be over 10%. This simulation study shows that collagen extraction is challenging with spectral un-mixing in the presence of multiple chromophores. In order for an accurate collagen concentration estimation, potentially more wavelengths or lower measurement noise are required.

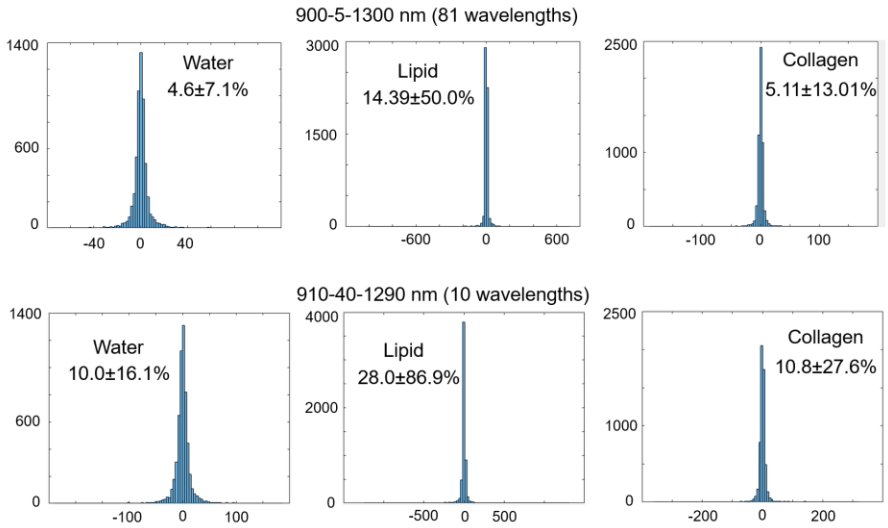

Figure 7.3.1. Percent error of simulated chromophore extraction with water, lipid, and collagen.

7.3.2: superfast deep neural network inverse model digital Diffuse Optical Spectroscopic Imaging (dDOSI)

As discussed in previous section, in addition to multi-fx SFDI optical property inversion, deep learning can potentially be used as a general fast inversion framework in other optical imaging modalities as well. Here a superfast inversion model based on deep neural network for digital Diffuse Optical Spectroscopic Imaging (dDOSI) is presented. dDOSI is a novel optical technology that allows fast measurement of tissue optical properties.[127] The data acquisition for dDOSI can be up to 97 Hz. However, the bottleneck of this technology is the inversion from measured data to tissue optical properties, since the inversion is based on iterative computations.[127] In order to speed up the inversion process, a deep neural network (DNN) inverse model is designed and validated in Fig. 7.3.2. It shows the expected and estimated optical properties from the original iterative

method and the DNN. It demonstrates that the DNN has similar or better accuracy performance than the iterative method. Speed wise, 10 and 100 measurements are simulated and repeated 10 times to compare the speed of optical property inversion from the measured amplitude and phase data, shown in Table 10. It demonstrates that the DNN inverse model improves the computational speed by two to three orders of magnitude. Such speed increase opens possibility of real-time tissue information extraction with dDOSI. Fig. 7.3.3 demonstrates dDOSI measurements on a human thumb. The optical absorption and hemoglobin fluctuations are clearly visible with heart pulsing. The measurements were conducted at approximately 25 Hz. Real-time feedback of such information is now possible with the DNN inverse model.

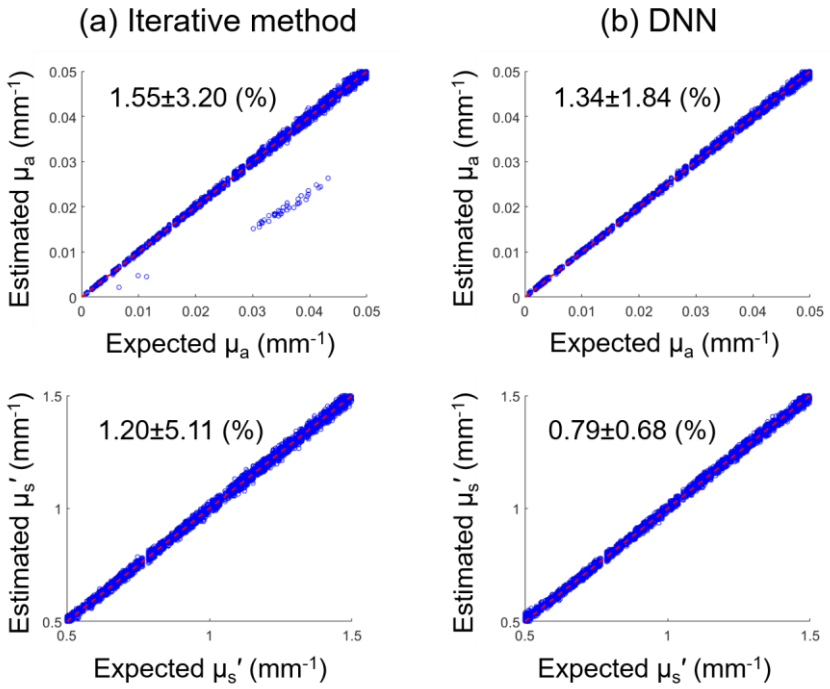

Figure 7.3.2. Expected and estimated optical properties of the iterative method and the deep neural network method.

Speed / # measurements (s)	Iterative method	DNN
10	0.21 ± 0.034	4.9e-4 ± 4.7e-4
100	2.7 ± 0.074	5.6e-4 ± 4.3e-4

Table 10. Speed comparison of the iterative method and DNN for dDOSI optical property inversion.

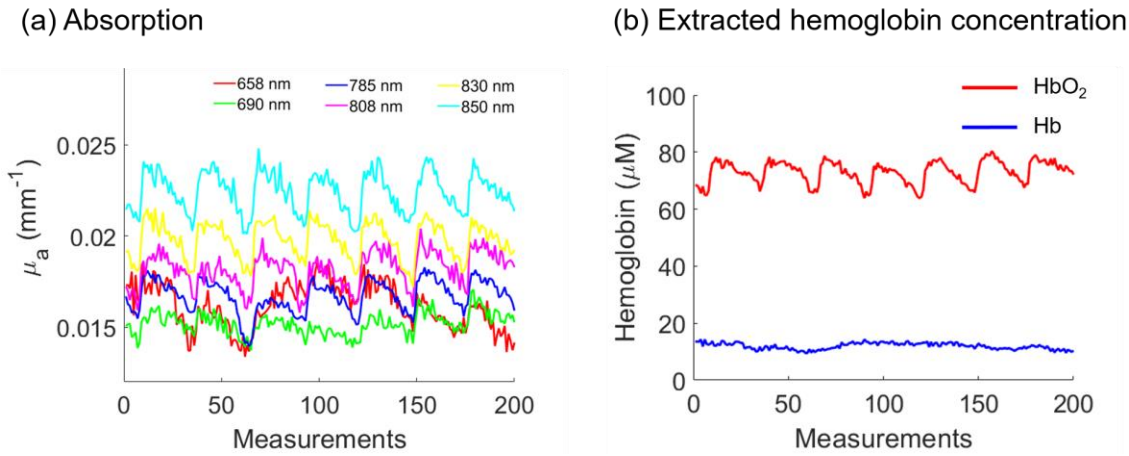

Figure 7.3.3. Thumb measurements of dDOSI. Hemoglobin information is extracted from the measured absorption. The measurements were conducted at approximately 25 Hz. Absorption and oxy-hemoglobin pulses from heart pulsing are clearly visible.

7.4: Conclusion

The body of this work has aimed to build novel instrument, improve methodology, expend applications, and incorporate technology in other fields to enhance current imaging techniques. Biomedical optics has great potential to provide additional tissue information in the clinic and improve patient outcomes. Additional work needs to be done toward this goal. However, it is not only the technology advancement, but also habit nurturing, product cost, and marketing that hold the prosperity of biomedical optics in the real world. As an "apprentice" in research,[128] it is my hope that this dissertation at least contributes to the first wheel.

BIBLIOGRAPHY

1. Veselkov KA, Mirnezami R, Strittmatter N, et al. Chemo-informatic strategy for imaging mass spectrometry-based hyperspectral profiling of lipid signatures in colorectal cancer. *Proceedings of the National Academy of Sciences of the United States of America*. 2014;111(3):1216-1221. doi:10.1073/pnas.1310524111.

2. Adada M, Luberto C, Canals D, et al. Biophysics of cell membrane lipids in cancer drug resistance: Implications for drug transport and drug delivery with nanoparticles. *Journal of Biological Chemistry*. 2013;102(2):38-53. doi:10.1016/j.canlet.2003.08.034.

3. Cerussi AE, Tanamai VW, Hsiang D, Butler J, Mehta RS, Tromberg BJ. Diffuse optical spectroscopic imaging correlates with final pathological response in breast cancer neoadjuvant chemotherapy. *Philosophical Transactions. Series A, Mathematical, Physical, and Engineering Sciences*. 2011;369(1955):4512-4530. doi:10.1098/rsta.2011.0279.

4. Loeffler M, Krüger JA, Niethammer AG, Reisfeld RA. Targeting tumor-associated fibroblasts improves cancer chemotherapy by increasing intratumoral drug uptake. *Journal of Clinical Investigation*. 2006;116(7):1955-1962. doi:10.1172/JCI26532.

5. Egeblad M, Rasch MG, Weaver VM. Dynamic interplay between the collagen scaffold and tumor evolution. *Current Opinion in Cell Biology*. 2010;22(5):697-706. doi:10.1016/j.ceb.2010.08.015.

6. Conklin MW, Eickhoff JC, Riching KM, et al. Aligned collagen is a prognostic signature for survival in human breast carcinoma. *American Journal of Pathology*. 2011;178(3):1221-1232. doi:10.1016/j.ajpath.2010.11.076.

7. Wang P, Li J, Wang P, et al. Label-free quantitative imaging of cholesterol in intact tissues by hyperspectral stimulated Raman scattering microscopy. *Angewandte Chemie - International Edition in English*. 2013;52(49):13042-13046. doi:10.1002/anie.201306234.

8. Cerussi A, Shah N, Hsiang D, Durkin A, Butler J, Tromberg BJ. In vivo absorption, scattering, and physiologic properties of 58 malignant breast tumors determined by broadband diffuse optical spectroscopy. *Journal of Biomedical Optics*. 2015;11(4):44005. doi:10.1117/1.2337546.

9. Nachabé R, Hendriks BHW, Desjardins AE, van der Voort M, van der Mark MB, Sterenborg HJCM. Estimation of lipid and water concentrations in scattering media with diffuse optical spectroscopy from 900 to 1,600 nm. *Journal of Biomedical Optics*. 2015;15(3):37015. doi:10.1117/1.3454392.

10. Caplan JD, Waxman S, Nesto RW, Muller JE. Near-Infrared Spectroscopy for the Detection of Vulnerable Coronary Artery Plaques. *Journal of the American College of Cardiology*. 2006;47(8 SUPPL.). doi:10.1016/j.jacc.2005.12.045.

11. Fleming CP, Eckert J, Halpern EF, Gardecki JA, Tearney GJ. Depth resolved detection of lipid using spectroscopic optical coherence tomography. *Biomedical Optics Express*. 2013;4(8):1269. doi:10.1364/BOE.4.001269.

12. Provenzano PP, Eliceiri KW, Campbell JM, Inman DR, White JG, Keely PJ. Collagen reorganization at the tumor-stromal interface facilitates local invasion. *BMC Medicine*. 2006;4(1):38. doi:10.1186/1741-7015-4-38.

13. Provenzano PP, Inman DR, Eliceiri KW, et al. Collagen density promotes mammary tumor initiation and progression. *BMC Medicine*. 2008;6(1):11. doi:10.1186/1741-7015-6-11.

14. Taroni P, Pifferi A, Quarto G, et al. Noninvasive assessment of breast cancer risk using time-resolved diffuse optical spectroscopy. *Journal of Biomedical Optics*. 2010;15(6):60501. doi:10.1117/1.3506043.

15. Taroni P, Quarto G, Pifferi A, et al. Breast tissue composition and its dependence on demographic risk factors for breast cancer: non-invasive assessment by time domain diffuse optical spectroscopy. *PLoS One*. 2015;10(6):e0128941. doi:10.1371/journal.pone.0128941.

16. Taroni P, Pifferi A, Salvagnini E, Spinelli L, Torricelli A, Cubeddu R. Seven-wavelength time-resolved optical mammography extending beyond 1000 nm for breast collagen quantification. *Optics Express*. 2009;17(18):15932-15946. doi:10.1364/OE.17.015932.

17. Quarto G, Spinelli L, Pifferi A, et al. Estimate of tissue composition in malignant and benign breast lesions by time-domain optical mammography. *Biomedical Optics Express*. 2014;5(10):3684-3698. doi:10.1364/BOE.5.003684.

18. Taroni P, Comelli D, Pifferi A, Torricelli A, Cubeddu R. Absorption of collagen: effects on the estimate of breast composition and related diagnostic implications. *Journal of Biomedical Optics*. 2007;12(1):14021-014021-014024. doi:10.1117/1.2699170.

19. Gavhane YN, Shete a S, Bhagat a K, et al. Solid Tumors : Facts , Challenges and Solutions. *International Journal of Pharma Science and Research*. 2011;2(1):1-12.

20. Choi K-H, Yoo IR, Han EJ, et al. Prognostic Value of Metabolic Tumor Volume Measured by (18)F-FDG PET/CT in Locally Advanced Head and Neck Squamous Cell Carcinomas Treated by Surgery. *Nuclear Medicine and Molecular Imaging*.

2011;45(1):43-51. doi:10.1007/s13139-010-0063-7.

21. Shah N, Cerussi AE, Jakubowski D, Hsiang D, Butler J, Tromberg BJ. The role of diffuse optical spectroscopy in the clinical management of breast cancer. *Disease Markers*. 2004;19(2-3):95-105.

22. Roblyer D, Ueda S, Cerussi A, et al. Optical imaging of breast cancer oxyhemoglobin flare correlates with neoadjuvant chemotherapy response one day after starting treatment. *Proceedings of the National Academy of Sciences of the United States of America*. 2011;108(35):14626-14631. doi:10.1073/pnas.1013103108.

23. Papadopoulos MC, Saadoun S, Binder DK, Manley GT, Krishna S, Verkman AS. Molecular mechanisms of brain tumor edema. *Neuroscience*. 2004;129(4):1011-1020. doi:10.1016/j.neuroscience.2004.05.044.

24. Bydlon TM, Nachab?? R, Ramanujam N, Sterenborg HJCM, Hendriks BHW. Chromophore based analyses of steady-state diffuse reflectance spectroscopy: Current status and perspectives for clinical adoption. *Journal of Biophotonics*. 2015;8(1-2):9-24. doi:10.1002/jbio.201300198.

25. Zhou C, Choe R, Shah N, et al. Diffuse optical monitoring of blood flow and oxygenation in human breast cancer during early stages of neoadjuvant chemotherapy. *Journal of Biomedical Optics*. 2013;12(5):51903. doi:10.1117/1.2798595.

26. Cuccia DJ, Bevilacqua F, Durkin AJ, Tromberg BJ. Modulated imaging: quantitative analysis and tomography of turbid media in the spatial-frequency domain. *Optics Letters*. 2005;30(11):1354-1356. doi:10.1364/OL.30.001354.

27. Cuccia DJ, Bevilacqua F, Durkin AJ, Ayers FR, Tromberg BJ. Quantitation and mapping of tissue optical properties using modulated imaging. *Journal of Biomedical Optics*. 2009;14(April 2009):24012. doi:10.1117/1.3088140.

28. Martinelli M, Gardner A, Cuccia D, Hayakawa C, Spanier J, Venugopalan V. Analysis of single Monte Carlo methods for prediction of reflectance from turbid media. *Optics Express*. 2011;19(20):19627. doi:10.1364/OE.19.019627.

29. Gioux S, Mazhar A, Cuccia DJ, Durkin AJ, Tromberg BJ, Frangioni J V. Three-dimensional surface profile intensity correction for spatially modulated imaging. *Journal of Biomedical Optics*. 2009;14(3):34045. doi:10.1117/1.3156840.

30. Nguyen JQ, Crouzet C, Mai T, et al. Spatial frequency domain imaging of burn wounds in a preclinical model of graded burn severity. *Journal of Biomedical Optics*. 2013;18(6):66010. doi:10.1117/1.JBO.18.6.066010.

31. Sharif S a., Taydas E, Mazhar a., et al. Noninvasive clinical assessment of port-wine stain birthmarks using current and future optical imaging technology: A review. *British Journal of Dermatology*. 2012;167(6):1215-1223. doi:10.1111/j.1365-2133.2012.11139.x.

32. Gioux S, Mazhar A, Lee BT, et al. Preclinical and clinical validation of a novel oxygenation imaging system. *Spectroscopy*. 2011;7896:78961R-78961R-10. doi:10.1117/12.875603.

33. Mazhar A, Sharif S a., Saggese S, Choi B, Cuccia DJ, Durkin AJ. Implementation of an LED based Clinical Spatial Frequency Domain Imaging System. *Proceedings of SPIE*. 2012;8254:82540A-82540A-7. doi:10.1117/12.909813.

34. Rohrbach DJ, Muffoletto D, Huihui J, et al. Preoperative mapping of nonmelanoma skin cancer using spatial frequency domain and ultrasound imaging. *Academic Radiology*. 2014;21(2):263-270. doi:10.1016/j.acra.2013.11.013.

35. Nadeau KP, Khoury P, Mazhar A, Cuccia D, Durkin a. J. Component and system evaluation for the development of a handheld point-of-care spatial frequency domain imaging (SFDI) device. *Proceedings of SPIE*. 2013;8573:857304-857304-857310. doi:10.1117/12.2004909.

36. Saager RB, Cuccia DJ, Saggese S, Kelly KM, Durkin AJ. Quantitative fluorescence imaging of protoporphyrin IX through determination of tissue optical properties in the spatial frequency domain. *Journal of Biomedical Optics*. 2011;16(12):126013. doi:10.1117/1.3665440.

37. Konecky SD, Mazhar A, Cuccia D, Durkin AJ, Schotland JC, Tromberg BJ. Quantitative optical tomography of sub-surface heterogeneities using spatially modulated structured light. *Optics Express*. 2009;17(17):14780-14790. doi:10.1364/OE.17.014780.

38. Konecky SD, Owen CM, Rice T, et al. Spatial frequency domain tomography of protoporphyrin IX fluorescence in preclinical glioma models. *Journal of Biomedical Optics*. 2012;17(5):56008. doi:10.1117/1.JBO.17.5.056008.

39. Zhao Y, Roblyer D. Spatial mapping of fluorophore quantum yield in diffusive media. *Journal of Biomedical Optics*. 2015;20(8):86013. doi:10.1117/1.JBO.20.8.086013.

40. Diep P, Pannem S, Sweer J, et al. Three-dimensional printed optical phantoms with customized absorption and scattering properties. *Biomedical Optics Express*. 2015;6(11):4212. doi:10.1364/BOE.6.004212.

41. Ponticorvo A, Burmeister DM, Yang B, Choi B, Christy RJ, Durkin AJ.

Quantitative assessment of graded burn wounds in a porcine model using spatial frequency domain imaging (SFDI) and laser speckle imaging (LSI). *Biomedical Optics Express*. 2014;5(10):3467-3481. doi:10.1364/BOE.5.003467.

42. Gioux S, Mazhar A, Lee BT, et al. First-in-human pilot study of a spatial frequency domain oxygenation imaging system. *Journal of Biomedical Optics*. 2011;16(8):86015. doi:10.1117/1.3614566.

43. Mazhar A, Saggese S, Pollins AC, Cardwell NL, Nanney L, Cuccia DJ. Noncontact imaging of burn depth and extent in a porcine model using spatial frequency domain imaging. *Journal of Biomedical Optics*. 2014;19(2):20901. doi:10.1117/1.

44. Beckman Laser Institute. NIR Tissue Absorption. http://dosi.bli.uci.edu/research/.

45. Allen TJ, Hall A, Dhillon AP, Owen JS, Beard PC. Spectroscopic photoacoustic imaging of lipid-rich plaques in the human aorta in the 740 to 1400 nm wavelength range. *Journal of Biomedical Optics*. 2012;17(6):61209. doi:10.1117/1.JBO.17.6.061209.

46. Mazhar A, Dell S, Cuccia DJ, et al. Wavelength optimization for rapid chromophore mapping using spatial frequency domain imaging. *Journal of Biomedical Optics*. 2010;15(6):61716. doi:10.1117/1.3523373.

47. Wilson RH, Nadeau KP, Jaworski FB, Tromberg BJ, Durkin AJ. Review of short-wave infrared spectroscopy and imaging methods for biological tissue characterization. *Journal of Biomedical Optics*. 2015;20(3):30901. doi:10.1117/1.JBO.20.3.030901.

48. Beard P. Biomedical photoacoustic imaging. *Interface Focus*. 2011;1(4):602-631. doi:10.1098/rsfs.2011.0028.

49. Weissleder R, Ntziachristos V. Shedding light onto live molecular targets. *Nature Medicine*. 2003;9(1):123-128. doi:10.1038/nm0103-123.

50. Laverdant J, de Marcillac WD, Barthou C, et al. Experimental Determination of the Fluorescence Quantum Yield of Semiconductor Nanocrystals. *Materials (Basel)*. 2011;4(7):1182-1193. doi:10.3390/ma4071182.

51. Han J, Burgess K. Fluorescent indicators for intracellular pH. *Chemical Reviews*. 2010;110:2709-2728. doi:10.1021/cr900249z.

52. Magde D, Rojas GE, Seybold PG. Solvent dependence of the fluorescence lifetimes of zanthene dyes. *Photochemistry and Photobiology*. 1999;70(5):737-744.

53. Magde D, Wong R, Seybold PG. Fluorescence quantum yields and their relation to lifetimes of rhodamine 6G and fluorescein in nine solvents: improved absolute standards for quantum yields. *Photochemistry and Photobiology*. 2002;75(4):327-334. doi:10.1562/0031-8655(2002)0750327FQYATR2.0.CO2.

54. Chang TL, Cheung HC. Solvent effects on the photoisomerization rates of the zwitterionic and the cationic forms of rhodamine B in protic solvents. *Journal of Physical Chemistry*. 1992;96:4874–4878. doi:10.1021/j100191a028.

55. Ware WR, Baldwin B a. Effect of Temperature on Fluorescence Quantum Yields in Solution. *Journal of Chemical Physics*. 1965;43(4):1194. doi:10.1063/1.1696903.

56. Brouwer AM. Standards for photoluminescence quantum yield measurements in solution (IUPAC Technical Report). *Pure and Applied Chemistry*. 2011;83(12): 2213-2228. doi:10.1351/PAC-REP-10-09-31.

57. Crosby G a., Demas JN. Measurement of photoluminescence quantum yields. Review. *Journal of Physical Chemistry*. 1971;75:991-1024. doi:10.1021/j100678a001.

58. Karstens T, Kobs K. Rhodamine B and rhodamine 101 as reference substances for fluorescence quantum yield measurements. *Journal of Physical Chemistry*. 1980;84(14):1871-1872. doi:10.1021/j100451a030.

59. Olmsted J. Calorimetric determinations of absolute fluorescence quantum yields. *Journal of Physical Chemistry*. 1979;83(20):2581-2584. doi:10.1021/j100483a006.

60. Wu J, Feld MS, Rava RP. Analytical model for extracting intrinsic fluorescence in turbid media. *Applied Optics*. 1993;32(19):3585-3595. doi:10.1364/AO.32.003585.

61. Gardner CM, Jacques SL, Welch J. Fluorescence spectroscopy of tissue: recovery of intrinsic fluorescence from measured fluorescence. *Applied Optics*. 1996;35:1780-1792. doi:10.1364/AO.35.001780.

62. Gardner CM, Jacques SL, Welch J. Light transport in tissue: Accurate expressions for one-dimensional fluence rate and escape function based upon Monte Carlo simulation. *Lasers in Surgery and Medicine*. 1996;18:129-138. doi:10.1002/(SICI)1096-9101(1996)18:2<129::AID-LSM2>3.0.CO;2-U.

63. Yafi A, Vetter TS, Scholz T, et al. Postoperative quantitative assessment of reconstructive tissue status in a cutaneous flap model using spatial frequency domain imaging. *Plastic and Reconstructive Surgery*. 2011;127:117-130. doi:10.1097/PRS.0b013e3181f959cc.

64. Pal R, Parker D. A ratiometric optical imaging probe for intracellular pH based on modulation of europium emission. *Organic & Biomolecular Chemistry*. 2008;6(6): 1020-1033. doi:10.1039/b718993a.

65. Gannot I, Ron I, Hekmat F, Chernomordik V, Gandjbakhche A. Functional optical detection based on pH dependent fluorescence lifetime. *Lasers in Surgery and Medicine*. 2004;35(5):342-348. doi:10.1002/lsm.20101.

66. Zhao Y, Tabassum S, Piracha S, Nandhu MS, Viapiano M, Roblyer D. Angle correction for small animal tumor imaging with spatial frequency domain imaging (SFDI). *Biomedical Optics Express*. 2016;7(6):2373. doi:10.1364/BOE.7.002373.

67. Minnaert M. The reciprocity principle in lunar photometry. *Astrophysical Journal*. 1941;93:403. doi:10.1086/144279.

68. Ekstrand S. Landsat TM-Based Forest Damage Assessment: Correction for Topographic Effects. *Photogrammetric Engineering and Remote Sensing*. 1996; 62(2):151-161.

69. Boyd S, Vandenberghe L. *Convex Optimization*. Cambridge University Press; 2004. doi:10.1080/10556781003625177.

70. McClatchy DM, Krishnaswamy V, Kanick SC, et al. High spatial frequency structured light imaging for intraoperative breast tumor margin assessment. *Proceedings of SPIE, Advanced Biomedical and Clinical Diagnostic and Surgical Guidance Systems XII*. 2015;9313:931304-931308. doi:10.1117/12.2080134.

71. Walker-Samuel S, Ramasawmy R, Torrealdea F, et al. In vivo imaging of glucose uptake and metabolism in tumors. *Nature Medicine*. 2013;19(8):1067-1072. doi:10.1038/nm.3252.

72. Merritt S, Gulsen G, Chiou G, et al. Comparison of water and lipid content measurements using diffuse optical spectroscopy and MRI in emulsion phantoms. *Technology in Cancer Research & Treatment*. 2003;2(6):563-569. doi:d=3015&c=4125&p=11944&do=detail [pii].

73. Kienle A, Lilge L, Patterson M, Hibst R. Spatially resolved absolute diffuse reflectance measurements for noninvasive determination of the optical scattering and absorption coefficients of biological tissue. *Applied Optics*. 1996;35(13):2304-2314. http://www.opticsinfobase.org/abstract.cfm?&id=46967.

74. Bevilacqua F, Berger AJ, Cerussi AE, Jakubowski D, Tromberg BJ. Broadband absorption spectroscopy in turbid media by combined frequency-domain and steady-state methods. *Applied Optics*. 2000;39(34):6498. doi:10.1364/AO.39.006498.

75. Tabassum S, Zhao Y, Istfan R, Wu J, Waxman DJ, Roblyer D. Feasibility of spatial frequency domain imaging (SFDI) for optically characterizing a preclinical oncology model. *Biomedical Optics Express*. 2016;7(10):4154. doi:10.1364/BOE.7.004154.

76. Thimsen E, Sadtler B, Berezin MY. Shortwave-infrared (SWIR) emitters for biological imaging: A review of challenges and opportunities. *Nanophotonics*. 2017;6(5):1043-1054. doi:10.1515/nanoph-2017-0039.

77. Wilson RH, Nadeau KP, Jaworski FB, et al. Quantitative short-wave infrared multispectral imaging of in vivo tissue optical properties. *Journal of Biomedical Optics* 2014;19(8):86011. doi:10.1117/1.JBO.19.8.086011.

78. Lin AJ, Koike MA, Green KN, et al. Spatial frequency domain imaging of intrinsic optical property contrast in a mouse model of alzheimer's disease. *Annals of Biomedical Engineering*. 2011;39(4):1349-1357. doi:10.1007/s10439-011-0269-6.

79. Weber JR, Cuccia DJ, Johnson WR, et al. Multispectral imaging of tissue absorption and scattering using spatial frequency domain imaging and a computed-tomography imaging spectrometer. *Journal of Biomedical Optics*. 2011;16(1): 11015. doi:10.1117/1.3528628.

80. Sho Asakura, Oosawa F. Interaction between particles suspended in solutions of macromolecules. *Journal of Polymer Science*. 1958;33(126):183-192.

81. Assadi H, Karshafian R, Douplik A. Optical scattering properties of intralipid phantom in presence of encapsulated microbubbles. *International Journal of Photoenergy*. 2014;2014. doi:10.1155/2014/471764.

82. Weissleder R. A clearer vision for in vivo imaging. *Nature Biotechnology*. 2001; 19(4):316-317. doi:10.1038/86684.

83. Park BK, Heo MY, Park H, Kim HP. Inhibition of TPA-induced cyclooxygenase-2 expression and skin inflammation in mice by wogonin, a plant flavone from Scutellaria radix. *European Journal of Pharmacology*. 2001;425(2):153-157. doi:10.1016/S0014-2999(01)01187-6.

84. Cao Q, Cai W, Li ZB, et al. PET imaging of acute and chronic inflammation in living mice. *European Journal of Nuclear Medicine and Molecular Imaging*. 2007;34(11):1832-1842. doi:10.1007/s00259-007-0451-0.

85. Ramirez-Zacarias JL, Castro-Mufiozledo F, Kuri-Harcuch W. Quantitation of adipose conversion and triglycerides by staining intracytoplasmic lipids with oil red O. *Histochemistry*. 1992;97(6):493-497.

86. Mann A, Thompson A, Robbins N, Blomkalns AL. Localization, Identification, and Excision of Murine Adipose Depots. *Journal of Visualized Experiments: JoVE*. 2014;(94):1-7. doi:10.3791/52174.

87. Deng Y, Zhao Y, Liu Y, Dai Q. Differences Help Recognition: A Probabilistic Interpretation. *PLoS One*. 2013;8(5). doi:10.1371/journal.pone.0063385.

88. Bishop CM. *Pattern Recognition and Machine Learning*. Vol 53.; 2013. doi:10.1017/CBO9781107415324.004.

89. Meacham CE, Morrison SJ. Tumour heterogeneity and cancer cell plasticity. *Nature*. 2013;501(7467):328-337. doi:10.1038/nature12624.

90. Marusyk A, Almendro V, Polyak K. Intra-tumour heterogeneity: a looking glass for cancer? *Nature Reviews. Cancer*. 2012;12(5):323-334. doi:10.1038/nrc3261.

91. Siu L, Snyder A, Stower H, et al. Toward understanding and exploiting tumor heterogeneity. *Nature Medicine.* 2016;21(8):846-853. doi:10.1038/nm.3915.Toward.

92. Burrell RA, McGranahan N, Bartek J, Swanton C. The causes and consequences of genetic heterogeneity in cancer evolution. *Nature*. 2013;501(7467):338-345. doi:10.1038/nature12625.

93. Chechi K, Nedergaard J, Richard D. Brown adipose tissue as an anti-obesity tissue in humans. *Obesity Reviews*. 2014;15(2):92-106. doi:10.1111/obr.12116.

94. Bartelt A, Heeren J. Adipose tissue browning and metabolic health. *Nature Reviews. Endocrinology*. 2014;10(1):24-36. doi:10.1038/nrendo.2013.204.

95. Cypess AM, Lehman S, Williams G, et al. Identification and Importance of Brown Adipose Tissue in Adult Humans. *New England Journal of Medicine*. 2009; 360(15):1509-1517. doi:10.1056/NEJMoa0810780.

96. Bordone L, Guarente L. Calorie restriction, SIRT1 and metabolism: understanding longevity. *Nature Reviews. Molecular Cell Biology*. 2005;6(4):298-305. doi:10.1038/nrm1616.

97. Giralt M, Villarroya F. White, brown, beige/brite: Different adipose cells for different functions? *Endocrinology*. 2013;154(9):2992-3000. doi:10.1210/en.2013-1403.

98. Ishibashi J, Seale P. Beige Can Be Slimming. *Science*. 2010;328(5982):1113-1114. doi:10.1126/science.1190816.

99. Hubert HB, Feinleib M, McNamara PM CW. Obesity as an independent risk factor

for cardiovascular disease: a 26-year follow-up of participants in the Framingham Heart Study. *Circulation*. 1983;67:968-977. doi:10.1161/01.CIR.67.5.968.

100. R. Michael Gower, Huaizhu Wu, Greg A. Foster, Sridevi Devaraj SIS. CD11c/CD18 expression is upregulated on blood monocytes during hypertriglyceridemia and enhances adhesion to VCAM-1. *Arteriosclerosis, Thrombosis, and Vascular Biology*. 2011;10(2)(1):160-166. doi:10.1038/nrm2621.

101. Bi P, Shan T, Liu W, et al. Inhibition of Notch signaling promotes browning of white adipose tissue and ameliorates obesity. *Nature Medicine*. 2014;20(8):911-918. doi:10.1038/nm.3615.

102. Rimm EB, Sc D, Chasman DI, et al. Intensive versus Moderate Lipid Lowering with Statins after Acute Coronary Syndromes. *New England Journal of Medicine*. 2012;367(15):1387-1396. doi:10.1056/NEJMoa1203039.

103. Abookire SA, Karson AS, Fiskio J, Bates DW. Use and monitoring of "statin" lipid-lowering drugs compared with guidelines. *Archives of Internal Medicine*. 2001;161(1):53-58. doi:10.1001/archinte.161.1.53.

104. Nguyen JT, Lin SJ, Tobias AM, et al. A Novel Pilot Study Using Spatial Frequency Domain Imaging to Assess Oxygenation of Perforator Flaps During Reconstructive Breast Surgery. *Annals of Plastic Surgery*. 2013;71(3):308-315. doi:10.1097/SAP.0b013e31828b02fb.

105. Srinivasan S, Pogue BW, Jiang S, et al. Interpreting hemoglobin and water concentration, oxygen saturation, and scattering measured in vivo by near-infrared breast tomography. *Proceedings of the National Academy of Sciences of the United States of America*. 2003;100(21):12349-12354. doi:10.1073/pnas.2032822100.

106. Maier JS, Walker SA, Fantini S, Franceschini MA, Gratton E. Possible correlation between blood glucose concentration and the reduced scattering coefficient of tissues in the near infrared. *Optics Letters*. 1994;19(24):2062-2064. doi:10.1364/OL.19.002062.

107. Laughney AM, Krishnaswamy V, Rizzo EJ, et al. Spectral discrimination of breast pathologies in situ using spatial frequency domain imaging. *Breast Cancer Research*. 2013;15(4):R61. doi:10.1186/bcr3455.

108. Angelo J, Vargas CR, Lee BT, Bigio IJ, Gioux S. Ultrafast optical property map generation using lookup tables. *Journal of Biomedical Optics*. 2016;21(11): 110501. doi:10.1117/1.JBO.21.11.110501.

109. Pera V, Karrobi K, Tabassum S, Teng F, Roblyer D. Optical property uncertainty estimates for spatial frequency domain imaging. *Biomedical Optics Express*. 2018;

9(2):661. doi:10.1364/BOE.9.000661.

110. Lin AJ, Ponticorvo A, Konecky SD, et al. Visible spatial frequency domain imaging with a digital light microprojector. *Journal of Biomedical Optics*. 2013; 18(9):96007. doi:10.1117/1.JBO.18.9.096007.

111. Xu Y, Iftimia N, Jiang H, Key L, Bolster M. Imaging of in vitro and in vivo bones and joints with continuous-wave diffuse optical tomography. *Optics Express*. 2001;8(7):447-451. doi:10.1364/OE.8.000447.

112. Firbank M, Hiraoka M, Essenpreis M, Delpy DT. Measurement of the optical properties of the skull in the wavelenght range 650-950 nm. *Physics in Medicine and Biology*. 1993;38:503-510.

113. Beek JF, Blokland P, Posthumus P, et al. In vitro double-integrating-sphere optical properties of tissues between 630 and 1064 nm. *Physics in Medicine and Biology*. 1997;42(11):2255-2261. doi:10.1088/0031-9155/42/11/017.

114. Peterson HM, Hoang BH, Geller D, Yang R. In vivo, noninvasive functional measurements of bone sarcoma using diffuse optical spectroscopic imaging. *Journal of Biomedical Optics*. 2017;22(12):1. doi:10.1117/1.JBO.22.12.121612.

115. Alexandrakis G, Rannou FR, Chatziioannou AF. Tomographic bioluminescence imaging by use of a combined optical-PET (OPET) system: A computer simulation feasibility study. *Physics in Medicine and Biology*. 2005;50(17):4225-4241. doi:10.1088/0031-9155/50/17/021.

116. Tseng S-H, Bargo P, Durkin A, Kollias N. Chromophore concentrations, absorption and scattering properties of human skin in-vivo. *Optics Express*. 2009; 17(17):14599. doi:10.1364/OE.17.014599.

117. Jacques SL. Optical properties of biological tissues: a review. *Physics in Medicine and Biology*. 2013;58(14):5007-5008. doi:10.1088/0031-9155/58/14/5007.

118. Lecun Y, Bengio Y, Hinton G. Deep learning. *Nature*. 2015;521(7553):436-444. doi:10.1038/nature14539.

119. He K, Zhang X, Ren S, Sun J. Deep Residual Learning for Image Recognition. *2016 IEEE Conference on Computer Vision and Pattern Recognition (CVPR)*. 2016:770-778. doi:10.1109/CVPR.2016.90.

120. Hinton G, Deng L, Yu D, et al. Deep Neural Networks for Acoustic Modeling in Speech Recognition. *IEEE Signal Processing Magazine*. 2012;(November):82-97. doi:10.1109/MSP.2012.2205597.

121. Gulshan V, Peng L, Coram M, et al. Development and validation of a deep learning algorithm for detection of diabetic retinopathy in retinal fundus photographs. *JAMA: The Journal of the American Medical Association*. 2016; 316(22):2402-2410. doi:10.1001/jama.2016.17216.

122. Silver D, Huang A, Maddison CJ, et al. Mastering the game of Go with deep neural networks and tree search. *Nature*. 2016;529(7587):484-489. doi:10.1038/nature16961.

123. Volodymyr Mnih, Koray Kavukcuoglu, David Silver, Andrei A. Rusu, Joel Veness, Marc G. Bellemare, Alex Graves, Martin Riedmiller, Andreas K. Fidjeland1, Georg Ostrovski, Stig Petersen, Charles Beattie, Amir Sadik, Ioannis Antonoglou, Helen King, Dharshan K DH. Human-level control through deep reinforcement learning. *Nature*. 2015. doi:10.1038/nature14236.

124. van de Giessen M, Angelo JP, Gioux S. Real-time, profile-corrected single snapshot imaging of optical properties. *Biomedical Optics Express*. 2015;6(10): 4051. doi:10.1364/BOE.6.004051.

125. Chen X, Lin W, Wang C, et al. In vivo real-time imaging of cutaneous hemoglobin concentration, oxygen saturation, scattering properties, melanin content, and epidermal thickness with visible spatially modulated light. *Biomedical Optics Express*. 2017;8(12):5468. doi:10.1364/BOE.8.005468.

126. Di Lullo GA, Sweeney SM, Körkkö J, Ala-Kokko L, San Antonio JD. Mapping the ligand-binding sites and disease-associated mutations on the most abundant protein in the human, type I collagen. *Journal of Biological Chemistry*. 2002; 277(6):4223-4231. doi:10.1074/jbc.M110709200.

127. Torjesen A, Istfan R, Roblyer D. Ultrafast wavelength multiplexed broad bandwidth digital diffuse optical spectroscopy for *in vivo* extraction of tissue optical properties. *Journal of Biomedical Optics*. 2017;22(3):36009. doi:10.1117/1.JBO.22.3.036009.

128. Park C. New variant PhD: The changing nature of the doctorate in the UK. *Journal of Higher Education Policy and Management*. 2005;27(2):189-207.

CURRICULUM VITAE